Max-Planck-Institut für Plasmaphysik
Garching bei München

Processing and Characterisation of SiC-Fibre Reinforced Cu-Matrix Composites

Carmen Rodica Popescu

Vollständiger Abdruck der von der Fakultät für Maschinenwesen der Technischen Universität München zur Erlangung des akademischen Grades eines

Doktor-Ingenieurs

genehmigten Dissertation.

Vorsitzender:	Univ.-Prof. Dr.-Ing. H. Baier
Prüfer der Dissertation:	1. Hon.-Prof. Dr.-Ing., Dr.-Eng. (Japan) H. H. Bolt 2. Univ.-Prof. Dr. mont. habil. E. Werner

Die Dissertation wurde am 18.12.2003 bei der Technischen Universität München eingereicht und durch die Fakultät für Maschinenwesen am 20.02.2004 angenommen.

Research is formalized curiosity
It is poking and prying with a purpose

Zora Neale Hurston

Acknowledgements

The present research work has been carried out during 2001-2003 at the Materials Research Division, Max-Planck Institut für Plasmaphysik (IPP), Garching.

I would like to express my sincere gratitude to my supervisor Prof. Dr.-Ing. Dr. H. H. Bolt for offering me the opportunity to work in this division, for supplying the very interesting topic, for his cordiality and all the support and especially for contributing his expertise to this work.

My referee Prof. Dr. mont. habil E. Werner deserves my most sincere thanks for reviewing of this work and for many fruitful discussions.
Thanks to my tutor Dr. A. Brendel for her assistance, helpful comments and encouragement.

Furthermore, I would like to thank Prof. Dr. J. Woltersdorf and Dr. E. Pippel, from the Max-Planck Institut für Mikrostrukturphysik in Halle, for making the TEM measurements available to me. Also thanks to Dr.-Ing. C. Leyens, from the Institute of Materials Research of German Aerospace Centre in Cologne, for kindly performing the HIP processes. Further thanks to Dr. P. Peters, from the same institution, for performing the composite tensile tests, and to Dr. Dipl.-Ing. L. Krämer, from the Technische Universität München, for giving me the possibility to use the tensile test device of his division.

Also thanks are expressed to the members of the Materials Research Division at IPP, to the staff and personnel of the laboratory for their kind collaboration, the friendly working atmosphere and their constructive criticisms and corrections, very especially to Dipl.-Ing. S. Linding and G. Matern for their experimental support.

Special thanks to my colleague and friend T. Höschen for his unwavering patience, understanding and encouragement to the whole work, without which I would probably never have been able to complete this work.

All of the above and many others have contributed substantially in one way or another to the preparation of this thesis. I express my deepest gratitude and appreciation to all of them.

Carmen Popescu

December 2003

Abstract

In a fusion reactor heat fluxes of 10-20 MW/m^2 will occur, which will have to be removed by heat sinks. This poses a great challenge to the heat sink materials. A thermal conductivity of 200 W/mK in combination with an operating temperature of 550°C will be required. This high temperature level favours an efficient energy conversion.

Copper has the necessary thermal conductivity, but does not possess a sufficient creep resistance, especially under neutron irradiation. To improve the high temperature values of creep and tensile strength, a reinforcement of copper by SiC long fibres (Textron SCS-6) was developed.

The copper matrix was deposited onto the fibres galvanically and subsequently the compound was consolidated in a hot pressing process. Structuring of the internal interfaces was performed by magnetron sputter deposition of Ti layers with a thickness in the nanometer range in combination with a thermal treatment to obtain the formation of carbides. The materials properties and structure were characterised by microscopy, micro indentation, push-out tests, and tensile tests. This revealed significant differences between compound samples with and without Ti interlayers.

Without treatment the adhesion between fibre and matrix was very weak. Push-out tests yielded adhesive shear strengths of 5 MPa. No chemical reaction between carbon on the fibre surfaces and the copper matrix occurs.

Applying a thin Ti coating as an interlayer improved the adhesive shear strength to a value of 60 MPa. By an appropriate heat treatment it was possible to obtain a carbide bonding of the carbon on the fibre surface and in this way initiate a chemical bonding between fibre and matrix. At the same time this improved the mechanical coupling between fibre and matrix, because the chemical reaction resulted in an interlocking between the TiC and the copper matrix.

For the first time it could be demonstrated in this work, that a reinforcement of copper by SiC long fibres is possible. The strength increases with increasing fibre volume fraction.

Kurzfassung

In einem Fusionsreaktor treten Wärmeflüsse von 10-20 MW/m^2 auf, die in Wärmesenken abgeführt werden müssen. Aufgrund dieser Belastung werden hohe Ansprüche an das Wärmesenkenmaterial gestellt. Gefordert ist eine Wärmeleitfähigkeit von 200 W/mK verbunden mit einer Einsatztemperatur von 550°C. Das hohe Temperaturniveau begünstigt eine effiziente Energieumwandlung.

Kupfer besitzt die erforderliche Wärmeleitfähigkeit, hat aber bei den hohen Betriebstemperaturen besonders unter Neutronenbestrahlung eine zu geringe Kriechbeständigkeit. Zur Verbesserung der Hochtemperaturzähigkeit und -festigkeit wurde eine Verstärkung des Kupfers mit SiC-Langfasern (Textron, SCS-6) entwickelt.

Die Cu-Matrix wurde durch galvanische Abscheidung auf die Fasern aufgebracht und der Verbundwerkstoff anschließend in einem Heißpressprozess konsolidiert. Die Strukturierung der inneren Grenzflächen erfolgte durch Magnetron-Sputtern von Ti-Schichten im Nanometerbereich verbunden mit einer thermischen Behandlung zur Karbidbildung. Materialstruktur und Eigenschaften wurden durch Mikroskopie, Mikroindentierung, Push-out-Versuche und Zugprüfungen charakterisiert. Dabei wurden Unterschiede zwischen den Verbundproben mit und ohne Titan-Zwischenschicht deutlich.

Ohne Modifizierung der Grenzfläche war die Haftung zwischen Faser und Matrix sehr gering. Im Push-Out Versuch wurden Haftscherfestigkeiten von 5 MPa errechnet. Es findet keine chemische Reaktion zwischen Kohlenstoff auf der Faseroberfläche und Kupfer statt.

Erst durch eine wenige nm dünne Titanschicht als Zwischenschicht stieg die Haftscherfestigkeit auf 60 MPa. Durch eine geeignete Wärmebehandlung ist es gelungen, den Kohlenstoff auf der Faseroberfläche karbidisch zu binden und damit eine chemische Bindung zwischen Faser und Matrix zu erreichen. Gleichzeitig wurde die mechanische Kopplung zwischen Faser und Matrix dadurch verbessert, dass sich das gebildete TiC mit der Kupfermatrix verzahnte.

In dieser Arbeit konnte erstmals gezeigt werden, dass eine Faserverstärkung des Kupfers mit SiC-Langfasern möglich ist. Die Festigkeitswerte erhöhen sich entsprechend dem Faservolumenanteil.

Content

List of symbols:

Symbol:	**Unit:**	**Denotation:**
A	mm^2	area
b_i	µm	interface thickness
C	nm/mN	contact compliance
C_f	nm/mN	machine compliance
C_s	nm/mN	sample compliance
c_V	J/m^3K	volume specific heat
E	GPa	modulus of elasticity or Young's modulus
E_1	GPa	modulus of elasticity for the composite in the direction of alignment
E_2	GPa	modulus of elasticity for the composite in the transverse direction
E_r	GPa	reduced modulus of elasticity
F	N	force
G	GPa	shear modulus
H	GPa	hardness
h	nm	penetration depth
h_c	nm	contact depth
h_f	nm	final depth
K	W/mK	thermal conductivity
L	mm	length
P	N	load
R	µm	radius
S	N/m	stiffness
T	K, °C	temperature
TS	GPa	tensile strength
v	m/s	average velocity of heat carrier
V_i	vol %	volume fraction of phase i
α	10^{-6} K^{-1}	thermal expansion coefficient
γ	-	shear strain
γ_{ij}	-	shear strain (rotation towards the i-direction of the j-axis) for the composite
Δ	-	precedes the symbol of a parameter to denote finite change
ε	-	engineering strain
ε^*	-	longitudinal fracture strain
ε_{ym}	-	strain where the matrix yields and deforms plastically
ϕ	µm	grain size
λ	m	mean free path of heat carrier
μ	-.	coefficient of friction
ν	-	Poisson's ratio
σ	MPa	engineering stress

Abreviations:

BSE	back-scattering electron
CCD	charge coupled device
CFC	carbon-fibre reinforced carbon
CMF	carbon monofilament
CTE	coefficient of thermal expansion
$Cu\text{-}C_f$ MMC	carbon fibre reinforced copper matrix composites
CVD	chemical vapour deposition
D	deuterium
DC	direct current
DLR	german aerospace centre
DS	dispersion strengthened
e^-	electron
EDS	energy dispersive spectrometry
EDX	energy dispersive X-ray
EDXS	energy dispersive X-ray spectroscopy
ESEM	environmental scanning electron microscope
ETPC	electrolytic tough pitch copper
FEA	Finite Element Analysis
GIF	electron energy filter
HIP	hot isostatic pressing
HREM	high resolution electron microscopy
HVEM	high voltage electron microscopy
LCFS	last closed flux surface
M	metal
MMC	metal matrix composite
MT	microindenter head
NT	nanoindenter head
PFC	plasma facing component
PFM	plasma facing materials
PH	precipitate hardened
PMI	plasma-material interaction
PVD	physical vapour deposition
PyC	pyrolytic carbon
RF	radio frequency
RT	room temperature
SCS	silicon carbide fibre
SE	secondary electron
SEM	scanning electron microscopy or microscope
SiC	silicon carbide
SOL	scrape off layer
STEM	scanning transmission electron microscopy
T	tritium
TEM	transmission electron microscopy or microscope
TiC	titanium carbide

$\overline{\sigma}$	MPa	volume-averaged stress
σ^*	MPa	longitudinal fracture strength
σ_y	MPa	yield strength
σ'_m	MPa	stress in matrix at composite failure
τ_d	GPa	interfacial shear strength
τ_{fr}	GPa	interfacial friction stress
τ	GPa	shear stress
τ_{ij}	MPa	shear stress acting in the i-direction on the plane with a normal in the j-direction

Subscripts:

i	indenter
i	initial
0	original
f	fiber
m	matrix
c	composite
ct	Transverse direction (composite)
cl	longitudinal direction (composite)
max	maximum
min	minimum
d	debonding
fr	friction
y	yielding
a	aparent

1. Introduction

Over ninety percent of the world's energy requirements are covered today by fossil energy sources. These are coal, crude oil and natural gas. The fossil energy is limited by finite reserves of non-renewable deposits [1], and the combustion of fossil fuels is creating the much-feared "greenhouse effect" by releasing carbon dioxide to the atmosphere. This has adverse effects upon the climate. The greenhouse gases resulting from human activities prevent heat (infrared) radiation from the earth's surface to escape into the space causing an additional warming of the earth's surface called anthropogenic climate change. The climate change is considered to be the most severe environmental risk for the globe and mankind [2].

Therefore the methods of energy production and use have to be modified. The amount of economically efficient energy sources capable of replacing coal, oil, and gas is, however, very limited. Some alternatives to fossil fuel are solar energy, hydropower, wind energy and nuclear energy [3]. In the following decades nuclear power will be one of the means of producing a large amount of electricity without carbon dioxide and aerosol emissions. There are two kinds of nuclear power sources: fission and fusion.

Fission is the process used today in nuclear power plants. Atoms such as uranium are split thus releasing the internal energy that holds the atom together. Besides nuclear fission there is the possibility of fusion, one method of transforming mass into energy in which light atoms fuse to form heavier ones. During the fusion of elements with low atomic numbers substantial amounts of energy are released.

As an energy source, fusion has several advantages over fission. First, the fuel (deuterium and tritium) is easily attainable. Second, nuclear fusion would be safer than nuclear fission. Even if there were to be an accident at a fusion reactor, exposure to radiation for humans would be 100 times less than in a fission reactor accident [4, 5]. Third, the problem of hazardous waste, which has been in part responsible for holding back development of nuclear fission as an energy source, is expected to be at least 100 and perhaps 10.000 or more times lower in fusion than that it is in fission [5-8].

The external costs of fusion are in the same range as the external costs of solar and wind energy [9]. For better efficiency and therewith reduction of the price of fusion energy an optimisation of service temperatures is required. This demands the employment of high performance materials, such as high power heat sinks - an issue to be resolved.

Future energy needs will require contributions from many sources and fusion is one of the most attractive alternative. Fusion power is a promising long-term candidate to supply the energy needs of mankind [10, 11].

1.1. Thermonuclear fusion

For centuries, the way in which the sun and stars produce their energy remained a mystery to man. Only during this century scientists have discovered that they produce their energy by the fusion process of hydrogen to helium. Einstein's theory that mass can be converted into energy provided the basis for energy release in nuclear reactions such as fusion [12].

Fusion is the process that powers the sun and the stars. Here on earth fusion represents a potentially unlimited source of energy for mankind.

1.1.1. Fusion basics

Many different nuclear fusion reactions occur in the sun and other stars, but only a few reactions are of practical value for potential energy production on earth. These all involve hydrogen. To produce net power, fusion reactions must take place at high temperatures. With increasing temperature, all materials are successively transformed from the solid to the liquid and then to the gaseous state. If the temperature is further increased, the atoms of the gas decompose into their constituents, electrons and nuclei and therefore plasma - the "fourth aggregate state of matter" is obtained. A plasma is an ionised gas consisting of a sea of ions and electrons and is a very good conductor of electricity and is affected by magnetic fields [13].

There are several candidate fusion reactions involving the light isotopes hydrogen (H), deuterium (D) and tritium (T), but D-T fusion is most intensely investigated because it should be most easily achieved (deuterium and tritium fuse at lower temperature). In the fusion reaction a deuterium and tritium atom combines together, or fuses, to form an atom of helium and an energetic neutron (Fig. 1.1.) [13].

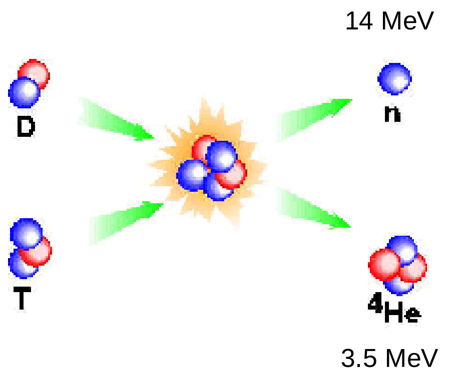

Figure 1.1. The D-T reaction

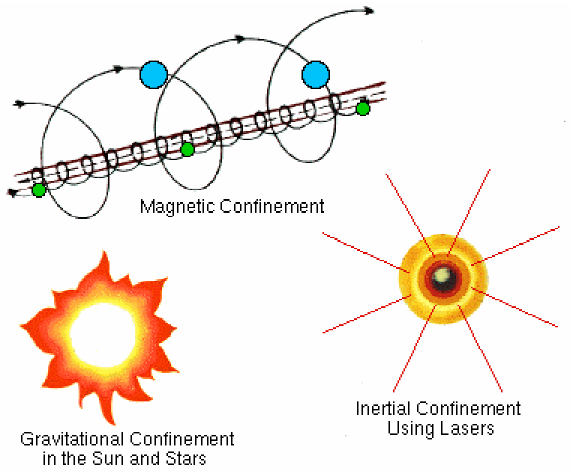

Figure 1.2. Plasma confinement [14]

$$\mathbf{D + T \Rightarrow {}^{4}He + n + 17.59\ MeV}$$

The released energy is distributed between a neutron and a charged ^{4}He nucleus, an alpha particle. In a magnetic confinement scheme, the neutron is not confined and escapes from the plasma. The charged ^{4}He particle, however, is confined by the magnetic field. Its energy must be thermalised to sustain the high plasma temperature.

Hydrogen is found in water and consists of one proton in the atomic nucleus and one electron orbiting the nucleus. Deuterium is one of the isotopes of hydrogen and consists of one proton and one neutron in the nucleus and one orbiting electron. One out of approximately 6500 hydrogen atoms in ordinary water is a deuterium atom. Tritium is the other isotope of hydrogen and consists of one proton and two neutrons in the nucleus and one orbiting electron. Deuterium can be easily extracted from seawater and tritium can be bred in a power plant from lithium, which is abundant in the earth's crust, according to following reaction:

$$^{6}\mathrm{Li} + \mathrm{n} \Rightarrow {}^{4}\mathrm{He} + \mathrm{T} + 4.78\ \mathrm{MeV}.$$

Releasing the potential energy source of fusion on earth requires temperatures of 100 million degrees or more and confining and controlling such a reaction is difficult. Three methods are currently known (Fig. 1.2.): gravitational confinement, which takes place in stars but is not possible on earth, inertial confinement, and magnetic confinement.

Inertial confinement uses pulsed energy sources (e.g. laser beam or X-ray) to concentrate energy on a small frozen pellet of fusion fuel. This pulsed energy source compresses the pellet up to a thousand times normal solid density and heats the fuel to ignition temperature. Researchers at Sandia National Laboratories, Albuquerque/New Mexico, succeed for the first time to fuse hydrogen atoms using inertial confinement and X-rays [15].

Magnetic confinement uses magnetic fields to hold a plasma (ionised gas) in place while it is heated to ignition temperature by external sources.

Owing to its high temperature fusion plasma cannot be confined direct in material vessels. Any wall contact would immediately re-cool the thin gas. Also the uncontrolled contact between the hot plasma and the wall leads to material destruction e.g. by melting. The problem is obviated by using magnetic fields, which confine and thermally insulate the fuel keeping it away from the vessel walls. Charged particles - ions and electrons - are forced in a magnetic field into circular gyration around the magnetic field lines. The particles are thus tied to the field lines. In the longitudinal direction they are able to move freely alongside the lines. In a suitably shaped magnetic field cage it is therefore possible to confine a plasma and keep it away from material walls.

On the other hand there is a need of controlled contact of plasma with special surfaces to allow the exchange of already fused He-particles with fresh fusion fuel. The therefore utilised component is called divertor, being described in the next chapter.

1.1.2. Fusion reactors, plasma facing components and related material questions

On its way to a power plant fusion research is concentrating on two different types of confinement configurations, the tokamak and the stellarator. Most of the devices in the world today are of the tokamak type, which is best investigated and comes closest to the ignition conditions.

Both types feature ring-shaped magnetic fields. Tokamaks (Fig. 1.3) produce part of these fields by means of an electric current flowing in the plasma. Stellarators (Fig. 1.4) form the magnetic field cage solely by means of external coils. Stellarators are thus suitable for continuous operation, whereas tokamaks without auxiliary facilities can only work in pulsed mode.

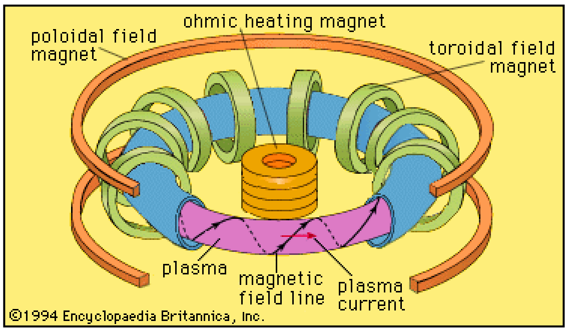

Figure 1.3. Schematic diagram of a Tokamak

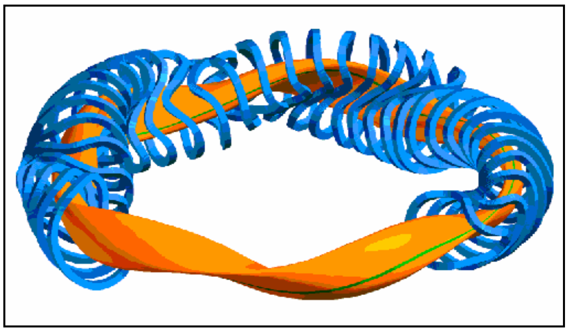

Figure 1.4. W 7-X Wendelstein Stellarator external coils

There are many tokamaks existing in the world. In Europe, those that can be mentioned are JET in England - the most powerful European tokamak device -, ASDEX Upgrade at IPP-Garching, TEXTOR, which is operating in the Research Centre Jülich (Germany) and TORE SUPRA, a medium sized tokamak with superconductive coils operated by CEA in Cadarache (France). The next project, ITER (Fig. 1.6.), should reach the equilibrium between the recycled energy and the produced power (break-even point) and the last step before building a real industrial reactor is called DEMO and would be the prototype of the fusion reactor built in a power plant (Fig. 1.5.).

The main components of a fusion reactor are: the superconductive coils, the blanket, the neutron shield and a toroidally structured wall with Plasma Facing Components (PFCs) like first wall and divertor.

In a tokamak configuration the inner part of the plasma -the confinement region- which is confined by closed field lines, is separated from the outer part with open field lines. The outermost closed magnetic field surface is characterised by a zero region in the poloidal magnetic field within the vessel known as ‘X point’. This boundary is called the last closed flux surface (LCFS) or separatrix (Fig. 1.7. and 1.8.). Magnetic field surfaces inside the LCFS are closed, confining the plasma ions. The edge region, just inside the LCFS, can contain significant levels of not fully ionised impurities and also neutral particles. Impurity line radiation and neutral particles transport some power from here to the wall. The remaining power leaving from the core plasma enters the region outside the LCFS either by conduction or by convection. This region is known as the scrape off layer or ‘SOL’ as here the power is rapidly ‘scraped off’ by electron heat conduction along open field lines, which are diverted to intersect with materials targets, in what is known as a ‘divertor’ [16]. On its way to these target plates the plasma, which is initially thin and hot, is cooling down and becomes denser. This enables the plasma to radiate part of its energy away before it reaches the targets. As a result, the erosion and power load on the targets can be minimised.

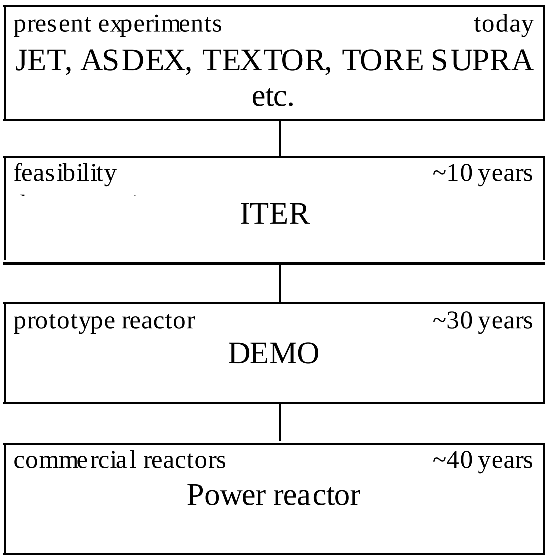

Figure 1.5. Approximate fusion time table [17]

In the field of fusion reactor technology, one of the most important tasks is the development of so-called “Plasma Facing Components”, which are high performance materials targets directly exposed to the plasma. Different design solutions have been developed for each plasma facing component depending on its specifications and functions [18]. Material selection and plasma-facing component (PFC) design remain major challenges in the safe and reliable operation of the thermonuclear reactors, and are perceived to be potential obstacles to the successful development of any long-pulse or steady-state deuterium-tritium (D-T) fusion reactor.

The first element encountered by plasma heat load is called *first wall*. Its function is to absorb particles and radiative heat fluxes from the plasma and thus protect the other components from the fusion plasma. Some technical parts on the walls of a fusion reactor, for example antennas, have to be protected against the plasma by material shields, the so called *limiters.*

In order to achieve clean plasmas by impurity control, a magnetic configuration called *divertor* may be used (Fig. 1.7.). The main function of the divertor system is to exhaust the major part of the alpha particle power as well as He and impurities from the plasma. As the main interface component under normal operation between the plasma and material surfaces, it must tolerate high heat loads and remove these heat loads reliably under stationary conditions. The divertor will need to be replaced and upgraded several times during the life of thermonuclear reactors.

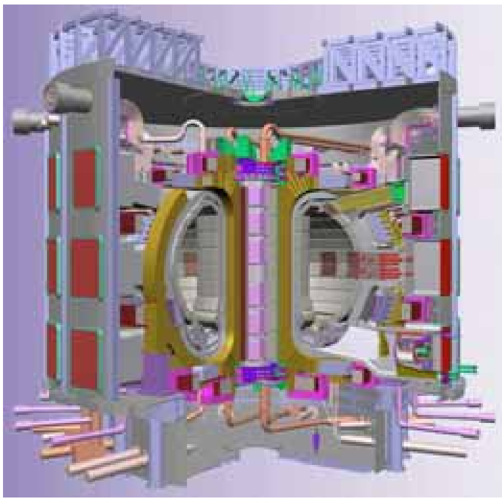

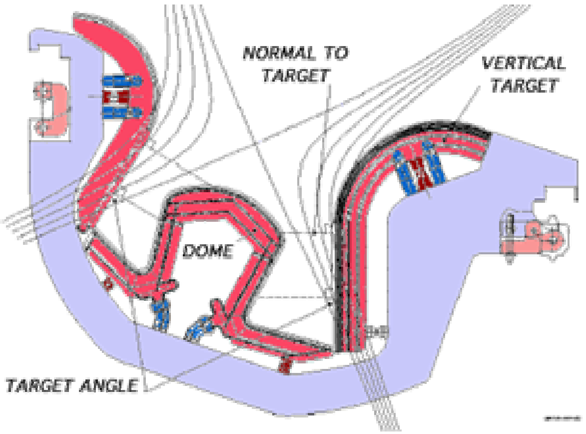

Figure 1.6. Cut-away view of the ITER

Figure 1.7. Cross-section through ITER divertor

The geometry of the divertor in future experiments is based on numerical simulations obtained using Monte Carlo codes for neutral atoms coupled to transport codes for the magnetically confined ions [19] and by extrapolation from results of tokamak experiments [20]. Whereas different engineering solutions are described elsewhere [21], the impact of the different physics effects on the chosen geometry and on the ITER divertor design and the lifetime of the various divertor components are discussed in [22].

The reference configuration for the ITER divertor is a vertical target/baffle with an open private flux region (the space below the separatrix X-point which has no flux line connections to the main plasma) and a “dome” below the X-point (Fig. 1.8.). The inner and outer vertical targets are PFCs, which in their lower part interact directly with the SOL plasma and in their upper part act as baffles for the neutrals. They are inclined so as to intercept the magnetic field lines of the separatrix at an acute angle, giving deep inboard and outboard channels in which to establish a partially detached plasma regime. In this regime, while the plasma remains attached in the outer region of the SOL, the plasma is detached from the PFCs in the region near the separatrix, causing the power profile to broaden and power to be radiated to other surfaces. Together with the lower end of each vertical target, a neutral particle reflector plate forms a ‘V’ shape that confines neutral hydrogenic particles in the divertor channels and aids partial plasma detachment.

Typically, in fusion devices the components facing the plasma (PFC) consist of plasma facing materials (PFM) bonded to a metallic heat sink furnished with cooling tubes for heat removal (Fig. 1.9.). To permit an equitable thermal efficiency, in a reactor the components are subjected to a higher temperature level in comparison to ITER. The superior limit will be determined by the temperature limits of the PFM and heat sink materials.

The appropriate selection of the armour materials for the PFCs of a next step experimental fusion reactor is a compromise between multiple requirements derived from the unique features of a burning fusion plasma environment. The factors that affect the selection result from the requirements of plasma performance, component lifetime, safety rules and cost [23].

The PFMs (divertor) which are in direct contact with the plasma are subjected to erosion processes which limit the component lifetime and also lead to impurity transport into the burning plasma, affecting its performance [24]. Many plasma-material interaction (PMI) issues remain still to be solved [25]. These components have to be suitable for operation under high thermo-mechanical loading. Moreover, the components must withstand intense irradiation by particle and energy exhaust from the plasma and by energetic fusion neutrons, respectively.

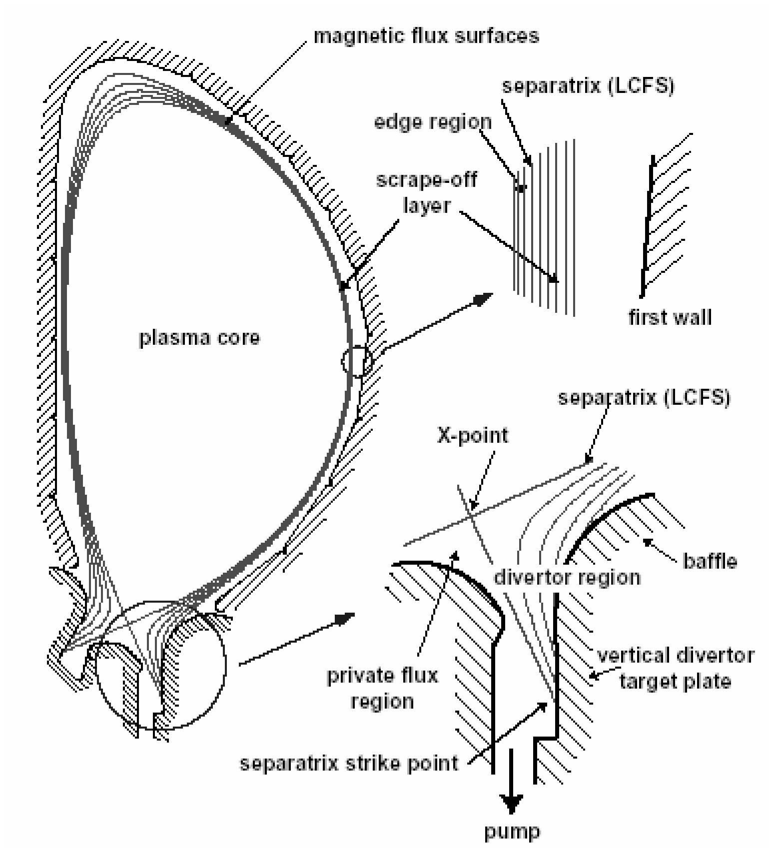

Figure 1.8. Poloidal cross-section of an ITER plasma, illustrating the regions of the plasma and the boundary walls where important atomic physic processes take place. The characteristics regions are: (i) the plasma core, (ii) the edge region just inside the separatrix, (iii) the scrape-off-layer (SOL) plasma outside the separatrix, and (iv) the divertor plasma region, which is an extension of the SOL plasma along field lines into the divertor chamber [16].

The critical role that PMIs play in the achievement of the technical objectives of a reactor-class fusion device can be easily understood from the consequences that these interactions have on the plasma performance and the surrounding material surfaces. One critical issue is the trapping, re-emission, and retention of tritium, affecting plasma fuelling and tritium inventory, which affects fuel availability and safety [26]. Recent experimental and modelling results have indicated four key problem areas that will greatly affect PFC design of next-step devices. They are (i) dispersal of the power and control of the particles and impurities to provide an adequate lifetime of PFCs and a tolerable plasma contamination; (ii) mitigation of off-normal events to reduce their severe effects on PFCs; (iii) minimisation of the tritium accumulation and development of efficient means of tritium removal; (iv) minimisation and control of the production of radioactive dust. A detailed discussion of these problems is beyond the scope of this paper. The interested reader is referred to [16] for further details and relevant bibliography.

The plasma facing material of the divertor, which receives severe localised and cyclic heat loads during operation, requires high thermal conductivity, excellent thermal shock resistance, low erosion by plasma particles and good connection with the heat sink material for active cooling. Resistance against radiation damage, low activation and high thermal efficiency are further issues.

In the ITER design, for the most highly loaded area - the vertical target strike zone - which receives high heat loads in steady state, 5-10 MW/m^2, and in 10 s long transients up to 20 MW/m^2, carbon-fibre reinforced carbon (CFC) with good thermal conductivity and proven structural integrity (e.g. non-melting) has been proposed as PFM [27]. In areas with relatively low steady state heat loads, 1-5 MW/m^2, where no ion fluxes but large charge exchange neutral fluxes occur, a material with a high sputtering threshold and thus a long erosion lifetime is favoured. Tungsten is such a material [28, 29]. Each of these materials has some inherent advantages and disadvantages. The rationale for this selection is thoroughly discussed elsewhere [29-32].

	ITER	DEMO
Component replacements	Up to 3	5 year cycle
Normal operation		
No. of cycles	10 000?	<1000
Peak particle flux ($10^{23}/m^2s$)	~10	~10
Surface heat flux (MW/m^2)	~10 /3	. . .10. . .
PFM operational temp. (°C)	W: 200–1000 CFC: 200–1500	W: 350–500
Av. neutron fluence (MWa/m^2)	Max. 0.15	5
Displacement damage/ transmut. production	CFC 0.7/230	
	W 0.7/0.15% Re	W 15/3% Re
(dpa/appm (He))	Cu 1.7/16	Cu 60/600
(dpa/%Re for W)	SS 1.6/16	RAFM steel 60/600
Heat sink		
Interface temperature	<350°C	>350°C
Interface material		MMC-Cu
Sink material	CuCrZr (Cu)	Cu (CuCrZr)

Table 1.1. Divertor requirements in future fusion devices [33]

Table 1.1. compares the parameters of the divertor of ITER and DEMO which are most relevant from the materials point of view. The neutron load, the fluence and the neutron damage in the divertor's PFM will be higher in DEMO while the heat load will be in the same range. An important difference between ITER and DEMO lies in the number of operating cycles and in the number of off-normal events. The conditions required for reactor operation are determined by the necessity of long operation time between component exchange periods. For DEMO, a steady-state operation should be achieved and the off-normal events eliminated or at least reduced to the level of extremely unlikely events. In ITER the divertor components are subjected to erosion rates due to sputtering and off-normal events, but the last largely exceed that coming from sputtering. Then tungsten as PFM seems to be the preferred option in DEMO, where the transient loads are abolished, the sputtering remaining the main, if not the only contribution to erosion. Tungsten instead of any carbon material will also eliminate any problem of tritium co-deposition, which is the limiting factor in using CFC in ITER.

The heat sink materials have to exhibit a high thermal conductivity, needed for achieving an efficient heat transfer into the cooling system. In addition to thermal conductivity, other properties as tensile strength and ductility, fracture toughness, fatigue at high temperature and irradiation resistance have to be taken into consideration. Owing to its excellent thermal conductivity strengthened copper is a viable candidate for heat sink applications in the divertor of ITER [34]. A selected number of precipitation hardened (PH) and dispersion strengthened (DS) copper alloys, which possess good thermal conductivity, stable elevated temperature strength and adequate resistance to irradiation damage are the choice for the heat sink of the high heat flux components in ITER [35, 36]. The analysis shows that due to their high mechanical strength and thermal conductivity precipitation hardened CuCrZr alloys are the most reasonable choice for the ITER divertor where fatigue and resistance to fracture are most critical [37-39]. According to the estimation in [40], the PH copper alloys could be used for the PFCs up to 350 °C under the applied stress intensity of 100 MPa. In DEMO or a power reactor to increase the efficiency higher service temperature is required, this implying divertor operation at higher heat sink temperature.

In a PFC the incident heat flux will be conducted through the thickness of the PFM and through the interface into the heat sink structure. Due to the temperature profile and the different thermal expansion coefficients of the two materials this thermal load generates thermal stresses in the PFC.

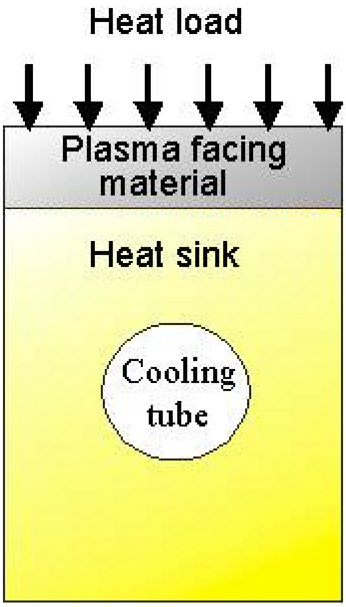

Figure 1.9. Schematic of PFC structure

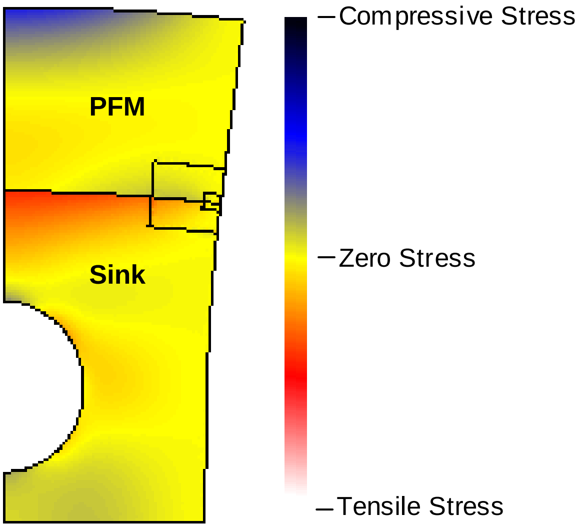

Figure 1.10. FEA simulation of thermal stresses in PFC

From Finite Element Analysis (FEA) simulation it has been noticed that the thermal stress is higher at the interface between PFM and metallic heat sink [41] and at the cooling tube circumference [42]. This is shown in Fig. 1.10., where the stresses in a PFC are visualised by different colours. The thermal stress leads to a fatigue mechanism that can lead to the junction failure [43]. The fibre reinforced metal matrix composites (MMCs) are potential candidate materials for the PFC application, since the combination of different properties of fibre and matrix can lead to versatile performance of these materials [44]. Suitable MMCs have to be developed and characterised.

According to the before discussed requirements, tentative MMCs to be used at the interface between PFM and heat sink in the divertor of DEMO and other power reactors are the SiC fibre reinforced Cu composites, where the strength and temperature limit of Cu is increased by SiC fibres [44]. While Cu supplies the thermal conductivity, SiC-fibres provide the needed tensile strength. Both materials seem to be convenient to withstand the high irradiation exposure in a fusion device [45, 46].

The design of the divertor for future thermonuclear reactors includes various combinations of joints between PFM and heat sink material. The joints must withstand the thermal, mechanical and neutron loads and the cyclic operation-mode and operate under vacuum conditions, while providing an acceptable design lifetime and high reliability [47, 48]. The impact of hot isostatic pressing (HIP) as a joining procedure on the degradation of the physical and mechanical properties of a CuCrZr alloy is discussed in [49].

The joining technology of the PFM has been developed to a standard allowing the removal of stationary surface heat loads on the order of 20 MW/m^2. This is of special importance, since divertor loads in ITER can reach 20 MW/m^2 under quasi-stationary conditions.

1.2. Objectives of the thesis

The main objectives of this thesis are processing and characterisation of a new metal matrix composite (MMC) material consisting of long silicon carbide fibres (high strength) reinforcing a copper matrix (good thermal conductivity). Thereby the high thermal conductivity of the copper should be maintained and the mechanical properties at high temperatures will be improved by the reinforcement. This composite is a possible candidate material for the joining region between the PFM and the CuCrZr heat sink of PFCs in future fusion reactors (Fig. 1.11.), where the thermal stresses are elevated owing to the different thermal expansion coefficients of the joined materials.

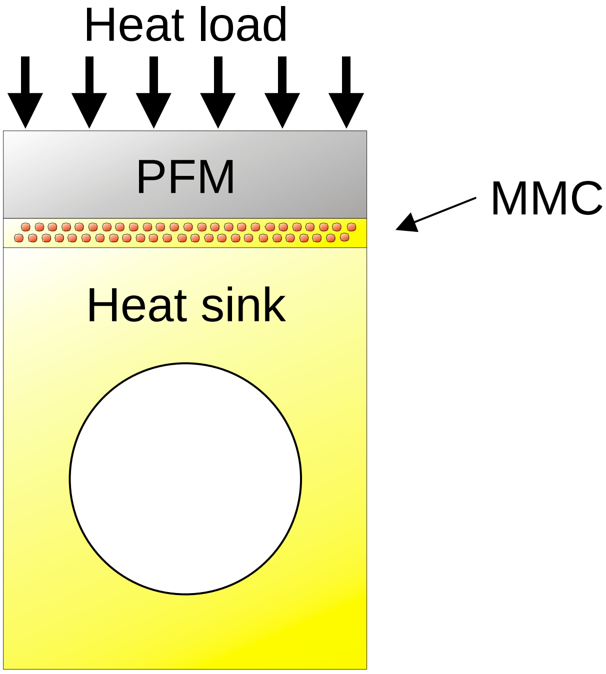

Figure 1.11. Sketch of an improved PFC

CuCrZr heat sinks allow a maximum operation temperature of 350°C in ITER. But in DEMO the use of Cu-MMC will possibly lead to temperatures greater than 350°C at the PFM/heat sink interface and a temperature of about 350°C near the coolant. The higher service temperature will lead to an increased energy efficiency of the fusion power plant.

Processing

In order to synthesise Cu-MMC, SiC fibres (SCS-6, Textron) will be electrolytically coated with a thick pure copper layer. The post deposition heat treatment will be optimised as to avoid the formation of pores in the copper matrix. The coated and annealed fibres are then consolidated by hot isostatically pressing in a copper capsule.
The composite performance depends on the quality of the matrix/reinforcement interface.

From investigations of carbon-fibre-reinforced copper it is well-known that copper wets the fibres very poorly, which entails little adhesion between the fibre and the matrix. SiC fibres that exhibit a thin carbon layer at the surface are also expected to be poorly wet by copper. Therefore the SiC fibres must be pre-treated by suitable procedures, which will allow a better adhesion. A possible way to improve adhesion is the introduction of a reactive interlayer between the fibre and the copper matrix. The proper interlayer should meet the requirements imposed by the required properties of the final-material. It should assure a proper bonding between the fibre and the matrix. Also the coating must not impair the original fibre strength.

One of the main tasks of the Cu/SiC composite development treated in this work is the optimisation of the fibre-matrix interface by applying a thin (several ten nm) titanium film on the SiC fibre.

Magnetron-sputter-deposition provides the possibility to deposit thin functional Ti-interlayers on SiC fibres covered by a copper film to impede oxidation. During suitable annealing active carbide-elements should be formed at the carbon-rich fibre surface and with this chemical coupling the interface strength will be increased.

Characterisation and properties

The requirements of a composite material are structural integrity and mechanical stability.

Morphology and microstructure

For structural characterisation optical and scanning electron microscopy (SEM) will be used.

After metallographic preparation the matrix microstructure will be revealed with optical microscopy. This will show the necessity of optimisations like annealing for reduction of pores. The optimal process parameters for degassing the coated fibres will be determined by mass-spectrometer measurements during ultra-high-vacuum heating.

The morphology and composition, especially processing impurities, will be determined with a scanning electron microscope (SEM) equipped with an energy dispersive X-ray spectrometer (EDX).

The structure in the nanometer range developed at the interface during processing is characterised with a transmission electron microscope (TEM).

The TEM is equipped with a quantitative x-ray microanalysis system which allows a laterally resolved measurement of the chemical composition at the fibre/matrix interface.

Thermal cycling tests, simulating the composite loading under true operation conditions will provide information about the long term behaviour.

Mechanical properties

To estimate the possibility of matrix hardening by diffusion from the fibre reinforcement, micro-hardness measurements will be carried out at different distances to the fibre.

For interface characterisation fibre push-out tests will be performed. Single fibres will be pushed out of the matrix using a microindenter tip. The interfacial shear strength and the interfacial friction stress will be derived. Thus information on the fibre-matrix adhesion will be obtained.

The stress-strain behaviour of the Cu/SiC-composite will be established by tensile tests at ambient temperature. In addition also the constituent materials (copper, SiC fibres) will be tested. Values for elastic modulus, matrix yielding and ultimate tensile strength will be derived.

1.3. Literature review

A composite material can be described as a mixture of component materials designed to meet a specific engineering role by exploiting the desirable properties of the components, whilst minimising the harmful effects of their less desirable properties.

Composites are combinations of two materials in which one of the materials, called the reinforcing phase, is in the form of fibres, sheets or particles, and is embedded in the other material called the matrix phase. The reinforcing and the matrix material can be metal, ceramic or polymer. Composites are classified according to the type of matrix material: metal matrix composites (MMC's), ceramic matrix composites (CMC's), polymer matrix composites (PMC's). Typically, reinforcing materials are strong while the matrix is usually a ductile or tough material. If the composite is designed and manufactured correctly, it combines the strength of the reinforcement with the toughness of the matrix to achieve a combination of desirable properties not available in any single conventional material [50].

An early example of application of composites is israelites using bricks made of clay and reinforced with straw, where the individual constituents – clay and straw – could not serve the function by themselves but did when put together. Some believe that the straw was used to keep the clay from cracking, while others suggest that it blunted the sharp cracks in the dry clay [51].

Historical examples of composites are abundant in the literature. Significant examples include the use of reinforcing mud walls in houses with bamboo shoots, glued laminated wood by Egyptians and laminated metals in forging swords. In the 20th century, modern composites used in the 1930s were glass fibres reinforced resins. Boats and aircraft were built out of these glass composites, commonly called fibreglass. Since the 1970s, application of composites has widely increased [51].

1.3.1. Thermo-mechanical behaviour of composites

The purpose of a composite material is to alter and improve the properties of the matrix material, by the addition of some second material with very different chemical and structural properties. An important area of composite research are metal-matrix composites (MMCs), in which a metallic host material is modified through the addition of a ceramic. The ceramic may be in the form of particles or fibres. The goal is to supplement the desirable properties of the metal, such as ductility, by the addition of a ceramic, which can improve the performance of the material in its final application. Common goals in the creation of new metal-matrix composites are to achieve increased strength and stiffness, reduce friction, or prevent corrosion. Other important improvements in parameters such as component weight, wear resistance, thermal expansion and high temperature capabilities can be achieved by suitable combinations of reinforcing materials in metallic matrices [52].

Composite materials have many characteristics that are different from more conventional engineering materials. Most common engineering materials are homogeneous and isotropic. In contrast, composite materials are often both inhomogeneous and anisotropic. The inherent anisotropy of composite materials leads to mechanical behaviour characteristics that are quite different from those of conventional isotropic materials [53].

It is useful to be able to predict the thermo-mechanical behaviour of a metal matrix composite by appropriate formulae if the thermo-mechanical behaviour of matrix and fibre are known. The thermo-mechanical behaviour of a material can be categorised into two types: mechanical and thermal. The most important thermal behaviour can be described by conduction and thermal expansion laws and that of the mechanical behaviour by a combination of elastic-plastic and creep laws.

1.3.1.1. Mechanical behaviour

Central to an understanding of the mechanical behaviour of a composite is the concept of load sharing [54] between the matrix and the reinforcing phase. The stress may vary sharply from point to point, but the proportion of the external load borne by each of the individual constituents can be gauged by volume-averaging the load within them. Of course, at equilibrium, the external load must equal the sum of the volume-averaged loads borne by the constituents. This gives rise to the condition

$$V_f \bar{\sigma}_f + (1 - V_f)\bar{\sigma}_m = \sigma \qquad (1.1.)$$

governing the volume-averaged matrix and fibre stresses ($\bar{\sigma}_m$, $\bar{\sigma}_f$) in a composite under an external applied stress σ, containing a volume fraction V_f of reinforcement. Thus, for a simple composite under a given load, a certain proportion of that load will be carried by the reinforcement and the remainder by the matrix. Provided the response of the composite remains elastic, this proportion will be independent of the applied load and it represents an important characteristic of the material. It depends on the volume fraction, shape and orientation of the reinforcement and on the elastic properties of both constituents. The reinforcement may be regarded as acting efficiently if it carries a relatively high proportion of the externally load. This can result in higher strength, as well as greater stiffness, because the reinforcement is usually stronger, as well as stiffer than the matrix.

The mechanical properties of the composite are also dependent upon the efficiency of the matrix in transferring the load to the reinforcement and are therefore related to the quality of the fibre/matrix bond. It is important to be able to control the degree of bonding between the matrix and the reinforcement. The important types of interfacial bonding are classified as follows: mechanical bonding, physical bonding and chemical bonding [55]. Two general ways of obtaining an optimum interfacial bond involve fibre or reinforcement surface treatments or modification of matrix composition. It should be emphasised that maximising the bond strength is not always the goal. In brittle matrix composites, a bond too strong would cause embrittlement [55].

Tensile stress - strain behaviour - longitudinal loading

Mechanical responses of continuous and aligned fibre composites depend on several factors including the stress–strain behaviours of fibre and matrix phases, the phase volume fractions, and, in addition, the direction in which the stress or load is applied. Furthermore, the properties of a composite having its fibres aligned are highly anisotropic, that is, dependent on the direction in which they are measured. It is first considered the stress–strain behaviour for the situation wherein the stress is applied along the direction of alignment, the longitudinal direction (direction 1- Fig. 1.12.).

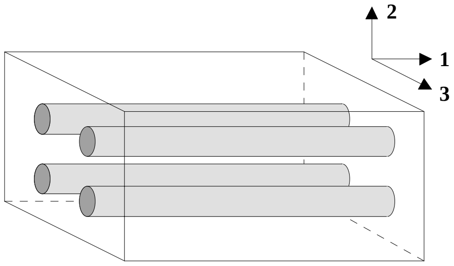

Figure 1.12. Schematic illustration of a composite containing aligned continuous fibres.

To begin, assume the stress versus strain behaviours for fibre and matrix phases that are represented schematically in Figure 1.13.a) [56]; in this treatment the fibre it is considered to be totally brittle and the matrix phase to be reasonably ductile. Also indicated in this figure are fracture strengths in tension for fibre and matrix, σ_f^* and σ_m^*, respectively, and their corresponding fracture strains, ε_f^* and ε_m^*; furthermore, it is assumed that $\varepsilon_m^* > \varepsilon_{f,}^*$ which is normally the case.

A fibre-reinforced composite consisting of these fibre and matrix materials will exhibit the uniaxial stress–strain response illustrated in Figure 1.13.b); the fibre and matrix behaviours from Figure 1.13.a) are included to provide perspective.

In the initial Stage I region, both fibres and matrix deform elastically; normally this portion of the curve is linear. Typically, for a composite of this type, the matrix yields and deforms plastically (at ε_{ym}, Figure 1.13.b)) while the fibres continue to stretch elastically, because the tensile strength of the fibres is significantly higher than the yield strength of the matrix. This process constitutes Stage II as noted in the figure, which stage is ordinarily very nearly linear, but of diminished slope relative to Stage I. Furthermore, in passing from Stage I to Stage II, the proportion of the applied load that is borne by the fibres increases. The onset of composite failure begins as the fibres start to fracture, which corresponds to a strain of approximately ε_f^* as noted in Figure 1.13.b). Initial composite failure is not catastrophic for a couple of reasons. First of all, not all fibres fracture at the same time. In addition, even after fibre failure, the matrix is still intact inasmuch as $\varepsilon_f^* < \varepsilon_m^*$ (Figure 1.13.a)). Thus, these fractured fibres, which are shorter than the original ones, are still embedded within the intact matrix, and consequently are capable of sustaining a diminished load as the matrix continues to plastically deform [56].

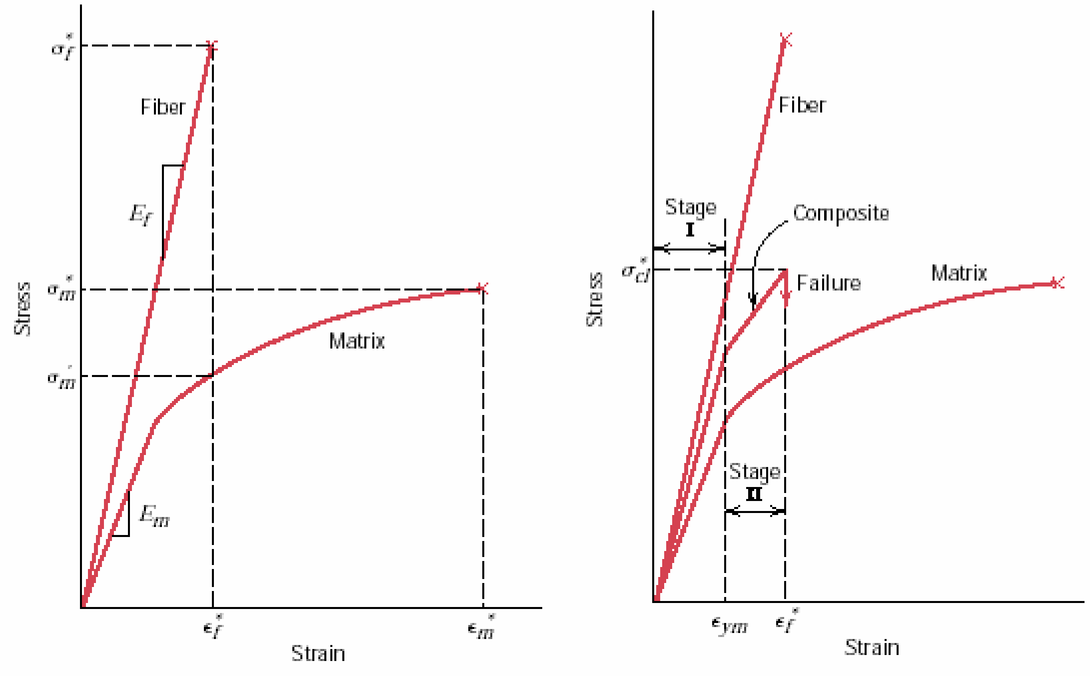

(a) (b)

Figure 1.13. a) Schematic stress-strain curves for brittle fibres and ductile matrix materials. Fracture stresses and strains for both materials are noted. b) Schematic stress-strain curve for an aligned fibre-reinforced composite that is exposed to a uniaxial stress applied in the direction of alignment; curves for the fibre and matrix materials shown in part a) are also superimposed [56].

Elastic behaviour - longitudinal loading

Now the elastic behaviour of a continuous and oriented fibrous composite that is loaded in the direction of fibre alignment direction is being considered [51, 56]. First of all, it is assumed that the fibre–matrix interfacial bond is very good, such that deformation of both matrix and fibres is the same (an *isostrain* situation). Under these conditions, the total load sustained by the composite F_c is equal to the loads carried by the matrix phase F_m and the fibre phase F_f, or

$$F_c = F_m + F_f \tag{1.2.}$$

From the definition of stress, $F = \sigma A$, expressions for F_c, F_m, and F_f in terms of their respective stresses (σ_c, σ_m, and σ_f) and cross-sectional areas (A_c , A_m, and A_f) are possible. Substitution of these into equation 1.2. yields

$$\sigma_c A_c = \sigma_m A_m + \sigma_f A_f \tag{1.3.}$$

and then, dividing through by the total cross-sectional area of the composite, A_c ,

$$\sigma_c = \sigma_m \frac{A_m}{A_c} + \sigma_f \frac{A_f}{A_c} \tag{1.4.}$$

where A_m/A_c and A_f /A_c are the area fractions of the matrix and fibre phases, respectively. If the composite, matrix, and fibre phase lengths are all equal, A_m/A_c is equivalent to the volume fraction of the matrix, V_m and likewise for the fibres, $V_f = A_f /A_c$. Equation 1.4. now becomes

$$\sigma_c = \sigma_m V_m + \sigma_f V_f \tag{1.5.}$$

The previous assumption of an isostrain state means that

$$\varepsilon_c = \varepsilon_m = \varepsilon_f \tag{1.6.}$$

and when each term in Equation 1.6. is divided by its respective strain it is obtained:

$$\frac{\sigma_c}{\varepsilon_c} = \frac{\sigma_m}{\varepsilon_m} V_m + \frac{\sigma_f}{\varepsilon_f} V_f \tag{1.7.}$$

Furthermore, if composite, matrix, and fibre deformations are all elastic, then $\sigma_c/\varepsilon_c = E_c$, $\sigma_m/\varepsilon_m = E_m$, and $\sigma_f/\varepsilon_f = E_f$, the E's being the modulus of elasticity for the respective phases. Substitution into equation 1.7. yields an expression for the modulus of elasticity of a continuous and aligned fibrous composite in the *direction of alignment* (or *longitudinal direction*), E_1, as

$$E_1 = E_m V_m + E_f V_f \tag{1.8.a}$$

or

$$E_1 = E_m (1 - V_f) + E_f V_f \tag{1.8.b}$$

since the composite consists of only matrix and fibre phases; that is, $V_m + V_f = 1$.
The equation 1.8.a is known as the *rule of mixture* expression for the apparent Young's modulus in the direction of the fibres.
Marked increases in the Young's modulus may be achieved by reinforcing metals. The composite becomes stiffer as the proportion of reinforcement increases [57].
Other properties, including density, also have this dependence on volume fractions.

Although not further referred to in the following investigations, for completeness the elastic behaviour under transverse and shear loading is described formally.

Elastic behaviour - transverse loading

A continuous and oriented fibre composite may be loaded in the transverse direction (direction 2- Fig. 1.12.); that is, the load is applied at a 90° angle to the direction of fibre alignment [51, 56]. For this situation the stress σ to which the composite as well as both phases are exposed is the same, or

$$\sigma_c = \sigma_m = \sigma_f = \sigma \tag{1.9.}$$

This is termed an *isostress* state. Also, the strain or deformation of the entire composite ε_c is

$$\varepsilon_c = \varepsilon_m V_m + \varepsilon_f V_f \tag{1.10.}$$

but, since $\varepsilon = \sigma/E$,

$$\frac{\sigma}{E_2} = \frac{\sigma}{E_m} V_m + \frac{\sigma}{E_f} V_f \tag{1.11.}$$

where E_2 is the modulus of elasticity in the transverse direction. Now, dividing through by σ yields

$$\frac{1}{E_2} = \frac{V_m}{E_m} + \frac{V_f}{E_f} \tag{1.12.}$$

This reduces to

$$E_2 = \frac{E_m E_f}{V_m E_f + V_f E_m} = \frac{E_m E_f}{(1 - V_f) E_f + V_f E_m} \tag{1.13.}$$

which is the mechanics of materials expression for the apparent Young's modulus in the direction transverse to the fibres.

Elastic behaviour - shear loading

The shear modulus of a continuous and oriented fibre composite can be predicted in a similar way, by evaluating the net shear strain induced when a shear stress is applied to the composite, in terms of the individual displacement contributions from the two constituents [55, 59]. It is important to understand the nomenclature convention, which is used. A shear stress designated τ_{ij} ($i \neq j$, i, j=1,2,3) refers to a stress acting in the i-direction on the plane with a normal in the j-direction. Similarly, a shear strain γ_{ij} is a rotation towards the i-direction of the j-axis. The shear modulus G_{ij} is the ratio of τ_{ij} to γ_{ij}. As the composite body is not rotating, the condition $\tau_{ij} = \tau_{ji}$ most hold. In addition, $G_{ij} = G_{ji}$ so that $\gamma_{ij} = \gamma_{ji}$. Since the 2-and 3-directions (Fig. 1.12.) are equivalent in the aligned fibre composite, it follows that

$$G_{12} = G_{21} = G_{13} = G_{31}. \tag{1.14.}$$

The stresses τ_{12} and τ_{21} are assumed to operate equally within both of the constituents, it follows that

$$\tau_{12} = \tau_{12f} = \gamma_{12f} G_f = \tau_{12m} = \gamma_{12m} G \tag{1.15.}$$

where γ_{12f} and γ_{12m} are the individual shear strains in the two constituents. The total shear strain is found by summing the two contributions to the total shear displacement in the 1-direction

$$G_{12} = \frac{G_m G_f}{V_m G_f + V_f G_m} \tag{1.16.}$$

which is the same type of expression as was obtained for the transverse Young's modulus, E_2.

Longitudinal tensile strength

We now consider the strength characteristics of continuous and aligned fibre-reinforced composites that are loaded in the longitudinal direction. Under these circumstances, strength is normally taken as the maximum stress on the stress–strain curve, Fig. 1.13.a); often this point corresponds to fibre fracture, and marks the onset of composite failure. Failure of this type of composite material is a relatively complex process, and several different failure modes are possible. The mode that operates for a specific composite will depend on fibre and matrix properties, and the nature and strength of the fibre–matrix interfacial bond.

If we assume that $\varepsilon^*_f < \varepsilon^*_m$ (Figure 1.13.), which is the usual case, then fibres will fail before the matrix. And once the fibres have fractured, the majority of the load that was borne by the fibres is now transferred to the matrix. This being the case, it is possible to adapt the expression for the stress on this type of composite, equation 1.5., into the following expression for the longitudinal strength of the composite, σ^*_{cl}:

$$\sigma^*_{cl} = \sigma'_m(1 - V_f) + \sigma^*_f V_f \tag{1.17.}$$

Here σ'_m is the stress in the matrix at fibre failure (as illustrated in Figure 1.13.a) and, as previously, σ^*_f is the fibre tensile strength.

As for stiffness, the strength is generally higher with increased volume fraction of reinforcement [57].

1.3.1.2. Thermal characteristics

Thermal conductivity

There are many applications in which the electrical and/or thermal conductivities of metals are exploited. Since the use of ceramic inclusions can bring about significant strengthening, there is interest in predicting how the conductivity of the composite will vary with reinforcement properties, volume fraction, interfacial structure etc. Heat flows within a material by the transmission of phonons and free electrons. Both of these carriers have a certain mean free path λ between collisions (energy exchange events) and an average velocity v. The thermal conductivity K is related to these parameters by a simple equation derived from kinetic theory

$$K = \frac{1}{3} c_V v \lambda \tag{1.18.}$$

where c_V is the volume specific heat of the carrier concerned. The mean free path of a phonon is structure-sensitive and can be very large in pure specimens of high perfection and large grain size. Single crystals of materials as diamond and SiC can therefore have very high thermal conductivity. With the exception of such cases, metals have the highest conductivities because electrons usually have a much larger mean free path than phonons. This can, however, be substantially reduced by the presence of solute atoms and various defects which cause electron scattering.

The effective conductivity of composite structures has been the subject of prolonged study [54]. Many of the treatments developed are specific to a particular geometrical arrangement of the constituents.

The longitudinal conductivity of a continuous fibre composite is given by a simple weighted mean rule of mixtures while the transverse conductivity reduces to the expression

$$K_{ct} = K_m + \frac{K_m\left(K_f - K_m\right)V_f}{K_m + \left(1 - V_f\right)\left(K_f - K_m\right)/2} \tag{1.19.}$$

where *m* and *f* refer to matrix and fibre respectively [54].

<u>*Thermal expansion*</u>

The overall thermal expansion characteristics of a composite can be controlled by controlling the proportion of reinforcement and matrix and the distribution of the reinforcement in the matrix. Many researchers have proposed models to predict the coefficients of thermal expansion of composites, determined experimentally these coefficients, and analysed the general thermal expansion characteristics of metal matrix composites [55]. Unidirectionally aligned fibrous composites have two (or sometimes three) thermal expansion coefficients: α_{cl} in the longitudinal direction and α_{ct} in the transverse direction. Schapery (1969) derives the following expressions for the expansion coefficients of a fibrous composite [55]:

$$\alpha_{cl} = \frac{\alpha_m E_m V_m + \alpha_f E_f V_f}{E_m V_m + E_f V_f} \tag{1.20.}$$

$$\alpha_{ct} \cong \left(1 + \nu_m\right)\alpha_m V_m + \left(1 + \nu_f \alpha_f V_f\right) - \alpha_{cl}\bar{\nu} \tag{1.21.}$$

where ν_m is the matrix Poisson’s ratio; α_f is the thermal expansion coefficient for the fibre,
ν_f is the fibre Poisson’s ratio; α_m is the thermal expansion coefficient for the matrix
and $\bar{\nu} = \nu_f V_f + \nu_m V_m$.

To predict the coefficient of thermal expansion is complicated because of the structure of the composite, interface, and the matrix plastic deformation due to internal thermal stresses. In general, ceramic reinforcements have a coefficient of thermal expansion α smaller than that of most metallic matrices. Therefore reinforcement of metals with ceramic fibres or particles leads to a reduction in *α*. For example, *α* for SiC is about one-fifth and one-fourth of that for aluminium and magnesium respectively [57].

Problems can arise from the large differences in the coefficients of thermal expansion between the matrix and the reinforcement. This means that when the composite is subjected to a temperature change the mismatch in the expansion coefficients lead to thermal stresses generation.

Chawla and Metzger (1972), working with a single copper matrix containing large-diameter tungsten fibres showed the importance of thermal stresses in MMCs. They showed that near the fibre the dislocation density was much higher in the matrix than the dislocation density far away from the fibre. This arises because of the plastic deformation in response to the thermal stresses generated by the thermal mismatch between the fibre and the matrix. The existence of a plastically deformed zone containing high dislocation density in a metallic matrix near the reinforcement has been confirmed by transmission electron microscopy by a number of researchers, both in fibrous and particulate metal matrix composites [55]. Thermal mismatch is indeed something that is difficult to avoid in any composite.

1.3.2. Advantages of MMC's and applications

Whilst improving also other desirable properties of metals such as ease of fabrication, ductility, high thermal and electrical conductivity should preferably be maintained. Metals are generally noted for their good ductility and toughness, but unfortunately both these properties are degraded by the incorporation of reinforcement. The thermal and electrical conductivities of the reinforcement are often less than that of the metallic matrix and hence, composites have lower values for these parameters than the monolithic metal. Although there is a significant reduction in the conductivities on reinforcing metals, the values remain much greater than those for most polymers and polymer matrix composites [57]. Furthermore, the desired combination of properties needs to be obtained at minimum cost.

Depending on the specific application, MMCs as a class of materials offer significant potential advantages compared to other material classes. The major advantages are summarised in table 1.2. [52].

MMCs compared with:	**MMCs Advantages**	**MMCs Disadvantages**
un-reinforced materials	-higher specific strength -higher specific stiffness -improved high temperature creep resistance -improved wear resistance	-lower toughness and ductility -more complicated and expensive production methods
polymer matrix composite	-higher transverse strength -higher toughness -better damage tolerance -improved environmental resistance -higher thermal and electrical conductivity -higher temperature capability	-less developed technology -smaller data base of properties -higher cost
ceramic matrix composites	-higher toughness and ductility -ease of fabrication -lower cost -high thermal conductivity	-inferior high temperature capability

Table 1.2. MMCs advantages and disadvantages compared with other material classes

The initial driving force for the development of MMCs were in aerospace and defence applications where high performance materials were required in relatively low volumes, thus justifying high costs. Whilst this field of application continues to be of great interest, there have been strong moves in recent years to introduce the MMC concept into higher volume applications, notably the automotive field where larger volume production and lower materials cost are required. In addition, various other more specialised applications exist.

The commercial titanium alloys, characterised by their low specific weight, high strength and excellent resistance to chemical attack, were introduced in the aerospace industry as materials

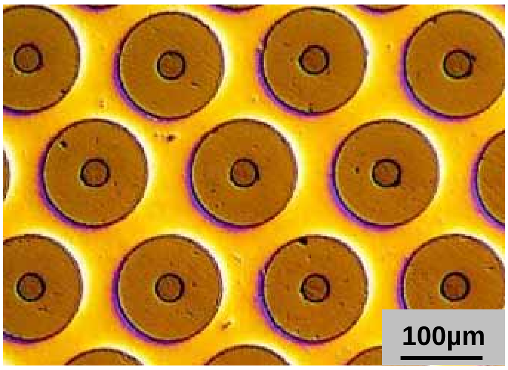

Figure 1.14. SCS-6/Ti-metal composite [58]

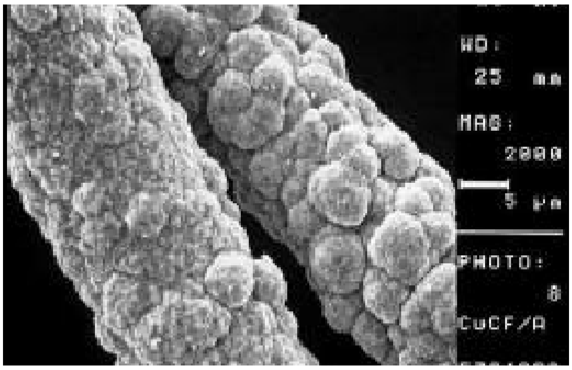

Figure 1.15. Copper coated carbon fibres [59]

for use in jet engines as compressor stage turbine blades working at temperatures up to ca. 300°C. A Ti-alloy reinforced with high strength, high modulus, high temperature resistance SiC-fibres offers the possibility to satisfy the increasing requirement in modern jet engines for even greater weight reduction and higher service temperatures [60].
Figure 1.14. shows a micrograph of SCS-6/Timetal 834 composite produced using a method developed in the DLR (German Aerospace Center) [61]. In this process the SiC-fibres are coated with Ti-alloy matrix material by magnetron sputtering at 500°C for 8h. The coated fibres are bundled and encapsulated in a Ti-alloy tube and evacuated. HIP'ing is carried out for 30 min, at a temperature of 900°C and a pressure of 190 MPa [60].

Metal matrix composites can be tailored to have optimal thermal and physical properties to meet the requirements of electronic packaging systems. Continuous boron fibre reinforced aluminium composites have been used as heat sinks in electronic chip carrier multilayer boards. Unidirectionally aligned, pitch-based carbon fibres in an aluminium matrix can have very high thermal conductivity along the fibre direction. Such a C/Al composite can find practice in heat transfer applications where weight reduction is an important consideration, for example, in high-density, high-speed integrated-circuit packages for computers and in base plates for electronic equipment [55].

Copper-based materials are widely used if thermal or electrical conductivity is required. However, use of pure copper has some limitations if its high coefficient of thermal expansion (CTE) forbid it is used. The carbon fibre reinforced copper matrix composite (Cu-C_f MMC) may fulfil these requirements because it can use good properties of both constituents – high conductivity of copper and high stiffness, a negative axial CTE and a low density of carbon fibres [62, 63]. The most promising applications of the Cu-C_f MMC e.g. heat sinks, packaging for high voltage chips, packaging base plates and carrier plates of electronic box closures can be found in the electronic industry [64]. In this applications heat dissipation is important because new integrated circuits and other powerful electronic parts can generate large amount of heat.
The composite's properties can be tailored to the required values by changing the volume fraction and arrangement of the fibres as well as by different production parameters [65-68]. Different technologies have been used to prepare short fibre composites samples and to examine the feasibility of producing full-density Cu/C composites with relatively high carbon-fibre contents [59, 69]. A promising production route is electroless copper coating of short carbon fibres (Fig. 1.15.) followed by annealing in a reducing atmosphere and hot pressing. By the electroless method it is possible to deposit a copper layer on carbon fibre at a thickness of several tenths of a micrometer. A thicker layer can be deposited by galvanic coating [70].

In recent years, SiC particles have attracted much attention as reinforcements in copper matrix composites not only for electronic packaging but also for other applications. Copper matrix composites reinforced with SiC particles can exhibit high thermal conductivity and low CTE by combining the thermal conductivity of copper and the CTE of silicon carbide. The feasibility of copper matrix composites containing SiC particles being prepared by using a powder metallurgy method for electronic packaging materials is studied in [71].

SiC-fibres copper-matrix composite materials make the use of the strength and elastic modulus of SiC fibres possible in combination with the high heat conductivity and middle density of copper, if during the processing the properties of the interface are adequate adjusted and fibre damages are avoided at the same time. In fusion applications come the demands that the high heat conductivity of the pure copper should be obtained for the composite material and as well to facilitate operation at high temperatures (> 500°C): The divertor of the fusion reactor experiences high thermal loads from the fusion plasma, a heat flow which needs to be efficiently transferred through the heat sink into the cooling agent. Therefrom high requirements result for the heat sink material. For efficient energy conversion its thermal conductivity should be above 200 $W\,m^{-1}\,K^{-1}$ under neutron irradiation at an operation temperature which permits the use of the cooling agent (water) at a temperature level as high as possible.

Processing and characterisation of SiC-Cu composite with application in fusion will be discussed in this thesis.

1.3.3. MMC processing

Certain requirements are essential for any production route [52]:

- the reinforcement must be distributed in a controlled manner in the metal matrix, i. e. either uniformly distributed throughout or placed in designated locations of the component
- minimal porosity and full density should result in the final component
- typically, volume fractions of 0.1-0.6 of reinforcement need to be incorporated in the matrix
- reactions at the reinforcement/matrix interface should be controlled to promote optimum bond strength and avoid reinforcement degradation
- the reinforcement should be incorporated into matrix without breakage. This is a particularly important factor when processing continuous fibre and whisker reinforced MMCs
- during composite joining and forming, minimal reinforcement degradation of either chemical or physical means should result. Reinforcement alignment and distribution should be maintained
- the route should be as flexible as possible in terms of matrices and reinforcements to which it can be applied
- subsequent post-fabrication heat treatments should be allowed for
- the route should be capable of producing components with a high degree of reproducibility at minimum product variability at minimum cost and maximum productivity
- flexibility in the range of shapes capable of being produced is highly desirable
- any proposed process route should be amenable to scale-up

In considering any proposed application for a particular MMC, it is necessary to bear in mind the available means of producing such a material. The factors involved in the production of an MMC can have a critical influence on the cost of the final MMC component, the type of component that can be produced and, therefore, the applications for which a given MMC can be used.

Production of a final component manufactured from MMCs involves [52]: bulk production of the composite from its component materials, secondary working of the composite material into some form/shape and joining of the composite material, leading to final fabrication of the engineered component.

With the multitude of possible matrix and reinforcement combinations and composite products available, there are a large number of production routes for MMCs. They differ considerably, depending on whether they are aimed at continuous or discontinuous MMC production. Continuous reinforcements for MMCs take the form of either single filaments of large diameter (in excess of 100 µm) or of small filaments (typically of 1-20 µm diameter) produced in tows or yarns of fibres, called multifilaments.

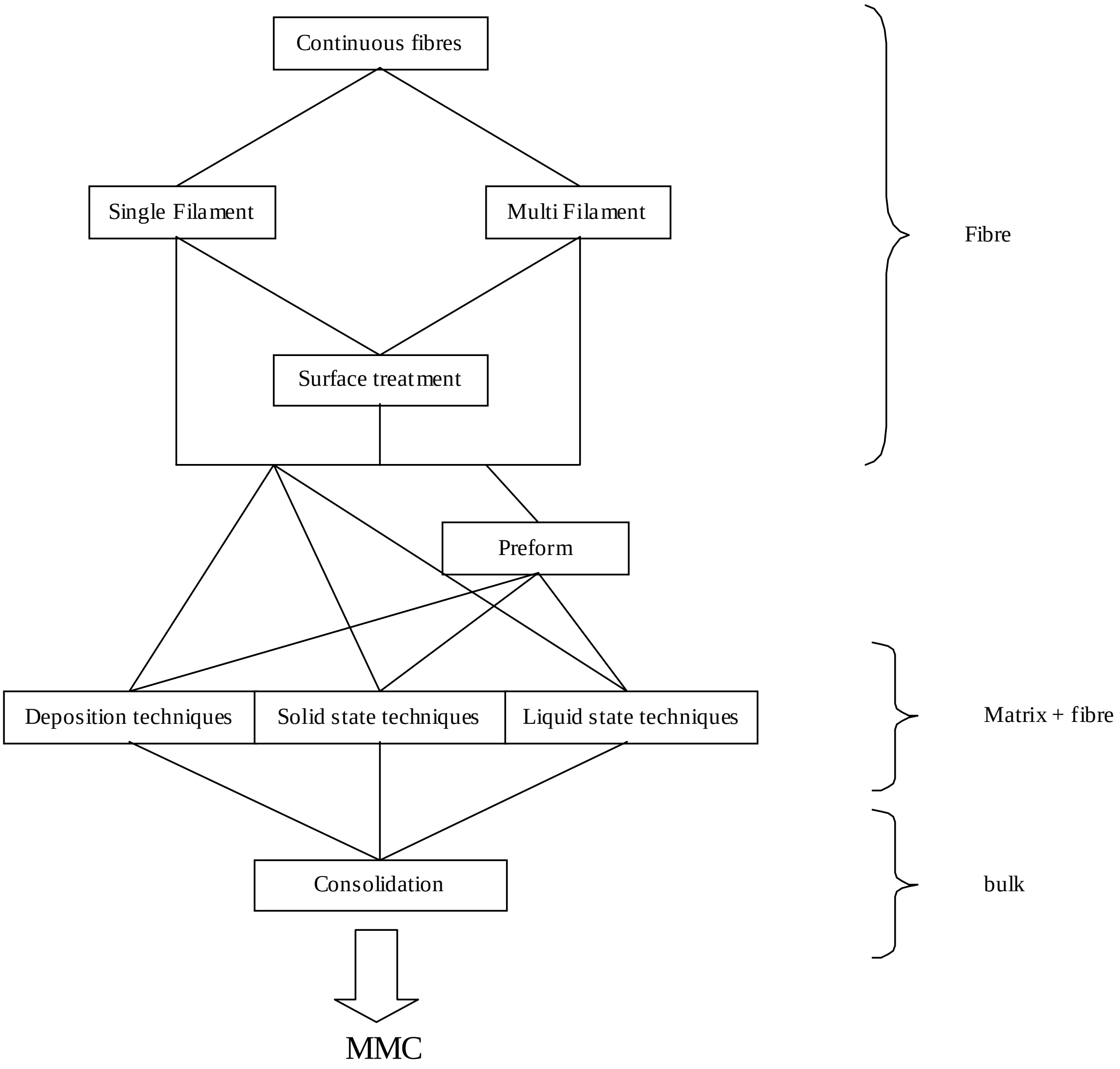

Figure 1.16. Principle of composite processing

Filaments may be pre-coated with matrix material, affording protection and ease of handling. Matrix coating is particularly useful in the production of high volume fractions of fibres where filaments overlap would otherwise cause serious problems. Achievement of matrix coating of filaments on a large scale at a reasonable cost and throughput is, however, a major concern.

For either single filament or multifilament reinforcements, the production sequence is either the formation of some form of preform or the formation of an array with binders. The preform can take the form of a sheet, a tape or a wire.

The main methods of preform production are plasma spraying and electroforming, methods that are explained later.

Most processes for fabricating MMCs involve processing in the liquid and solid state. Some may involve a variety of deposition techniques or an in situ process of incorporating a reinforcement phase. Metals with melting temperatures that are not too high, such as aluminum, can be incorporated easily as a matrix by liquid route. Some important liquid-state processes are: *casting* or *liquid infiltration* (involves infiltration of a fibre bundle by liquid metal) and *squeeze casting* or *pressure infiltration* (involves forcing the liquid metal into a fibrous preform) [55].

Many solid state techniques are available. Diffusion bonding is a common solid state welding technique used to join similar or dissimilar metals. Interdiffusion of atoms from clean metal surfaces in contact at an elevated temperature leads to welding. There are many variants of the basic diffusion bonding process; however, all of them involve a step of simultaneous application of pressure and high temperature.

Several deposition techniques are available: chemical vapour deposition (CVD), physical vapour deposition (PVD), spray deposition, immersion plating and electroplating.

Chemical vapour deposition (CVD) involves the decomposition of vapour species precursors, from which the metal is deposited in a solid form. Using metal organic compounds, this process can be operated at relatively low temperatures. It is, however, a slow and costly process and adequate control of the chemical deposition reactions can present problems.

Physical vapour deposition (PVD) include direct evaporation and condensation, ion beam deposition and sputtering. In ion beam deposition, the material is deposited from an ionised beam; in sputtering, a high ion current generates a flux of atoms by physical sputtering.

A spray deposition operation, typically, consists of winding fibres onto a foil-coated drum and spraying molten metal onto them to form a monotape. The source of molten metal may be powder or wire feedstock, which is melted in a flame, arc, or plasma torch. The advantages of spray deposition are easy control of fibre alignment and rapid solidification of the molten matrix.

Immersion plating is similar to infiltration casting except that fibres tows are continuously passed through baths of molten metal, slurry, sol, or organo-metallic precursors.

Electroplating produces a coating from a solution containing the ion of the desired material in the presence of an electric current. Fibres are wound on a mandrel, which serves as the cathode, and placed into the plating bath with an anode of the desired matrix material. The advantage of this method is that the temperatures involved are moderate, high density material can be obtained, better fibre-matrix contact and bonding is usually found and no damage is done to the fibres. Problems with electroplating involve void formation between fibres and between fibre layers, possible contamination from impurities from the plating baths, adhesion of the deposit to the fibre may be poor, and there are limited numbers of alloy matrices available for this processing.

Whether filaments, matrix coated filaments or preforms are employed as the source of the reinforcement, a consolidation step with the matrix material is used to produce the final MMC material. The principal techniques employed for this consolidation step are based on either liquid state or solid state. The available liquid state techniques are hot molding (liquid phase diffusion bonding, liquid phase sintering, liquid phase hot pressing), braze bonding and liquid infiltration methods. The most widely used solid state techniques are diffusion bonding, hot and cold roll bonding, high energy rate forming and hot isostatic pressing.

Hot isostatic pressing (HIP) technique is used as consolidation step in this work. It is defined as a process of forming or bonding materials at high temperatures with high pressures acting on all surfaces simultaneously and equally. Hot isostatically pressed parts are fully dense and essentially have no porosity; as a result they exhibit improved mechanical properties.

In the hot isostatic pressing process, the workpiece is placed inside a furnace, which is contained within a pressure vessel. The workpiece is then heated to a softened state and pressurised with an inert gas such as argon or helium. The gas pressure exerts a great force equally (iso) distributed over the part to attain full density. Temperatures, pressures and holding time periods differ as a function of the various materials being HIPed. HIP cycles for production must be reliable and reproducible for effective processing. The HIP process is a proven and accepted method of economically forming materials.

In the end the composite with the requested properties according to the intended application is processed.

1.3.4. Reactive interfaces in Cu-based MMCs

From literature it is known that the problem appearing during the processing of a carbon-copper composite is that copper wets carbon surfaces poorly [72] so that the interface is extremely weak. The wetting angle lies between 120° and 140°, and the adhesion is achieved only by van-der-Waals forces [73].

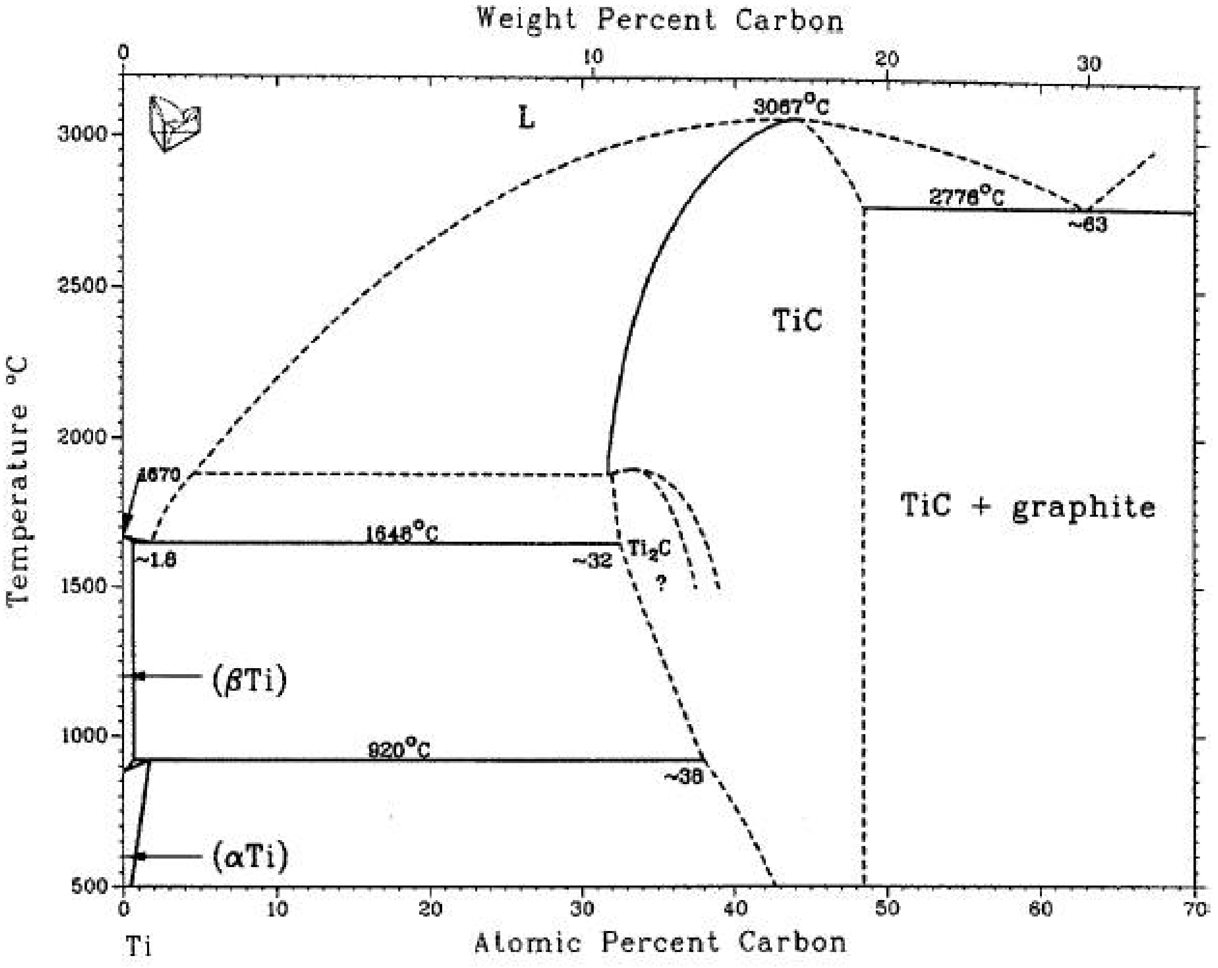

Figure 1.17. Ti-C phase diagram [78]

A possible solution for the improvement of the interfacial strength is forcing the fibre surface to react with the matrix or making the matrix dissolve the carbon surface. Possible reaction elements are titanium or chromium deposited as interlayer between carbon fibre and copper.

A quantity of 0.1 at% chrome alloying copper is enough to reach the wetting condition (wetting angle <90°). For titanium a quantity of 10 at% is indicated in literature [74].

An improvement of the wetting behaviour can be achieved also by modification of the carbon surface [75]. The adhesion of the copper on carbon was reported to be increased by deposition of a thin titanium or chromium layer [76, 77].

The binary Ti-C phase diagram is shown in Fig. 1.17. The Ti-C system is a well established system which has α-Ti (hexagonal structure) and β-Ti (cubic structure) on the titanium side where only a very limited solubility of carbon exists [79].

The interaction of titanium and carbon is investigated in [80]. As TiC is first formed at C-concentrations of about 30 at%, there are understoichiometric carbides with carbon atoms missing in the lattice and also Ti$_2$C is produced. Titanium and carbon do not combine in a 1:1 ratio. Rather carbon and TiC build a mixture, when the carbon concentration exceeds 48.8 at% (Fig. 1.17.).

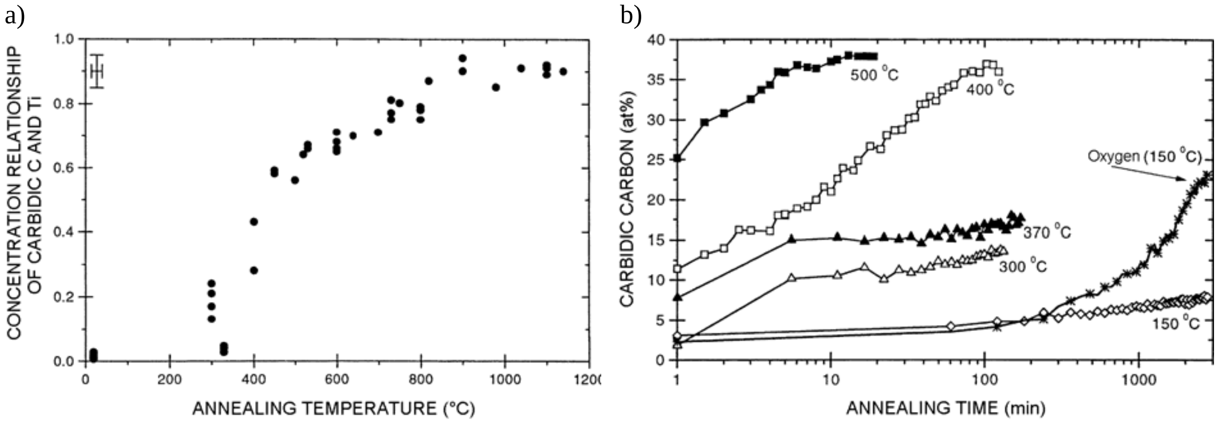

Figure 1.18. a) Temperature dependence of carbide formation, b) Time dependence of carbide formation. (Curves below 400°C are irrelevant for this work as they are subjected to surface effects that can be excluded by an additional copper coating.) [80]

Supplying an amount of titanium on the outer carbon-layer of the fibre, titanium carbide will be formed during adequate heat treatment.

Depending on the annealing temperature, different grades of understoichiometric carbides are formed beginning already at 300°C with a low degree of carbidisation (Fig. 1.18.a).

Looking at the time-dependence shown in figure 1.18.b) it can be seen that the time to reach this temperature depending level of carbidisation is shorter the higher the annealing temperature is. Heating at temperatures higher than 400°C for about 100 minutes seems to be enough to cause extensive titanium carbide formation.

As TiC is a stable compound it is not found to solubilise in copper. On the other hand a limited solubility of copper exists in TiC, giving an option to raise the adhesion between carbide and copper [79].

1.3.5. Push-out test

A critical issue in the successful applications of MMCs is the behaviour of fibre/matrix interfaces. The principal methods of characterising the interface can be classified into three broad categories, microstructural, chemical and mechanical. The first two methods can help only in understanding the architecture and chemical composition of the region between fibre and matrix. In order to obtain quantitative information about the strength of the interface, mechanical tests are required. Several techniques including microindentation [81], fibre push-out, re-push and pull-out tests [82-84] and debonding length measurements [85] are reported in the literature for measuring the interfacial properties such as interfacial shear strength τ_d, frictional shear stress τ_f and interfacial debonding energy [54, 85, 86]. Fibre push-out tests have been increasingly used in recent years for studying the interfacial shear behaviour of composites [87-95].

The different stages involved in a typical *depth-controlled* push-out test are shown in Fig. 1.20. with different corresponding load/displacement curves in Fig. 1.19. [adapted from 93 and 96]. When a compressive load is applied to the top face of the fibre as shown in the figure 1.20., shear stresses are introduced at the interface with a maximum value occurring at the region near the top face. Initially the load increases linearly and the fibre remains essentially fully bonded to the matrix. When the applied load reaches P_d, the shear stress in the upper region reaches a critical value and debonding initiates, causing a change in slope (Fig. 1.19. A, C). This is represented in stage (a). Once debonding occurs, the shear stress in the debonded zone drops, and the region of maximum shear stress moves away from the top face when the applied load is increased. This results in a nonlinear debonding progression as represented in stage (b). The stage of increasing load after initiation of debonding corresponds to additional debonding and frictional sliding of the debonded section of the fibre. If the debond initiation load is significantly different from that required for propagation, a load drop signifying the initiation event could appear on the load-displacement plot (dotted). If the debond initiation and propagation strengths are not significantly different, it will be necessary to identify the debond initiation load from the beginning of nonlinearity. If the difference between initiation load and propagation load is very large, upon initiation, the crack may propagate completely through the specimen in a catastrophic fashion. In such a case, the load-displacement curve is expected to be linear to the peak load, then drop to the purely frictional portion of the curve (B) [83]. The magnitude of the initial debonding load and the subsequent load drop associated with the debonding event were found variable for the same SiC-borosilicate glass composite by Bright [82].

When the load reaches P_{max}, the maximum shear stress reaches the critical value at the bottom face (stage (c)). As a result the entire length of the fibre gets debonded, and the fibre is pushed out of the matrix as represented in stage (d). This can result in a sudden drop in the load because the resistance to further movement of the fibre is mainly due to friction and surface roughness (A) [96]. If the maximum load is similar to the friction force, no sudden drop appears (C). The friction load P_{fr} may sligthly increase, but generally the load decreases beyond this point as the length of the fibre within the matrix is decreased (e). Bright [82] found that a large debonding load drop was followed by a small increase in the frictional sliding load before the load started to decrease. Conversely, a small debonding drop was followed by more extensive frictional load increase before reaching the maximum friction load. This inverse relationship is clarified in the following manner. A large instantaneous load drop at debonding corresponds to a sudden increase in the fibre displacement associated with the debonding over a long section of the fibre. Accordingly, the additional frictional sliding necessary before the fibre exits is small. The frictional sliding stage was found to be characterised by fine-scale serrations on the load-displacement record [82]. In a *load-*

controlled experiment these friction data would be lost due to lack of force reduction measurement (f).

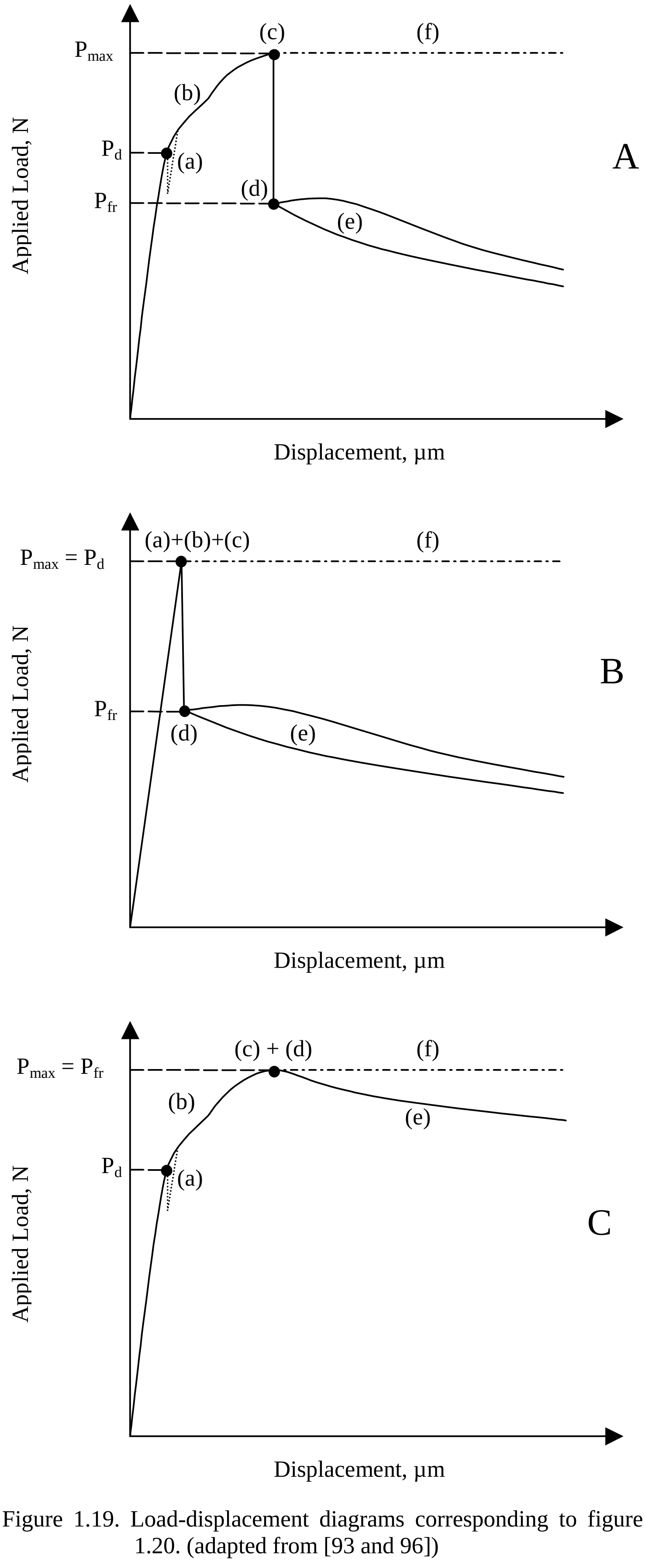

Figure 1.19. Load-displacement diagrams corresponding to figure 1.20. (adapted from [93 and 96])

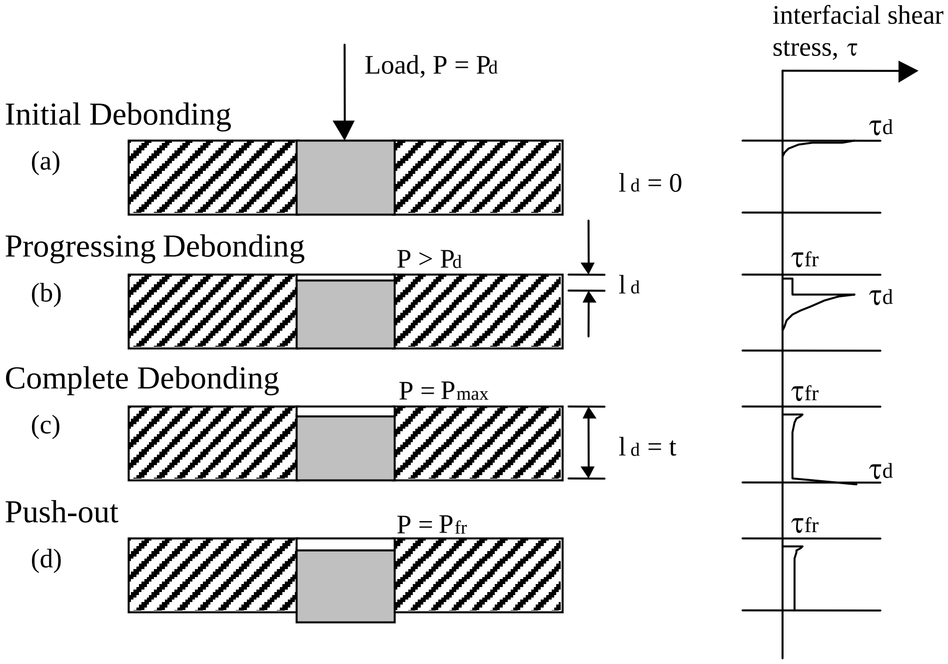

Figure 1.20. Stages in a push-out test (adapted from [93 and 96])

From the experimental load-displacement curve, the initial debonding load and the friction load are determined. The interfacial shear strength and the interfacial friction stress can be derived from these forces. The interfacial shear strength τ_d is the maximum shear stress encountered at the fibre-matrix interface before the debonding initiates (P_d). In contrast to this, the interfacial friction stress τ_{fr} describes the reactive force during fibre slip opposite to the moving direction.

For every force applied on a stressed area, the apparent mean value τ_a of the stress is given by

$$\tau_a = \frac{P_{applied}}{A_{stressed}} . \tag{1.22.}$$

In the case of a loaded fibre the perimeter surface has to be considered:

$$\tau_a = \frac{P_{applied}}{2\pi R_f L} , \tag{1.23.}$$

where R_f is the fibre radius and L the embedded fibre length.

For the more accurate determination of both interface parameters τ_d and τ_{fr}, different models have been developed which can be used to describe the process taking place at the interface during the push-out test.

The model for the determination of τ_d dates back to Greszczuk [97], 1969, and was also used by Lawrence [98] for the evaluation of pull-out tests [99]. Using shear-lag analysis they have shown that the debonding load P_d in pull-out tests can be related to the interfacial shear strength τ_d, the embedded fibre length L, the radius of the fibre R_f and a shear-lag parameter α [82, 100]. According to Greszczuk, the elastic interfacial shear stress as a function of depth along the fibre, x, is given by the following expression

$$\tau(x) = \frac{P\alpha}{2\pi R_f}\left[\coth(\alpha L)\cosh(\alpha x) - (\sinh(\alpha x))\right],\ \alpha = \left(\frac{2G_i}{b_i R_f E_f}\right)^{1/2} \qquad (1.24.)$$

where α is a parameter dependent on the relative elastic properties of the fibre and the matrix and their geometric configuration, b_i is defined by Greszczuk as the effective thickness of the interface and G_i is the interface shear modulus [97, 98].

Referring to equation (1.25.), the debonding stress is

$$\tau(x = 0 \quad and \quad P = P_d) = \tau_d = \frac{P_d}{2\pi R_f}\alpha\coth(\alpha L) \quad \text{and} \quad \tau_a = \tau_d \frac{\tanh(\alpha L)}{\alpha L}. \qquad (1.25.)$$

$$\Rightarrow \qquad P_d = \frac{2\pi R_f \tau_d}{\alpha}\tanh(\alpha L) \qquad (1.26.)$$

The equations are also applicable to the push-out tests [81].
As emphasised by Lawrence, Greszczuk implicitly assumes that debonding occurs instantaneously, in a catastrophic way (which is generally true for short embedments and/or high bonding strengths due to the stored elastic energy).
It is observed with bulk materials that two main types of failure are possible in tension or shear, namely yielding and brittle fracture. The interface between fibres and matrix can show either behaviour. Calculating τ_d, by means of the Greszczuk equation, two cases are found: τ_a depends or does not depend on the length L of the embedded fibre. In the first case, length dependent debonding strength, the maximum debonding force is a function of the embedded length according to equation (1.26.). This case corresponds to a brittle interface characterised by sudden load drops and is referred to as the elastic case.
In the second case, constant debonding strength for any length, the load required to debond the fibre is simply a linear function of the embedded length L. It looks like a matrix yielding with the load variation as a function of the embedded length given by

$$P_d = 2\pi R_f L \tau_y \qquad (1.27.)$$

with a constant debonding strength, τ_y.
Hence

$$\tau_y = \frac{P_d}{2\pi R_f L} = const. \qquad (1.28.)$$

This case does imply the plastic deformation of the matrix in the vicinity of the interface and cannot be accounted by elastic analysis model as that of Greszczuk [101]. This is referred to as the elastoplastic case.

The model used for the determination of τ_{fr} was developed by Shetty [102]. In contrast to the method proposed by Greszczuk, fibre sliding is considered. In addition, the radial deformation of the fibre under load is also taken into account. It is further assumed that a radial residual stress σ_0 exists in the composite at room temperature. This residual stress is mainly caused by the different coefficients of thermal expansion of the fibre (α_f) and the matrix (α_m). If $\alpha_m > \alpha_f$, a radial compressive stress exists after cooling from fabrication temperature. Using the coefficient of sliding friction μ, Coulomb's law of friction is valid for the interfacial friction stress:

$$\tau_{fr} = \mu \cdot \sigma_0 \tag{1.29.}$$

Shetty has analysed the frictional sliding problem using the shear-lag approach and has derived the following equation that relates the frictional sliding load P_{fr} and the embedded fibre length L:

$$P_{fr} = \frac{\pi R_f^{\,2} \sigma_0}{k} \left[\exp\left(\frac{2\mu k}{R_f} L \right) - 1 \right] \tag{1.30.}$$

where σ_0 is the radial residual stress on the filament, μ is the friction sliding coefficient at the interface, and k is a nondimensional parameter defined by the following equation:

$$k = \frac{\nu_f E_m}{E_f (1 + \nu_m)} \tag{1.31.}$$

In eq. (1.31.) E and ν are Young's modulus and Poisson's ratio, the subscripts m and f correspond to the matrix and the fibre respectively.

One interesting aspect of the sliding friction at interfaces in composites is the role of Poisson expansion and contraction of the fibres. In push-out tests, the filament expands under the compressive load and this tends to increase the compressive stress on the interface and, therefore, the sliding friction stress and the push-out force. Contrary in the case of pull-out tests, the Poisson contraction of the filament under tensile load tends to decrease the sliding friction stress and the pull-out force. Equation (1.30.) was derived by explicitly considering the effect of this Poisson expansion in the shear-lag analysis.

On the basis of equations (1.26.) and (1.30.) the interface parameters τ_d and τ_f can be determined from a series of push-out tests on specimens of variable thickness L by means of iterative regression [82, 89].

2. Materials and experimental procedures

2.1. Materials and processing

The materials developed and studied in this work are unidirectional fiber reinforced metal matrix composites, consisting of long SiC single fibres (SCS-6, Textron, diameter 140 µm) in a copper matrix. The SiC-fibres were electrolytically covered with copper and hot isostatically pressed (HIP) to be consolidated in a composite.

The HIP-based processing followed a method developed by DLR [58, 61] for titanium alloys used as metal matrix in SiC-fibre composites.

In order to study the interfacial properties, composites with and without fibre surface treatment were manufactured.

The flow chart in Fig. 2.1. offer an overview of the processing and the characterisation methods and indicates an improvement route.

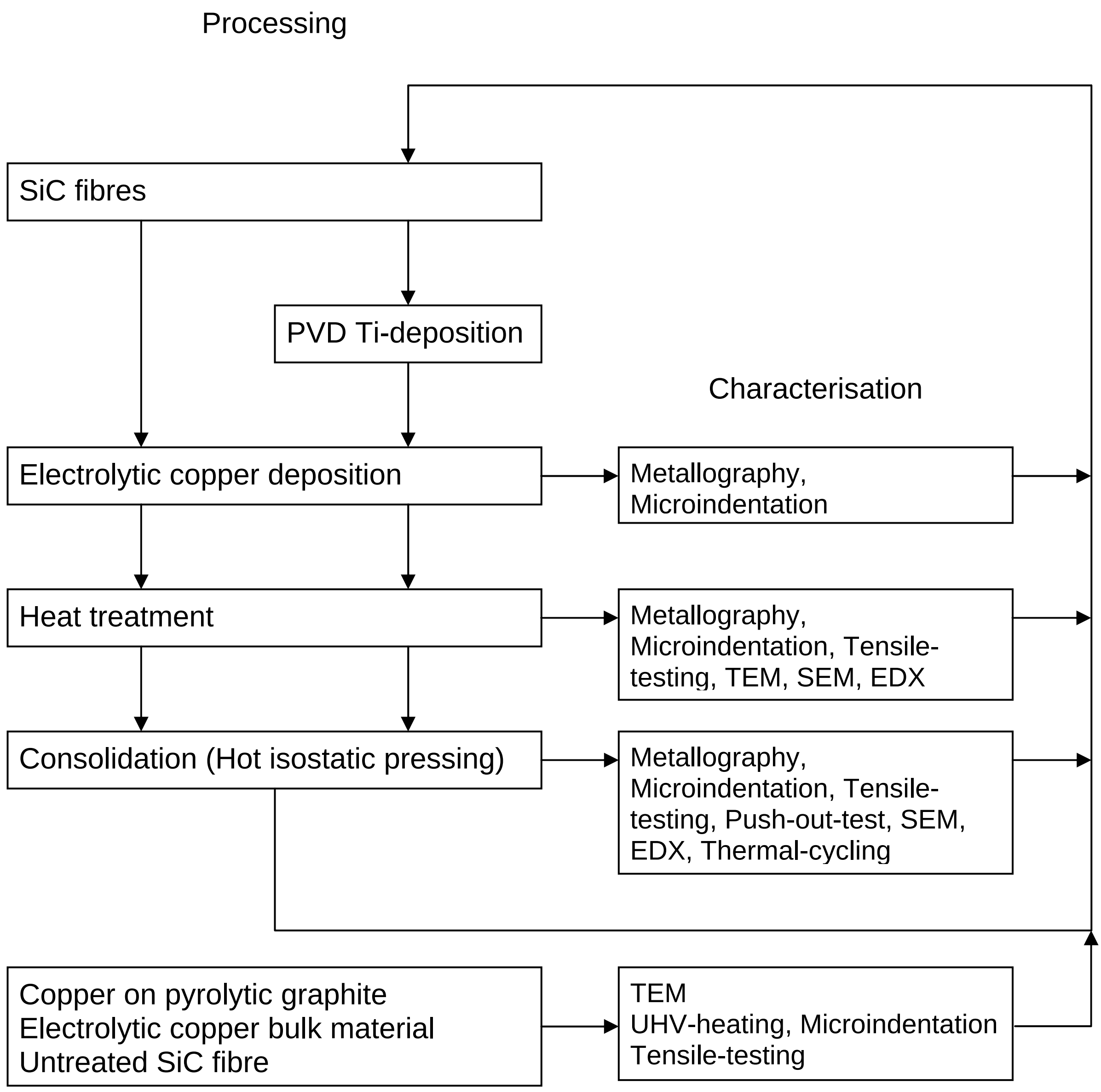

Figure 2.1. Processing and characterisation methods

2.1.1. Fibre

SiC-fibres (SCS-6) were selected to reinforce the copper because of their high strength as well as their better resistance to neutron irradiation compared to that of carbon fibres, which are both requirements for the divertor in fusion reactors.

The mechanical and physical characteristics, especially the high specific strength and modulus of the SiC-fibres, make them an interesting choice for reinforcement for metal and ceramic matrix composites. Temperatures up to 800°C have no significant effect on these properties [103], thus SiC is a key candidate for high-temperature applications. The mechanical and physical properties of the composite are influnced by the microstructural features of the fibres determined by the production method. In a fibre-reinforced metal-matrix-composite the most important parameter is the strength of the fibre because it generally determines the strength of the composite. As a result, the microstructure of the fibre, which controls its strength, plays a major role.

Some of the most widely used fibres are the SCS series of SiC-fibres (manufactured by Textron Specialty Materials, Textron Co., Inc., Lowell, MA) which became commercially available in the 1980's. The various fibres in the series differ in the nature of the outermost coating, having essentially the same core [104].

The first microstructural study of SCS fibres corresponds to Nutt and Wawner [103], who performed a transmission electron microscopy (TEM) investigation of SCS-2 fibres embedded in an Al matrix at around 550°C. As a result, Al reacted with the outermost coating of the fibres and formed a layer identified as Al_4C_3. Some years later, Lancin et al. [105] carried out TEM studies of SCS-6 fibres set in Ti-Al-V alloy, which reacted with the outermost regions of the fibres producing titanium carbide and a titanium silicide. Ning et al. studied the unprocessed SCS-6 fibres using TEM [105, 106].

The SCS-6 fibre has a diameter of 142 µm and is manufactured using single-stage CVD deposition. A schematic of the SCS-6 fibre is shown in Fig. 2.2.a) and the constitutive parts of the fibre are illustrated in Fig. 2.2.b).

The fibre's architecture can be separated into several parts. The core consists of a 33 µm diameter carbon monofilament (CMF) originally spun from a pitch-based material, which is then sealed by a 1.5 µm thick overcoat of pyrolytic carbon. The β SiC grows in columnar fashion outward from the CMF core forming two different regions. Both consist of subgrains of β SiC with close-packed {1 1 1} planes oriented radially. These subgrains have a large aspect ratio to their length in the radial direction. The first region, which extends approximately 15 µm, is relatively fine grained (10–60 nm) and from a compositional point of view, is slightly rich in carbon [107]. Although not depicted in Fig. 2.2., Ning [106] has determined that this inner region actually comprises three subzones with thicknesses of 6 µm, 4.5 µm and 4.5 µm, measured from the pyrolytic coating. The second region is approximately 35 µm wide, exhibits a coarser grain structure (70-140 nm) and is essentially stoichiometric in composition. The change in grain size is attributed to this change in chemistry. The interface between the two grown layers forms what is referred to as the mid-radius of the SiC.

The external surface of the fibre is coated with three carbonaceous layers totalling 3 µm in thickness, which are used to protect the fibre during handling and to reduce its susceptibility to strength degradation due to chemical reaction within matrices. The first layer is amorphous carbon which is approximately 0.5 µm and acts as a "seal" for the ends of the columnar β SiC. The fibre is then coated with two more carbon layers which are doped with β SiC crystallites. The thicknesses of the inner and outer C-rich layers are 1.0 µm and 1.5 µm, respectively.

The SCS-6 fibre retains essentially all of its original strength under the heat treatment conditions in an inert environment at 1000°C for up to 700 hours and therefore is suitable as reinforcement for metal matrix composite applications, wherein processing and/or heat treatment temperatures are comparable [107].

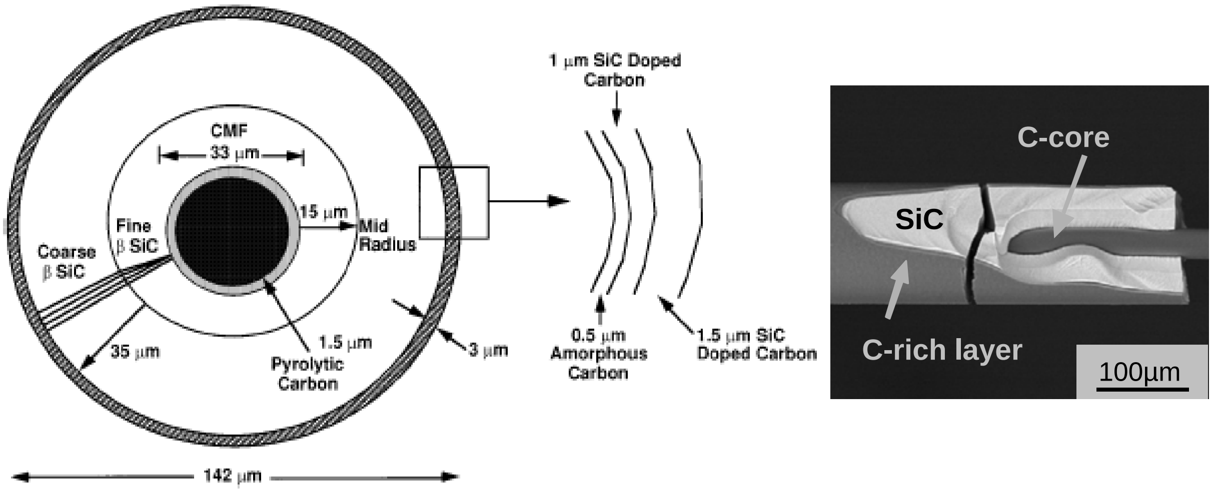

Figure 2.2.a) Schematic of SCS-6 fibre [107]; b) SEM image of SiC – SCS-6 fibre

Having similar strength [108, 109], SiC fibres have the advantage of a better neutron resistance than carbon materials, that swell and loose their conductivity due to structural damage. Investigations into SiC-SiC composites with crystalline fibres have shown that the fibre material behaves in a similar way to that of crystalline SiC bulk material [110]. Bulk SiC under intense neutron irradiation shows only small dimensional changes (volume increase <1%) reached at low doses and progressing no further.

Properties of the SiC fibre at room temperature (RT) are listed in Table 2.1.

Property	**SiC (SCS-6) long fibre**
Young’s modulus (GPa)	380[108]
Poisson’s ratio	0.17[118]
Coefficient of linear thermal expansion (10^{-6} K^{-1})	4.1[108]
Ultimate tensile strength (MPa)	3450[108]

Table 2.1. Properties of the fibre material at RT.

2.1.2. Interface

The interface between matrix and reinforcement plays a crucial role in the determination of the mechanical properties of a composite.

To achieve a good composite interface magnetron sputtering was used to deposit a thin layer of titanium on the silicon carbide fibres.
In a sputter deposition device (Fig. 2.3.), energetic ions (usually argon) from the plasma of a gaseous glow discharge (Fig. 2.4.) bombard a target made of the source material, which acts as the cathode of the discharge. Atoms ejected from the target condense on a substrate producing a coating [111]. Magnetron sputtering is a magnetically assisted discharge where a static magnetic field is created parallel to the surface of the sputtering target by adding a permanent magnet (or electromagnet). The magnetic field concentrates and intensifies the plasma within the space immediately above the target, as a result of trapping electrons near

the surface. The magnetron effect results in enhanced ion bombardment and sputtering rates, for both DC and RF discharges.
Thin titanium and copper layers were deposited using a commercial magnetron sputtering device (Discovery 18DC/RF Research Magnetron Sputter Deposition System), product of Denton Vacuum Company. The machine has a confocal magnetron sputter cathode arrangement able to operate in direct-current (DC) or radio frequency (RF) discharge regimes. The chamber walls act as anode. Power supplies up to 600 W RF and 1000 W DC for sputtering of dielectrics and metals as well as RF etch/bias options are available.

The titanium and copper cathodes (diameter of 7.5 cm) are placed in the top plate of the chamber and are focused on the central area of the substrate table. The distance between cathode and substrate is about 12 cm. The rotation of the substrate table during sputtering enables co-deposition, provides continuous substrate exposure to the cathodes and ensures good coating uniformity. The substrate holder and each cathode are equipped with corresponding shutters that allow an individual etching process before deposition without affecting the cathodes or the substrate. To achieve high vacuum conditions a turbo pump system is installed and connected to the deposition chamber by an automatic gate valve.
An Ar-DC-plasma was used for film deposition in this work.

Figure 2.3. Sputter device image

Figure 2.4. Deposition plasma in sputter device

Processing of the interfacial layer
To optimise the adhesion between fibre and matrix by carbide formation, an interfacial layer of titanium covered with a copper layer for oxidation protection was deposited by magnetron sputtering. Flat substrates of pyrolytic graphite were coated as test samples for TEM analysis. Pyrolytic graphite was chosen because it is similar to the carbon rich coating of the fibre (See chapter 2.1.1.). Before introducing the carbon substrates into the sputtering chamber, they were cleaned in a propanol ultrasonic bath for 5 minutes.

For fibre coating, 8 cm long broken SiC fibre pieces were glued on a cleaned copper frame with a width of 10 cm using conductive silver solution. The fibres where only fixed at one end to prevent fibre deformation due to stresses during deposition. The frame was placed in the sputtering chamber in a stable vertical position (Fig. 2.5.).
Before deposition the chamber was evacuated to a pressure of 10^{-5} Pa. During the experiment 25 sccm argon was injected in the deposition chamber resulting in a gas pressure of around

0.55 Pa. The substrate table was rotated (~6 rpm) assuring a uniform deposition on the plate surface. The deposition parameters are shown in table 2.2.

	RF Probe etching	DC Cathode pre-sputter	DC Ti deposition	DC Cu deposition
Power [W]	200	150	300	300
Time [min]	10	2	5, 10, 20, 30	10, 20, 30

Table 2.2. Parameters of the magnetron sputter deposition

In the first step the samples were cleaned in a plasma etching process with 200 W RF power for 10 minutes.

The deposition of the titanium layer was carried out at an output power of 300 W DC for different periods of time. To protect the titanium layer from oxidation a copper layer was deposited with the same power settings. Before each deposition the cathode was pre-sputtered for 2 minutes with a 150 W DC power setting.

The used deposition parameters were the same for the PyC substrates, the deposition time being varied between 5 and 30 minutes to obtain different coating thicknesses.

After processing the fibres were cut out from the frame. The remaining pieces had a length of about 7 cm.

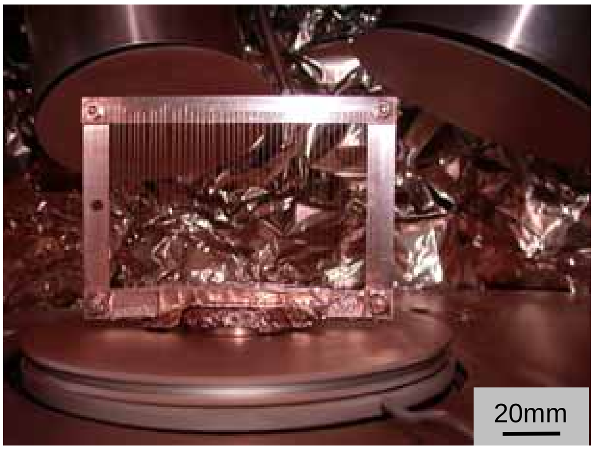

Figure 2.5. SiC fibres on holder in magnetron sputter device

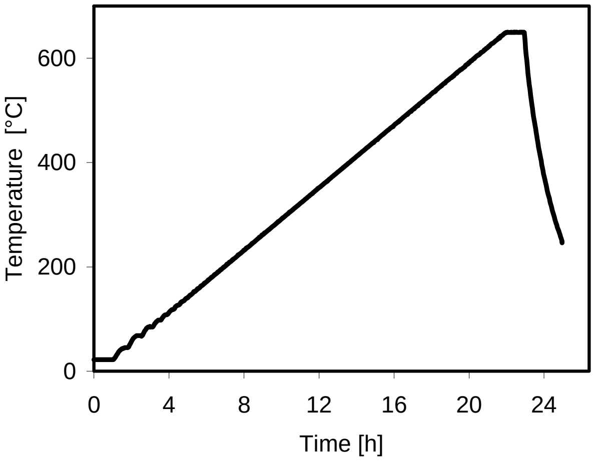

Figure 2.6. Heat parameters for carbide formation investigation

For the first investigation of the carbide formation layered PyC substrates and some SiC fibres were annealed at 650°C for 60 minutes in a vacuum furnace. The applied heating rate was 0.5 K/min (Fig. 2.6.) for comparison and later adaptation to matrix annealing.

The remaining fibres were used for further processing as described in chapter 2.1.3.

2.1.3. Matrix

To combine copper and SiC in a composite, the SiC fibres were electrolytically coated with copper.

Although electrodeposition has been used to produce copper matrix composites reinforced by carbon fibres [112, 113] or silicon carbide whiskers [114], no previous work has been reported on electroplating of SiC fibre with copper.

Actively cooled components in structures designed for elevated temperature service in magnetic confinement fusion reactors require materials with a high thermal conductivity. Copper based alloys are natural choices for such applications. Copper has not only high thermal conductivity but also the advantage of a low elastic modulus, which minimises thermal stresses in actively cooled structures. Copper also offers good machinability, good formability and, in fusion applications, it is attractive for its resistance to neutron displacement damage. It can be expected that irradiation induced slips and defects anneal at the high operation temperature and that the copper still offers ductility. However, for high temperature applications, copper requires a substantial enhancement in strength.

Property	**Cu**
Thermal conductivity W/mK	388$^{120)}$
Young's modulus (GPa)	129.8$^{119)}$
Poisson's ratio	0.34$^{119)}$
Coefficient of linear thermal expansion (10^{-6} K^{-1})	17$^{119)}$
Yield stress (MPa)	54-270$^{119)}$
Ultimate tensile strength (MPa)	224-314$^{119)}$

Table 2.3. Properties of the matrix material at RT

Pure copper is easily obtained by electroplating in an acid solution of $CuSO_4$ as electrolyte, but the plating is accompanied by simultaneous hydrogen and oxygen deposition. While the degree of purity is 99.90% [115] there is always a small amount of other elements co-deposited from the electrolyte. In the literature values of up to 0.04 wt% can be found for oxygen [115]. The oxygen is chemically bonded as Cu_2O.

For hydrogen values up to 300 ppm are reported with atomic hydrogen interstitially placed in the copper lattice. Although both are low concentrations there is the danger of water being formed at temperatures of 400°C [116], with the vapour pressure leading to the formation of pores in the deposited material, known as the "hydrogen disease".

Hence adequate heat treatment of electrolytically deposited copper has to be carried out, allowing the hydrogen to diffuse out. The small amount of remaining oxygen has no significant effect on the conductivity of the material [117].

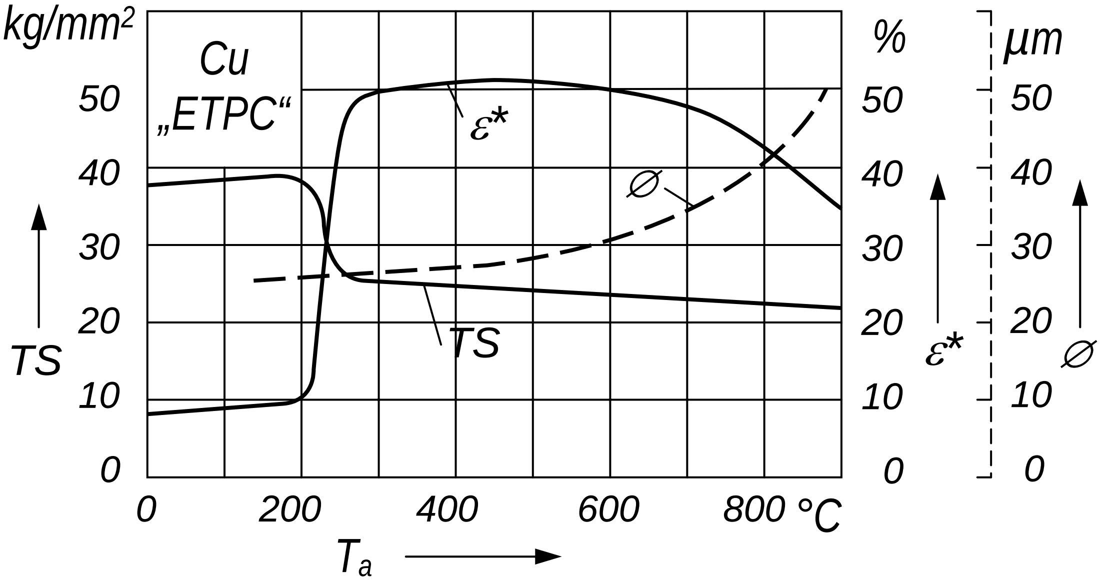

Figure 2.7. Tensile strength *TS*, fracture strain ε^* and grain size $\varnothing$ of electrolytic copper „ETPC“ (electrolytic tough pitch copper) at RT in dependence with the annealing temperature (1/2 hours) [115]

Tensile strength, fracture strain and the grain size of electrolytically deposited copper can also be adjusted by heat treatment as can be seen in Fig. 2.7. Annealing for half an hour at temperatures above the recristallisation temperature of 200°C significantly raises the fracture

strain and the tensile strength is reduced. Fracture strain again decreases with the grains growing.
HIP'ing the final composite at an elevated temperature (650°C, see chapter 2.1.4.) leads to the growth of the as-deposited crystallites.

Electroplating

Electroplating is the process of applying a metallic coating to an article by passing an electric current through an electrolyte in contact with the article. Basically any electrically conductive surface can be electroplated.
The essential components of an electroplating process are an electrode to be plated (cathode), a second electrode to complete the circuit (anode), an electrolyte containing the metal ions to be deposited, and a direct current power source. With no external voltage applied, an equilibrium potential difference forms at the interface between the metal and the solution. Once potential is shifted by an external power source away from the equilibrium potential, a current will be driven across the interface. As a result of the low current through the electrolytic solution metal ions (M^{z+}) recombine with electrons (e^-) to form metal (M) deposited on the cathode.

$$M^{z+} + ze^- \rightarrow M \tag{2.1.}$$

When the potential becomes too high the species reacting at the cathode no longer reach the article's surface at a rate sufficient to sustain the reaction. Undesirable deposit characteristics occur.

Here, the SiC fibres which are to be coated act as the cathode and strips of phosphate containing copper as the anode (phosphate content of 0.04-0.06%) in a sulfuric acid bath. The chemicals used in the plating process were mainly supplied by Schlötter GmbH & Co. KG, as electrolyte the product "Glanzkupferbad ACG-8" was used. Parameters of this electrolytic process are shown in table 2.4.

Copper content	55 – 65	g/l
Free sulfuric acid	50 – 75	g/l
Chloride content	50 – 100	mg/l
Glancing additive ACG-8	3 – 5	ml/l
Working temperature	20 – 30	°C
Cathodic current density	1 – 10	A/dm²

Table 2.4. Electrolytic process parameters

The deposition is dominated by the reaction

$$Cu^{2+} + 2e^- \rightarrow Cu \tag{2.2.}$$

at the fibre surface. At the copper anode an ionisation reaction occurs in the opposite direction that balances the current flow at the cathode replacing the copper ions removed from the solution. The mass deposited can be controlled through variations of plating current and time.
The schematic of the copper plating process and an image of the apparatus used for deposition are shown in Fig. 2.8. and 2.9.

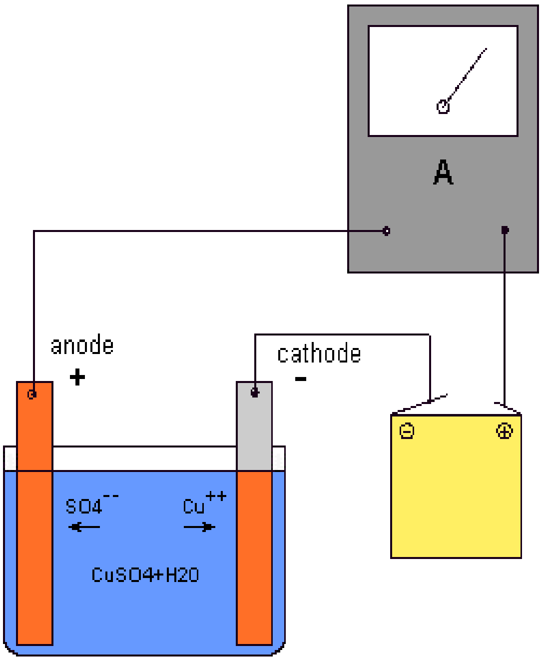

Figure 2.8. Schematic of the electroplating process

Figure 2.9. Image of electrolytic bath

Processing of the matrix material

For matrix processing the SiC fibres were electroplated with copper.

SiC broken fibres of seven centimetres length with and without surface modification (see chapter 2.1.2.) were glued on a copper frame with a width of 50 cm. In contrast to the experiments in 2.1.2. they were glued to the frame at both ends. A conductive silver solution was used as adhesive agent. The frame was introduced into a copper sulphate electrolyte. Copper electrodeposition on SiC fibres was performed starting with a current density of 5 A/dm^2. Due to layer growth on the thin fibres the surface area increases. With the current remaining constant this leads to a reduction of the current density during the deposition process. To find the right voltage to be applied in order to optimise the growth efficiency several coating experiments were carried out. The voltage was raised from 0.4 V to 0.8 V. The coating thickness was adjusted by the deposition time. In figure 2.10. coated-fibres on a frame after the electrolytic deposition are shown.

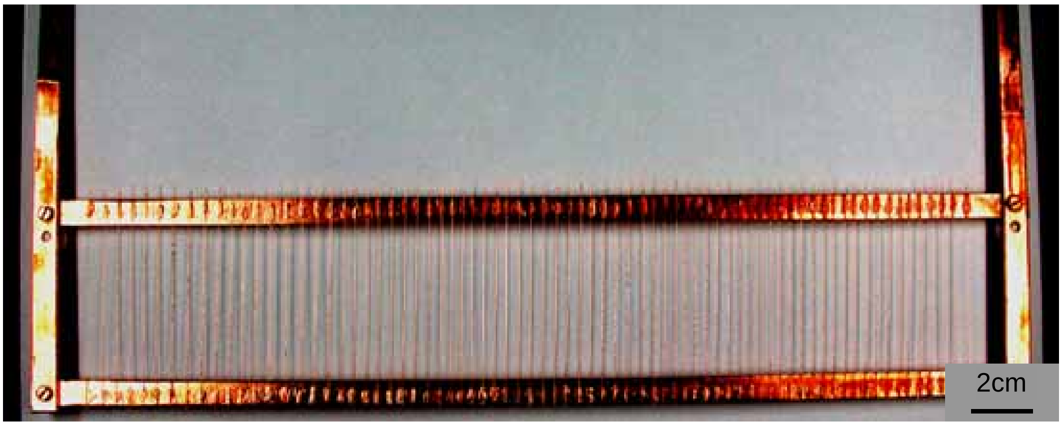

Figure 2.10. Fibres on frame after plating

To determine the temperature where hydrogen diffuses out from the electrolytic copper flat samples with a thickness of 1 mm and the size of 1 cm^2 where heated in a high vacuum device

($p < 10^{-9}$ mbar) where a mass-spectrometer allowed investigation of the residual gases during a heating process. A temperature ramp of 3 K/min was applied.

To investigate the matrix comportment during annealing, coated fibres were heated with two different rates, slow (Treatment 1, table 2.5.) and fast (Treatment 2, table 2.5.), to 300°C and held for one hour. The heating was further continued at the same rate to higher temperatures (550°C, 650°C and 750°C) with a dwell time of 30 minutes. The cooling was done at a rate of 20 K/min.

For the electrolytically coated fibres used in later composites optimised parameters were selected for the heat treatment: a maximum temperature of 550°C was chosen at a rate of 0.33 K/min (Treatment 3, table 2.5.).

		Treatment 1	**Treatment 2**	**Treatment 3**
Step 1	Heating rate [K/min]	0.5	5	0.33
	Dwell temperature [°C]	300		550
	Dwell time [h]	1		2
Step 2	Heating rate [K/min]	0.5	5	-
	Maximum temperature [°C]	550, 650, 750		-
	Dwell time [h]	0.5		-

Table 2.5. Parameters of heat treatment processes

2.1.4. Composite

For consolidation the matrix coated fibres were hot isostatically pressed (HIP'ed). The process was performed in DLR, Cologne, using a C30-03CX press delivered from ABB Asea Brown Boveri, Sweden. The HIP'ing chamber has a diameter of 152 mm and a height of 305 mm. Heating is done by a graphite heater with two heating zones, allowing a maximum temperature of 2000°C and a maximum pressure of 2000 bar. Pressure and temperature are controlled by computer.

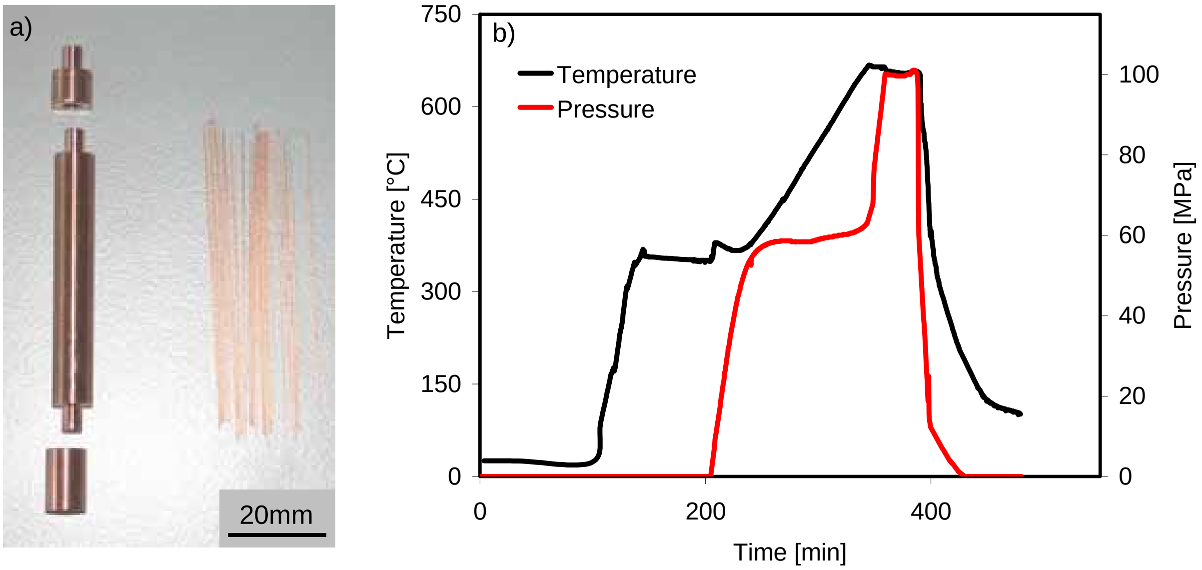

Figure 2.11.a) Coated fibres to be consolidated in the copper capsule; b) HIP parameters

Using coated single fibres processed at different parameters (with and without titanium interlayer, different matrix thickness) composites having different volume fibre fractions (20%, 40% nom.) and different properties at the matrix-fibre interface were produced.

Prior to the HIP'ing the coated and thermally treated fibres were bundled in copper tubes, made of SE-copper (Oxygen-free copper, Cu ≥ 99.90%, P ≈ 0.003%), covered with a copper lid (Fig. 2.11.a) and welded in vacuum. HIP'ing was carried out for 30 minutes at a temperature of 650°C and a pressure of 1000 bar. A dwell time of 1 hour was applied at about 300°C (Fig. 2.11.b). The metal matrix composite is formed by the copper matrix being pressed into the initial cavities between the coated fibres and by diffusion welding. Samples with an outer diameter of 10 mm and a reinforced region of ca. 3.5 mm diameter were produced.

2.1.5. Denotation of probes

The samples used for investigation in this study are summarised in the following tables. The samples names are referred to in the text, allowing to check the individual parameters.

Cu coated single fibres without Ti-interlayer

	electrolytic deposition		**heat treatment**		
Name	**Voltage [V]**	**Time [h]**	**Rate [K/min]**	**Temp.1 /Time [°C]/[min]**	**Temp.2/Time [°C]/[min]**
Test3	0.55	8			
TSSCu03	0.4	8	5	300/60	550, 650, 750/30
	0.4	8	0.5	300/60	550, 650, 750/30
TSSCu07	0.6	8	0.33	550/120	
TSSCu08	0.8	4.5	0.33	550/120	
TSSCu09	0.8	8	0.33	550/120	

Table 2.6. Denotation of copper coated single fibres without Ti-interlayer and the processing parameters

Cu coated single fibres with Ti-interlayer

	sputtering		**Cu-electrolytic**		**heat treatment**	
Name	**Ti [min]**	**Cu [min]**	**Voltage [V]**	**Time [h]**	**Rate [K/min]**	**Temp./Time [°C]/[min]**
CuTi05	10	10	0.8	8	0.33	550/120
CuTi09	5	10	0.8	8	0.33	550/120
CuTi15	10	10	0.8	8	0.33	550/120
CuTi20	5	10	0.8	4.5	0.33	550/120
CuTi26	10	10	0.8	4.5	0.33	550/120

Table 2.7. Denotation of copper coated single fibres with Ti-interlayer and the processing parameters

Composite push-out testing

Name	Fibre type	V_f [%]	Thickness [mm]
TestH3	Test3	10	2.55 2.8 3.55
TSSCuH07	TSSCu07	16	1.35 1.5 2.3 3.0
CuTiH2	CuTi09	15	0.8 1.25
CuTiH4	CuTi15	17	0.45 0.9
CuTiH6	CuTi20	39	not tested
CuTiH8	CuTi26	33	not tested

Table 2.8. Denotation of composite samples used in push-out experiments

Composite tensile testing

Name	Fibre type	V_f [%]
TSSCuH08	TSSCu08	27
TSSCuH09	TSSCu09	15
CuTiH1	CuTi09	14
CuTiH3	CuTi15	14
CuTiH5	CuTi20	32
CuTiH7	CuTi26	27

Table 2.9. Denotation of composite samples used for tensile testing

Fibre tensile testing

Name	V_f [%]
SCS-6	100
TSSCu08	37
TSSCu09	28
CuTi09	18
CuTi15	20
CuTi26	38

Table 2.10. Denotation of fibres used for tensile testing

Electrolytic copper				
	electrolytic deposition		**heat treatment**	
Name	**Voltage [V]**	**Time [h]**	**Rate [K/min]**	**Temp./Time [°C]/[min]**
elCu1f	0.63	48	3	700/
elCu2f	0.63	48	3	(a) 350/ (b) 700/
elCu1	0.63	48		
elCu2	0.63	48		
elCu3	0.63	48	0.33	550/120
elCu4	0.63	48	0.33	550/120

Table 2.11. Denotation of electrolytic copper samples

TEM samples						
	sputtering	**pre-heating**		**Cu-electrolytic**	**heat treatment**	
Name	**Ti, Cu [min]**	**Rate [K/min]**	**Temp./Time [°C]/[min]**	**Voltage/Time [V]/[h]**	**Rate [K/min]**	**Temp./Time [°C]/[min]**
Test3				0.55/8		
PyC	10/10	0.5	650/60			
CuTi05.3	10/10	0.5	650/60			
CuTi05.4	10/10			0.8/8	0.5	650/60

Table 2.12. Denotation of samples used for TEM investigations

2.2. Experimental details

2.2.1. Samples preparation

The preparation of probes for further investigation is difficult due to the difference in the strength of the hard SiC and the soft copper and carbon. Small samples are difficult to hold safely during grinding and polishing operations.

Therefore pieces sheared-off from the single coated fibres were placed within the holes of a cylindrical ceramic ring mounted inside a polymer block which serves as a mould. Further, they were cold embedded in a resin material consisting of two components which are liquid but set solid shortly after mixing. Depending on the kind of planed investigations the probes were cut in thin slices.

Working with composite, representative portions of about a few millimetres thickness were cut from the cylindrical sample using a diamond hacksaw, with the surfaces kept parallel. For easier metallographic preparation the pieces were embedded using the same technique described above. An acetone removable resin was selected for the probes that were later investigated by push-out tests (see chapter 2.2.3.2.).

In the next step wet grinding was done in a Phoenix 4000 grinding/polishing machine from Jean Wirtz/Buehler GMBH using rotating discs covered with diamond coated plastic paper and water. There are a number of grades of flat grinding wheels (120-220-600-1200 granularity) used, while loads of 80-90 N at 300 rotation/min were applied on the sample for 30 seconds. Grinding continues until all the blemishes are removed, the sample surface is flat, and all the scratches are in a single orientation. When moving to the next grinding step the sample was washed in water and blown dry with compressed air.

The next preparation step is polishing. The polishers consisted of rotating discs covered with medium hard cloth impregnated with diamond particles (3 and 1 micron of size) and an oily lubricant. The polishing began with the 3 micron grade and continued with 1 micron polishing particles until the grinding scratches had been removed. The other machine parameters remained the same as for grinding, only the load was reduced to 50 N.

After polishing the probes with 10% watery ferric nitrite solution on synthetic fibre cloth for 10 seconds the copper grains become visible. The use of copper (II) ammonium chloride + NH_3 etchant, attacking the surface, leads to the apparition of the surface relief which allows grain boundaries to be distinguished in light microscopy.

2.2.2. Structure analysis

The probe’s structure was investigated with optical, scanning electron and transmission electron microscopy.

Optical microscope

For optical microscopy investigations the optical microscope Olympus BX60M from Olympus Optical Co., Ltd., Japan was used. It has the ability to magnify in the range of 50X, 100X, 200X, 500X, 1000X. The microscope is featured with a CCD color video camera, model DXC-9100P delivered from Sony Corporation. It allows image capture which can be put out with the help of a computer.

Scanning electron microscope

For scanning electron microscopy the XP30 Environmental Scanning Electron Microscope (ESEM) from Philips/ElectroScan was used.

The ESEM’s features consist of an electron column, that creates a beam of electrons; a sample chamber where the electron beam interacts with the sample; detectors that monitor a variety of signals resulting from the beam-sample interaction - in secondary electron (SE) and backscatter electron (BSE) mode, compositional analyses by energy-dispersive X-ray spectroscopy (EDXS), and collection of electron beam backscatter patterns (EBSP) - and a viewing system, that constructs an image from the signal. Spatial imaging resolution of 2 nm at 20 kV and detection of elements with atomic number Z=6 or larger is possible. An electron gun at the top of the column generates the electron beam.

In the gun, an electrostatic field direct electrons, emitted from a very small region on the surface of an electrode, through a small spot called the crossover. The gun then accelerates the electrons down the column toward the sample with energies typically ranging from a few hundred to tens of thousands of electron volts.

The electrons emerge from the gun as a divergent beam. A series of magnetic lenses and apertures in the column reconverges and focuses the beam into a demagnified image of the crossover. Near the bottom of the column a set of scan coils deflects the beam in a scanning pattern over the sample surface. The final lens focuses the beam into the smallest possible spot on the sample surface. The column requires a high vacuum in order to generate and focus the electron beam.

The beam exits from the column into the sample chamber. The chamber incorporates a stage for manipulating the sample, a door for inserting and removing the sample, and access ports for mounting various signal detectors and other accessories. The sample chamber requires a high vacuum to permit the use of available secondary electron detectors.

As the beam electrons penetrate the sample, they give up energy, which is emitted from the sample in a variety of ways. Each emission mode is potentially a signal from which to create an image.

Image signals are not generated only at the sample surface. The beam electrons penetrate some distance into the sample and can interact one or more times anywhere along their paths. The region within the sample from which signals originate and subsequently escape to be detected is called the volume of interaction.

Sample atom electrons that have been ejected by interactions with the primary electrons of the beam are called secondary electrons. Generally, they have very low energy (by convention less than fifty electron volts). Because of their low energy they can escape only from a very shallow region at the sample surface. As a result they offer the best imaging resolution. Contrast in a secondary electron image comes primarily from sample topography. More of the volume of interaction is close to the sample surface, and therefore more secondary electrons can escape, for a point at the top of a peak than for a point at the bottom of a valley. Peaks are bright. Valleys are dark. This makes the interpretation of secondary images very intuitive. They look just like the corresponding visual image would look.

Primarily beam electrons that have been scattered back out of the sample by elastic collisions with the nuclei of sample atoms are called backscattered electrons. They have high energy, ranging (by convention) from fifty electron volts up to the accelerating voltage of the beam. Their higher energy results in a larger specific volume of interaction and degrades the resolution of backscattered electron images. Contrast in backscatered images comes primarily from point to point differences in the average atomic number of the sample. High atomic number nuclei backscatter more electrons and create bright areas in the image. Backscattered images are not easy to interpret but, properly interpreted, can provide important information about sample composition.

When an energetic electron, usually from the beam, scatters an inner shell electron from a sample atom X-rays result. When a higher energy, outer shell electron of the same atom, fills the vacancy, it releases energy as an X-ray photon. Because the energy differences between shells are well defined and specific to each element, the energy of the X-ray is characteristic of the emitting atom. An X-ray spectrometer collects the characteristic X-rays. The spectrometer counts and sorts the X-rays, usually on the basis of energy (Energy Dispersive Spectrometry, EDS). The resulting spectrum plots number of X-rays, on the vertical axis, versus energy, on the horizontal axis. Peaks on the spectrum correspond to elements present in the sample. The energy level of the peak indicates which element. The number of counts in the peak indicates something about the element’s concentration.

Transmission electron microscope

The investigation of the micro and nano-structures was performed at Max-Planck Institute of Microstructure Physics in Halle by Prof. Dr. J. Woltersdorf and Dr. E. Pippel in the frame of a collaboration with the IPP material research division. The investigations were performed by analytical transmission electron microscopy (TEM) carried out in a PHILIPS CM20 FEG (field emission gun) microscope operating at 200 kV. Both the geometric structure (morphology) and the atomistic arrangements were investigated by high voltage electron microscopy (HVEM) and high resolution/scanning transmission electron microscopy (HREM/STEM). The electron microscope is equipped with an imaging electron energy filter (GIF) from GATAN company. For the determination of the chemical composition within nanometer ranges the energy dispersive X-ray spectroscopic (EDXS) examinations were done by means of a Voyager II system (Tracor Inc.) attached to the PHILIPS microscope.

The working principle of a transmission electron microscope (TEM) is the same as of the scanning electron microscope. A stream of electrons is formed (by the Electron Source) and accelerated toward the specimen using a positive electrical potential. This stream is confined and focused using metal apertures and magnetic lenses into a thin, focused, monochromatic beam. This beam is focused onto the very thin sample (< 200 nm) using a magnetic lens. Unlike the scanning electron microscope, which uses reflected electrons, the TEM uses electrons passing through a very thin slice of the specimen. These highly energetic incident electrons interact with the atoms in the sample producing characteristic radiation and particles providing information for materials characterisation. The transmitted portion of the electron beam is focused by the objective lens into an highly-magnified image onto a phosphor screen or special photographic film revealing information of the internal structure of specimens. The darker areas of the image represent those areas of the sample that fewer electrons were transmitted through. The lighter areas of the image represent those areas of the sample that more electrons were transmitted through. TEM imaging allows for magnifications up to 1,000,000 times, and very high-resolution imaging, with point to point resolution of better than 2 nm. Sample preparation for TEM analysis is critical.

2.2.3. NanoTest platform

For hardness and push-out measurements a nanoindenter, NanoTest 600 from Micro Materials Ltd., UK was used. This is an indentation instrument capable to measure the displacement of a stylus probe into a surface as a function of the increasing applied load. Force, displacement and time are recorded throughout the test. The displacement resolution is < 1 nm. The positioning accuracy is < 2 µm.

The Micro Materials NanoTest platform has been designed to support separate modules which allows to install different setups for specific needs. The *indentation module* for nanoindentation, nano-, micro-hardness testing and reduced modulus determination can be used in conjunction with a low load “Nano” head (0.1-500 mN) or a high load “Micro” head (0.1-20 N). For the low load head (NT), there are two load ranges available: NT 1 and NT 2. NT 1, the lower range, allows highest sensitivity for loading the coil, with the maximum load typically 45 mN. The load range is selected via a switch at the front of the control panel. The load resolution is 0.1 µN for nano head and 60 µN for micro head (MT). The NanoTest system is supplied with a high-resolution microscope that enables the exact positions of indentation sites to be defined with the surface of the sample in view on the microscope monitor. The sample is installed on a holder in a vertical position parallely faced to the microscope and the impressing stylus. The position calibration of two planes (the focal plane and the measurement plane) has to be completed before the machine can be used.

The *focal plane* is the plane parallel to the Y-Z plane of the sample holder in which the surface of the sample is in focus “under” the highest magnification lens.

The *measurement plane* is the plane parallel to the Y-Z plane of the sample holder in which the surface of the sample is normally 50 µm away from the tip of the indenter.

The instrument is constructed so that when the sample is in the focal plane operation of the large transfer stage will not cause the sample to collide with the indenter. Thus, the software will always ensure that the sample stage is left in the focal plane position and therefore enable the operator to move the sample using the large transfer stage from “under” the microscope to the pendulum position in front of the indenter.

Figure 2.12.a) shows a schematic illustration of the NanoTest equipment [121]. The device utilises a pendulum rotating on a friction-less pivot. A coil is mounted on the top of the pendulum; with a coil current present, the coil is attracted towards a permanent magnet, producing motion of the diamond towards the sample and into the sample surface.

The displacement of the diamond is measured by means of a parallel plate capacitor, one plate of which is attached to the diamond holder. When the diamond moves, the capacitance changes, and this is measured by means of a capacitance bridge. The capacitance bridge unit is located close to the measuring capacitor in order to minimise stray capacitance effects.

Sample manipulation is done by means of three DC motors driving micrometer stages in an XYZ configuration. The motor control electronics consists of a mother board containing three power modules, an IEEE interface module and a backlash control board. These plug into expansion slots in the computer.

The limit stop defines the maximum outward movement of the diamond, and also the operating orientation of the pendulum, when a load is applied. Its position is manually adjusted by a micrometer. The equilibrium position of the pendulum, with zero load current, is adjusted with balance weights, which are movable along both the horizontal and vertical axes.

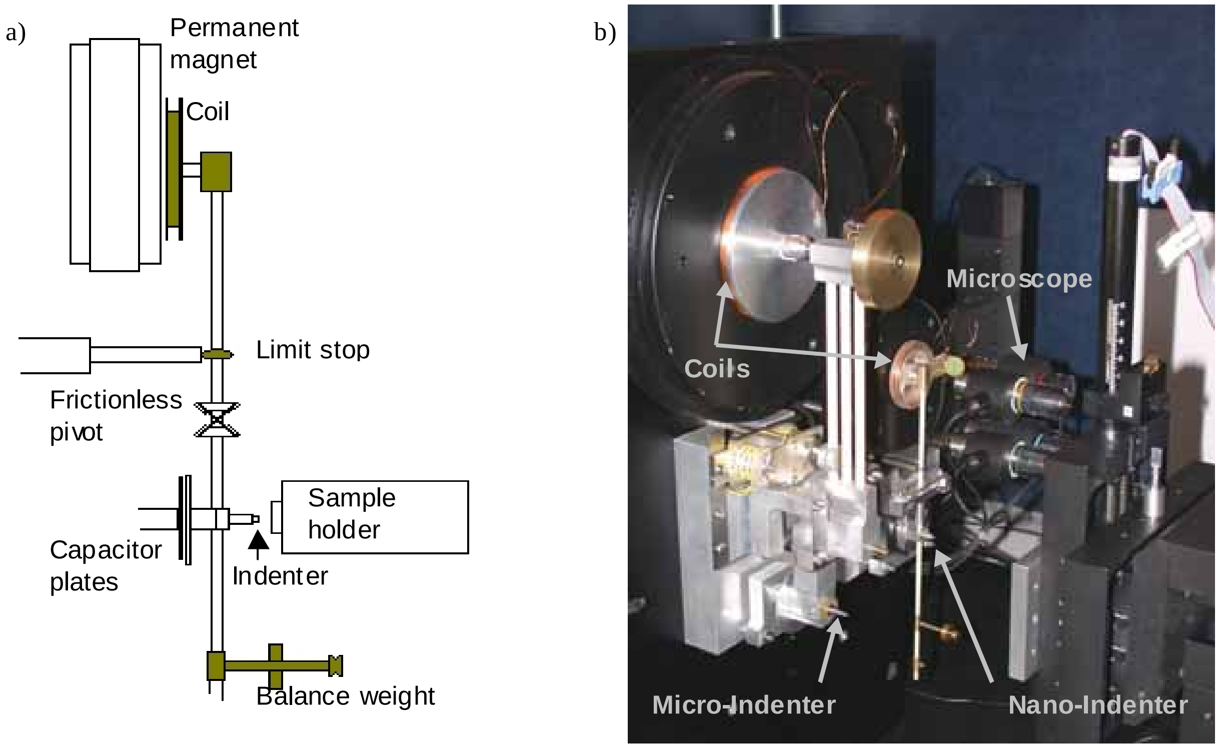

Figure 2.12.a) Schematic drawing of NanoTest setup; b) Photograph of the NanoTest device („Micro“ and „Nano“ heads)

Some maintenance checks (bridge box adjustment and zero load calibration) should be performed on a daily basis to confirm that the instrument is working at its optimum level.

The NanoTest uses a capacitive bridge circuit for displacement measurement. It is important to balance the bridge accurately to ensure maximum sensitivity to small displacements. The pendulum test is an indicator that the electronics are all plugged in properly and functioning correctly, and secondly, it shows whether the pendulum is mobile or not. The bridge unit contains a 5 kHz sine wave generator. The 5 kHz signal is applied across a 4-element AC bridge. Three elements of the circuit are adjustable by means of the three bridge unit controls. The fourth element in the circuit is the NanoTest capacitor. By tuning the bridge components so that the bridge is close to its balance condition, it is possible to look at the very smallest change in signal due to a change in the capacitance of the NanoTest capacitor. This will correspond to very small changes in depth when the machine is being used. The signal that comes from the moving plates goes into the unit through a short, gold coaxial lead. This contributes a large part of the capacitance being ‘tuned’ by the other bridge components and it is very important that it is firmly connected to obtain the best results.

The zero load calibration determines a minimum coil voltage necessary to hold the pendulum onto the limit-stop. The process is essentially the same as the pendulum test (bridge box adjustment) but while the force is being applied to the coil, it is measured to extract the value required to just bring the pendulum into contact with the limit stop. This calibration benefits from the pendulum test characteristic being as close to ideal as possible.

As the calibration is very exacting (in the order a few µN), it needs to be done often. External factors such as temperature stability of the cabinet and of the electronics can cause the value to alter. In general 3 calibrations have to be carried out before measurements. The calibration does not make contact with the sample surface and so does not need a specific sample to be in the machine.

It is also necessary to do periodic calibrations (load, depth, machine compliance, diamond area function).

The load calibration establishes the forces that can be applied at the diamond tip during a measurement. Calibration consists of hanging a series of masses from a set point (the balance point) at the bottom of the pendulum while the coil applies a countering force equating to a known voltage for each mass. The anticlockwise moment due to the coil current is balanced by the clockwise moment due to the applied weight [121]. The weight range normally used is 0-10 g. It is necessary to calibrate for each load range (NT1, NT2 and MT) being used (MT requires the set of three heavier balance weights). This calibration relies on a good pendulum test in *bridge box* adjustment.

The depth calibration relates the change in capacitance to a known distance moved by a sample in contact with the pendulum. The sample movement is determined directly from the stage movement (encoder displacement).

The calibration routine involves moving the sample in until the signal coming from the measuring plates is 1/4 of the initial value. At this point, the motor movement reverses and between 1/3 and 2/3 of the maximum signal amplitude, the changing amplitude is monitored against the known distance moved by the fused silica sample. The sample stops at 10 points for collection of bridge output data versus sample position data.

Another important calibration is the determination of the machine (or frame) compliance required for the determination of elastic properties of materials; any elastic deformation of the instrument at a particular load must be subtracted from the apparent diamond displacement at that load. From the measured data the contact compliance can be determined and then the sample compliance is obtained from *contact compliance (C) = sample compliance* (C_s) + *machine compliance* (C_f). When the sample compliance is small (high modulus sample) the machine compliance makes up an appreciable fraction of the total measured deformation and so small errors in the machine compliance can affect the accuracy of the sample modulus determination. Automatic compliance determination is based on elastic recovery data obtained from a well-documented reference material. Fused quartz is the preferred material and the NanoTest software will assume that this is being used. A Berkovich indenter, a three-sided pyramid with an area-to-depth function, which is the same as that of a Vickers indenter, was used in experiments. 10 *depth* versus *load* hysteresis curves are produced with a maximum load of 200 mN. The total compliance is measured from the unloading curve using the method of *Oliver and Pharr* (Chapter 2.2.3.1.) [122]. The sample compliance is given by $C_s=\pi^{0.5}/2E_rA^{0.5}$, where A is the projected area of contact at maximum load and E_r is the reduced modulus given by

$$\frac{1}{E_r}=\frac{1-\nu^2}{E}+\frac{1-\nu_i^2}{E_i} \tag{2.3.}$$

where E and ν are the elastic modulus and Poisson's ratio for the specimen (for quartz they are E=72 GPa and ν=0.17) and E_i and ν_i are the same parameters for the indenter (for diamond they are E_i =1141 GPa and ν_i=0.07, respectively).
Using the ideal diamond area function for a Berkovitch indenter $A=24.5h_c^2$ and h_c (the vertical distance along which contact is made - called the contact depth) obtained from *Oliver and Pharr* analysis of the raw data, an initial estimate of the frame compliance is obtained from $C_f=C-12725.8/A^{0.5}$ [121]. The constant *12725.8* follows from assuming the literature value for the elastic modulus of fused quartz. The first estimate of C_f is used to correct the raw data and produce a new value of h_c, again using the *Oliver and Pharr* method. The procedure is repeated several times until convergence is achieved.

The Diamond Area Calibration relates the actual, non-ideal diamond contact area to the depth of penetration. This involves performing a series of indentation experiments on a fused silica (quartz) sample. The target aim of the Diamond Area Calibration (*DAF*) is to find the function which can be used across a wide indentation range (0.5-200 mN) to obtain accurate hardness and modulus values which allow for the changing indenter shape. The calibration determines the constants k_1 and k_2 in the function $A = k_1h_c^2 + k_2h_c$, where A is the contact area and h_c is the contact depth. For an ideal Berkovitch indenter k_1 = 24.5 and k_2 = 0 nm. For a real Berkovitch indenter, values of k_1 = 20-24 and k_2 = 1500-3000 are typical, although since each diamond is slightly different, these values are only a guideline. This data is automatically analysed using the *Oliver and Pharr* method [122] to produce the required depth values. The method is based on the assumption that the elastic modulus is independent of indentation depth.

The operation of the MT loading head is very similar in principle to the low load head (NT) and the pendulum has to be calibrated for load and depth like the NanoTest. Similarly, a compliance calibration is necessary – although not with fused silica, as the large forces required will 'crack' the surface. For this calibration a steel sample is provided and indentation are carried out over 1-20 N load range. The *DAF* is not required, as at the indentation depth produced at these higher forces the tip correction is insignificant and for all practical measurements the ideal function will be satisfactory.

2.2.3.1. Hardness and elastic modulus determination

The two mechanical properties measured most frequently using load and depth sensing indentation techniques are the elastic modulus, E, and the hardness, H.

In a pyramidal indentation, the NanoTest measures the penetration depth of the calibrated diamond indenter as a function of the applied load during a load-unload cycle. A typical indentation loading curve is shown schematically in Fig. 2.13.a), where the load on the indenter is plotted versus the depth of indentation. On unloading the elastic component of the displacement starts to recover producing a sloped unloading curve. From the slope the elastic and plastic properties can be derived.

The NanoTest data analysis software produces values of h (h_{max}, total displacement) and h_c (contact depth) (Fig. 2.13.b)) together with the derived hardness and reduced modulus.
To determine the mechanical properties of the samples in Pyramidal Analysis, the depth vs. load unloading data can be fitted to either a linear fit - a tangent to the unloading curve at the maximum load – (Doerner and Nix fit) [123, 124] or to a power law fit - (Oliver and Pharr fit) [122]. The Oliver and Pharr method is preferred and is briefly described below.

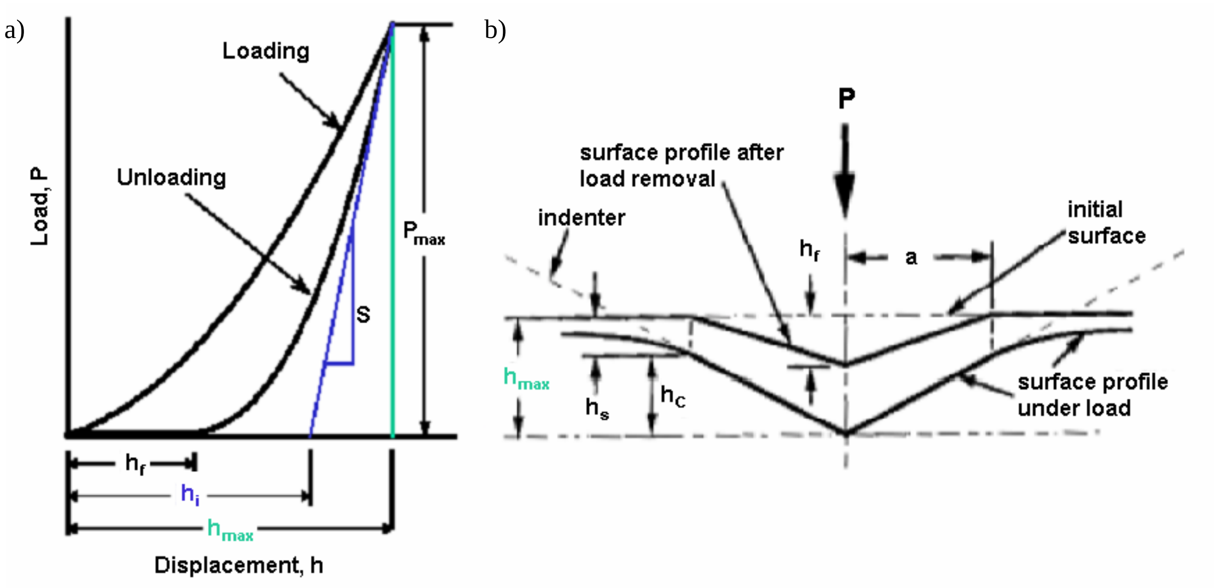

Figure 2.13. A schematic representation of: a) load versus indenter displacement data for an indentation experiment, b) a section through an indentation showing the quantities used in the analysis [122].

Power-law fitting: Oliver and Pharr method

The analysis of indentation load-penetration curves produced by depth-sensing indentation systems is often based on work by Oliver and Pharr. In general, the relationships between penetration depth, h, and load, P, for different indenter geometries is the power law function, which has the form

$$P = \alpha (h - h_f)^m \tag{2.4.}$$

where α contains geometric constants, the sample elastic modulus and Poisson's ratio, and the indenter elastic modulus and Poisson's ratio, h_f is the final unloading depth, and m is a power law exponent that is related to the geometry of the indenter. The constants α, h_f and m are determined by a least squares fitting procedure.

Figure 2.13.b) shows a cross section of an indentation and identifies parameters used in the analysis. At any time during loading, the total displacement h is written as $h=h_c+h_s$ where h_c is the vertical distance along which contact is made and h_s is the displacement of the surface at the perimeter of the contact. At peak load, the load and displacement are P_{max} and h_{max}, respectively. Upon unloading, the elastic displacements are recovered, and when the indenter is fully withdrawn, the final depth of the residual hardness impression is h_f. The experimental parameters needed to determine hardness and modulus are shown in Fig. 2.13 a). The three key parameters are the peak load (P_{max}), the depth at peak load (h_{max}), and the initial unloading contact stiffness (S_{max}).

The stiffness, S, is the slope of the tangent line to the unloading curve at the maximum loading point (h_{max}, P_{max}) and is given by

$$S = \left(\frac{dP}{dh} \right)_{(h_{\max}, P_{\max})} = \alpha\, m \left(h_{\max} - h_f \right)^{m-1} \tag{2.5.}$$

where the parenthetic subscript denotes that the derivative is evaluated at the maximum loading point.

The reduced modulus is related to the contact area and the measured stiffness by

$$E_r = \frac{\sqrt{\pi}}{2}\frac{S}{\sqrt{A}} \quad . \tag{2.6.}$$

Measurement of the unloading slope can thus be used to determine the reduced modulus if the contact area at peak load can be measured independently.

The area of contact at peak load is determined by the geometry of the indenter and the depth of contact, h_c. The indenter geometry can be described by an area function $A(h)$ which relates the cross-sectional area of the indenter to the distance from its tip, h. Given that the indenter does not itself deform significantly, the projected contact area at peak load can then be computed from the relation $A= A(h_c)$. The diamond area function $A(h_c)$ must be established experimentally prior to analysis.

To determine the contact depth from the experimental data, it is noted that

$$h_c = h_{max} - h_s \tag{2.7.}$$

and

$$h_s = \varepsilon P_{\max} / S \, . \tag{2.8.}$$

The value of ε depends on the indenter geometry. For a Berkovich indenter ε is 0.75.

The hardness (H) is determined from the peak load (P_{max}) and the projected area of contact, A:

$$H = P_{max}/A. \tag{2.9.}$$

2.2.3.2. Push-out test

The composite push-out samples were glued to a round aluminium holder with a polymer glue which can be easily removed with isopropanol after the experiment. To provide space for the pushed-fibre the holder has a groove that is 700 µm deep and 1.4 mm wide along its diameter. The sample is placed on the holder in such a way that the fibres to be pushed are placed above the groove (Fig 2.14.).

Figure 2.14. Push-out sample holder

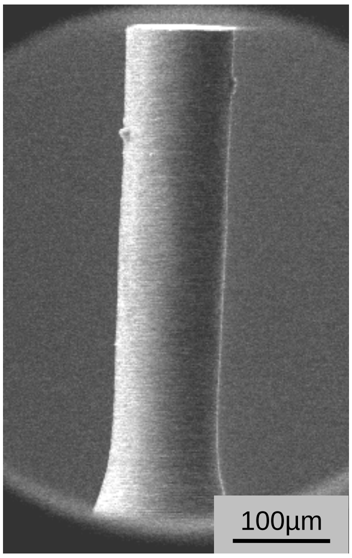

Figure 2.15. Push-out tip

A cylindrical tungsten carbide punch (diameter of 100 µm, length of 400 µm) was used as push-out indenter (Fig. 2.15.).

Push-out tests using the MicroTest head of the nanoindenter machine were performed on samples cut from Cu-SiC composites. Only *load-controlled* experiments could be performed, where the linear increasing load applied to the top of the sample and the corresponding punch penetration depth are measured. During the push-out test the punch is driven to contact the sample and then the load increases until the complete fibre debonds. While the resulting load decreases after debonding, the machine is only able to raise the applied force and accelerate the fibre until a maximum displacement is reached.

As a consequence, the experimental points corresponding to the frictional sliding of the fibre are missing in the load-displacement diagram (Fig. 1.19. (f)).

Nevertheless, the load at which debonding starts (P_d) and the maximum load before complete debonding (P_{max}) can be estimated. This enables one to derive the interfacial parameters τ_d and τ_f using the previous equations 1.26. and 1.30.

2.2.4. Universal-material-test platform

In this work the alternative capabilities of a universal-material-strength-test device TIRAtest2820, delivered by TIRA GmbH, were implemented.

The machine is suitable for the study of the strength and deformation behaviour of materials under tension, compression and bending loads. The experiments are possible at ambient temperature and test procedures are partially automated and computer-aided.

The device is equipped with loading features, a measure and control unit as well as peripheral facilities for the loading mechanisms and data output. It possesses a high rigidity and an exact traverse guidance.

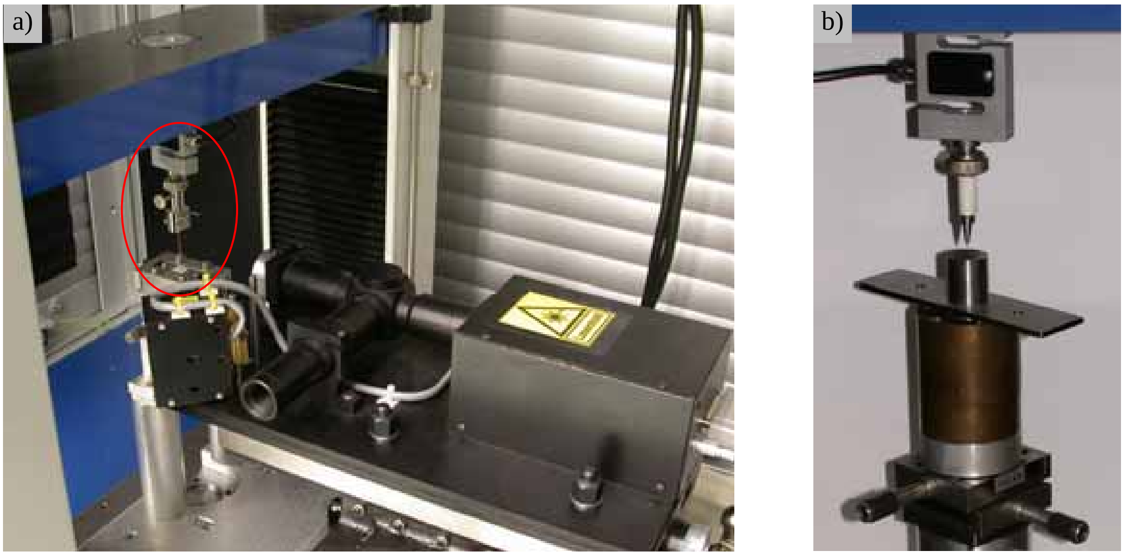

Figure 2.16. Image of the universal-test-machine; a) designed for tensile tests; b) adapted for push-out tests

The working principle is applying either a dynamic load and measuring the induced displacement, or applying a displacement and measuring the resulting load. The load is applied by traverse movement and quantified by a load cell connected to the computer interface. A maximum testing load of 20 kN can be applied depending on the cell. The 200 N load cell supplies a digital resolution of 2 mN, whereas for the 20 kN cell the resolution is about 0.5 N.

The change in length due to the load applied is measured using a Laser-Speckle Extensometer LSE-4000 DE which uses coherent illumination of the probe surface to generate the somewhat granular pattern always experienced with coherent wave phenomena. Although this pattern appears to be random it still yields enough spatial information about the object's surface to be able to accurately track displacements with the help of a conveniently positioned camera. The signal is processed in the digital signal processing unit is based on an image cross-correlation type pattern matching followed by a standard interpolation scheme. It resolves displacements smaller than the pixel pitch of the camera (7 µm) and a resolution of about 0.1 µm is achieved.

In this testing device tensile and push-out tests were performed (Fig. 2.16.).

2.2.4.1. Tensile test

The mechanical and failure behaviour of materials under the applied load may be tested in stress-strain experiments. The tests are distinguished by the way the load is applied: tension (further called tensile test), compression and shear.

A tensile test is also useful to investigate the mechanical properties of composite materials.

In a standard tensile test a specimen is deformed, usually to fracture, gradually increasing the tensile load uniaxially to the long dimension of the specimen. Typically, the specimens' cross section is circular, but rectangular specimens can also be used. The ends of the specimen are mounted in the holding grips of the tensile test device (Fig. 16.a)) which is designed to elongate the specimen at a constant rate while it continuously measures the applied load (using a load cell) and the induced elongation (using an extensometer). The load versus elongation characteristics are computed but depend on the size of the specimen. In order to eliminate this geometrical influence, normalised parameters for stress and strain are used, which are defined as follows:

$$\sigma = \frac{F}{A_0} \tag{2.10.}$$

$$\varepsilon = \frac{l_i - l_0}{l_0} = \frac{\Delta l}{l_0}, \tag{2.11.}$$

where F is the instantaneous load applied perpendicular to the cross section, A_0 is the original area of the cross section, l_0 is the length before any load is applied, l_i is the instantaneous length and Δl is the change in length at some specific instant.

The Young's modulus of a test specimen is determined by the gradient in the linear region of the stress-strain-curve.

Different batches of copper coated fibres with and without special interface treatment were compared. Damage to the thin and soft copper coating by clamping the ends of the fibres is prevented by coating them with a thick electrolytic copper layer. In addition, scraps of paper were enclosed in the clamp to avoid sliding.

A low testing speed of 1 µm/s was applied until fracture occurred.

2.2.4.2. Push-out test

For several investigated samples the maximum load available in the nanoindenter (20 N) was not enough to push-out the fibres. The universal test device adapted for push-out experiments (Fig. 16.b)) fulfilled the required loading conditions and therefore was used to investigate these samples.

The sample is placed on the sample holder which has two perpendicular grooves on the surface. The grooves are 0.5 mm wide and 1 mm deep. In this vertical setup it is not necessary to fix the sample to the holder.

As indenter the shank of a perpendicular polished tungsten carbide micro-drill with a diameter of 120 µm was mounted to the load cell. Supplying the required radial stiffness the 20 kN load cell had to be used despite its low digital resolution. Anyhow sufficient accuracy was obtained.

With the help of a 25x magnifying lens the indenter-tip is placed above the centre of a fibre, by simply aligning in two 90 degree viewing directions using an x-y-displacement table.

An increasing load is applied on the fibre by constant 1 µm/s displacement of the punch and the resultant load is measured by the load cell. A load-time curve is displayed during the test. Being *depth-controlled*, in difference to the push-out test in the NanoTest device, the push-out curves also contain the data corresponding to the fibre sliding after complete debonding. The interfacial parameters are calculated in the same way as described for the NanoTest platform.

3. Results

3.1. Morphology and microstructure

3.1.1. Magnetron-sputter deposition

For interface improvement a magnetron sputter process as described in chapter 2.1.2. was used.

3.1.1.1. Deposition rate

The deposition rate of the sputtering process for titanium and copper was determined with flat samples lying on the rotating table. Pieces of Si-wafers partly covered against deposition by other Si-wafer-pieces were used as substrates. The layer thickness was measured using a standard profilometer. The thickness of the Ti-layer was determined as the difference between the total thickness and the thickness of the copper layer, which was deduced from the deposition duration. The deposition rate of copper had been determined in a separate experiment. The titanium layer was always coated with copper as oxidation protection.
Coating time and results are shown in table 3.1.
A deposition rate of 31 nm/min for copper and 17.5 nm/min for titanium was found (Fig. 3.1.).
In figure 3.2. an example micrograph of the deposited layers on pyrolytic graphite is shown.

Time [min]	**Thickness [nm]**		
	Cu	Ti+Cu	Ti
10	290	460	170
20	660	1050	390
30	900	1400	500

Table 3.1. Thickness of titanium and copper deposited layers for different deposition time

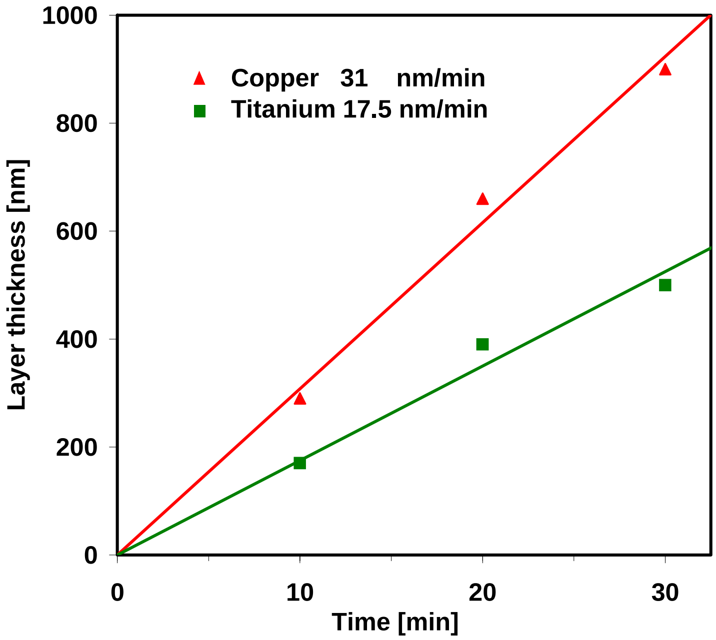

Figure 3.1. Determined sputter deposition rates for titanium and copper

3.1.1.2. Fibre sputter-coating

Using SEM capabilities the dependence of the titanium layer thickness on the position in the deposition frame was determined. Figure 3.3. is an example SEM micrograph showing the sputtered titanium and copper layer after 30 minutes deposition and the electroplated copper layer.

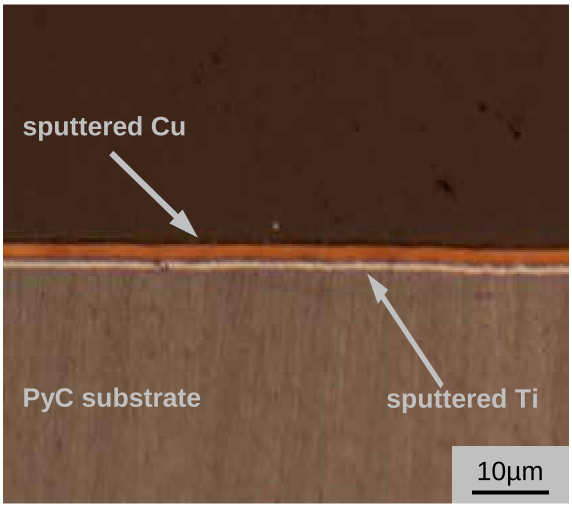

Figure 3.2. Example of optical micrograph of the Ti and Cu layers on PyC substrate

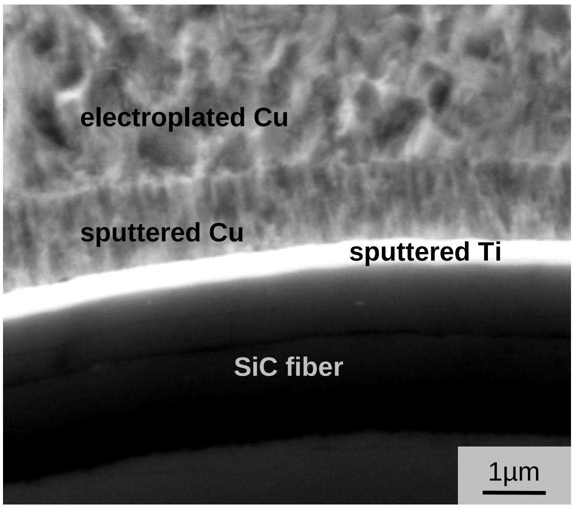

Figure 3.3. Example of SEM micrograph of the Ti and Cu layers on SiC fibre

With the deposition frame placed vertically in the sputtering chamber (Fig. 2.5.) SCS-6 fibres fixed on the frame were sputter-coated with titanium for 10 minutes and afterwards covered with the oxidation protection copper layer.
Two representative fibres from both, edge and middle of the frame were taken for analysis.

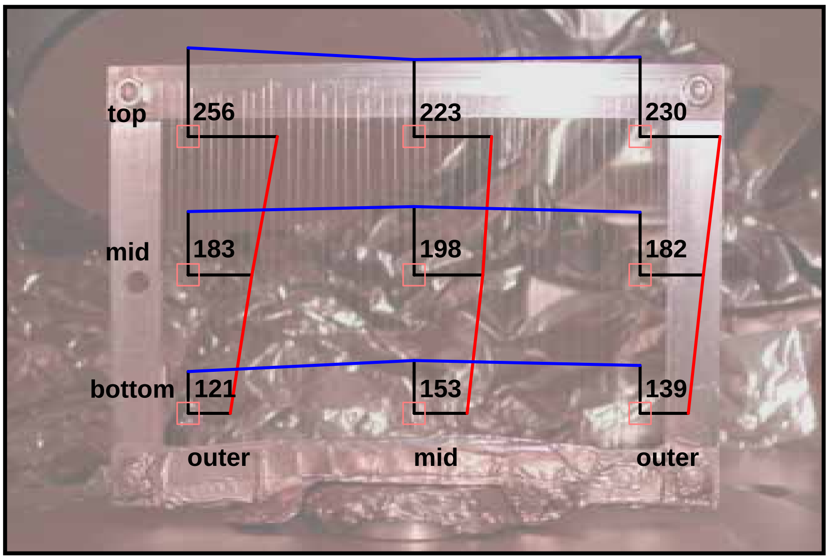

Figure 3.4. Schematic of the distribution of the titanium thickness (numbers in nm) along the fibre length in different points on the deposition frame

Each fibre was divided into three parts representing fibre top, bottom and middle. All of these parts were further prepared as described in chapter 2.2.1. For each position SEM images were captured in different regions over the fibre's circumference. For every image the thickness was measured in different locations. An average value was then determined for each of the different positions on the fibre and of the respective fibre within the frame.

The distribution of the titanium layer thickness along the fibre (red line) and over the deposition frame (blue line) is demonstrated in Fig. 3.4., where the length of the indicative black lines is proportional to the average values calculated for the thickness (shown twice for horizontal and vertical comparison). The background image shows the frame with fibres inside the deposition chamber (see Fig. 2.5.). The red squares roughly indicate the measurement position.

3.1.2. Electrolytic deposition

The microstructure of the electrolytically deposited copper layers of individual coated fibres before and after heat treatment was investigated by optical and electron microscopy. The composite was also investigated by optical microscopy and SEM studies.
For fibre coating with copper matrix material different deposition parameters were applied during the electrolytic process. The fibres without modified interface were first deposited applying voltages between 0.4 V and 0.6 V. After parameter optimisation 0.8 V were chosen. All fibres with modified surface were electrolytically processed at 0.8 V.

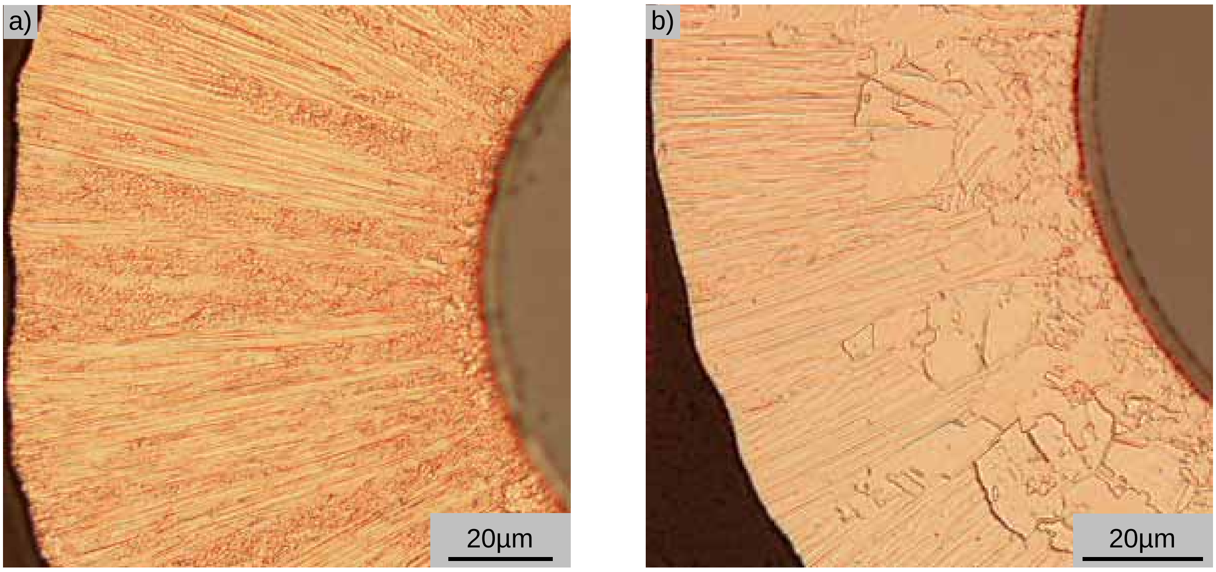

Figure 3.5. As-processed electrolytic copper microstructure a) needled; b) interrupted by larger grains

The optical-microscopy investigations show that in the as-deposited specimens a homogeneous microcrystalline structure is formed (Fig. 3.5.a)). The electrolytic copper layer growth starts with small crystallites on the fibre surface and afterwards turns over into radial columnar growth. Sometimes locally bigger rounder grains were observed (Fig. 3.5.b)).

In Fig. 3.6. micrographs of the copper coated fibres after respective deposition times of 4.5 hours and 8 hours are shown. The deposition of the copper layer during the electrolytic process took place not uniformly along the fibre length. The copper coating thickness between the two fibre ends was found to vary for the short deposition time in a range of 40-75 µm while for 8 hours deposition it varies in a range of 60-120 µm.

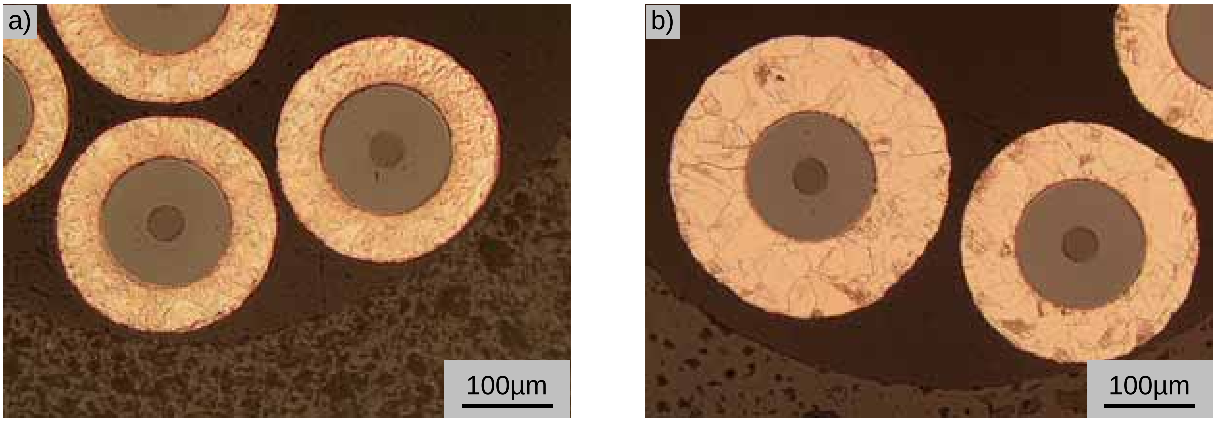

Figure 3.6. Optical micrographs showing the electrolytic copper layer (annealed) a) after 4.5 hours; b) after 8 hours deposition time

3.1.3. Heat treatment

3.1.3.1. Crystallite structure

An essential change of the structure occurs after annealing of the coated fibres at 550°C. With the heat treatment a growth of the grains occurs (Fig. 3.7.). A uniform structure is formed, the grains were found to be still smaller in the near fibre region where the small crystallites on the as-deposited fibres were observed.

Figure 3.7. Grain size after heat treatment at 550°C (0.33 K/min)

3.1.3.2. Reduction of porosity

Hydrogen desorption from the electrolytic copper was investigated with a mass-spectrometer installed in a high vacuum chamber. Two flat samples of as-deposited electrolytic copper (10x10x1mm) were heated with 3 K/min to 700°C on a molybdenum heater, while for sample #2, in order to observe surface cleaning effects, the heating was interrupted at 350°C (#2a) and continued after cooling down to 150°C (#2b). To obtain a background spectrum of the device the same run was carried out without a sample. The resulting temperature dependent desorption curves of hydrogen (H_2) are shown in figure 3.8.

The background signal increases with increasing temperature due to chamber characteristics. The beginning of hydrogen release is observed around 250°C (red circle) with a significant increase of the hydrogen signal. Small peaks (red arrows) are found as well as a shift in temperature between the measurements as discussed in chapter 4.1.

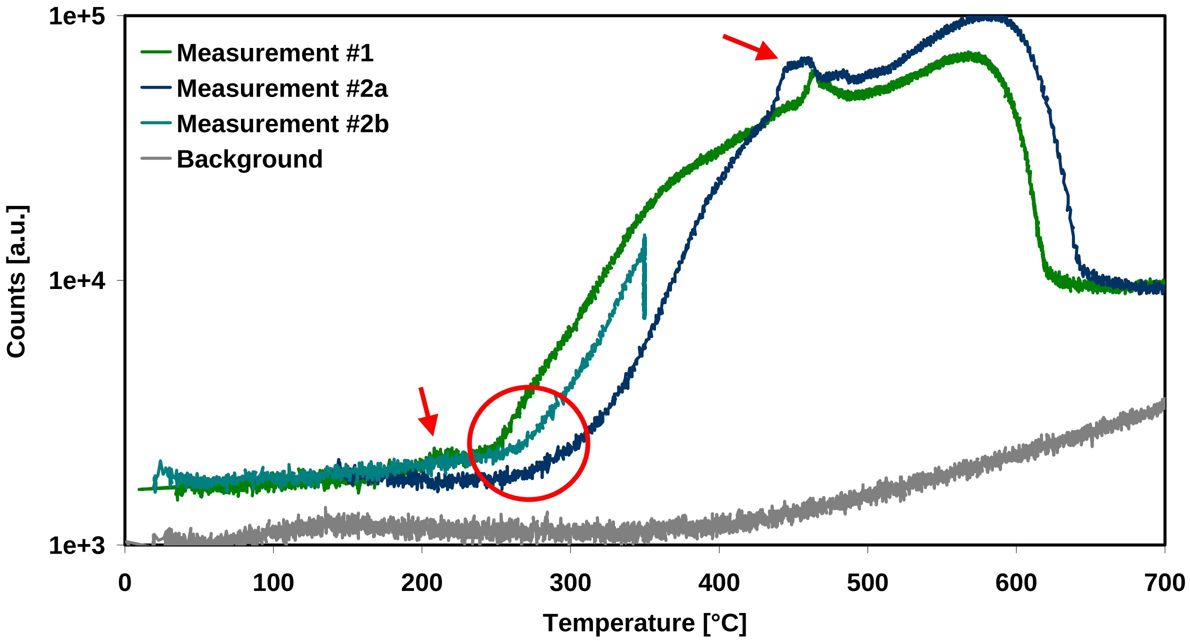

Figure 3.8. Hydrogen molecule signal of a quadrupole mass spectrometer during heating of electrolytic copper in ultra high vacuum

The temperature simulation of the HIP process was done by heating the copper coated fibres to 550°C, 650°C and 750°C with two different slopes (5K/min, 0.5K/min) and a dwell time of 60 minutes at 300°C. After the fast treatment many pores, mostly located at the grain boundaries, were found by optical microscopy. With the slow treatment two times less pores are visible.

This pore formation was found independent of the annealing temperature. The different pore-content is visible in Fig. 3.9. for an annealing process to 650°C (Table 2.5., treatment 1 and 2).

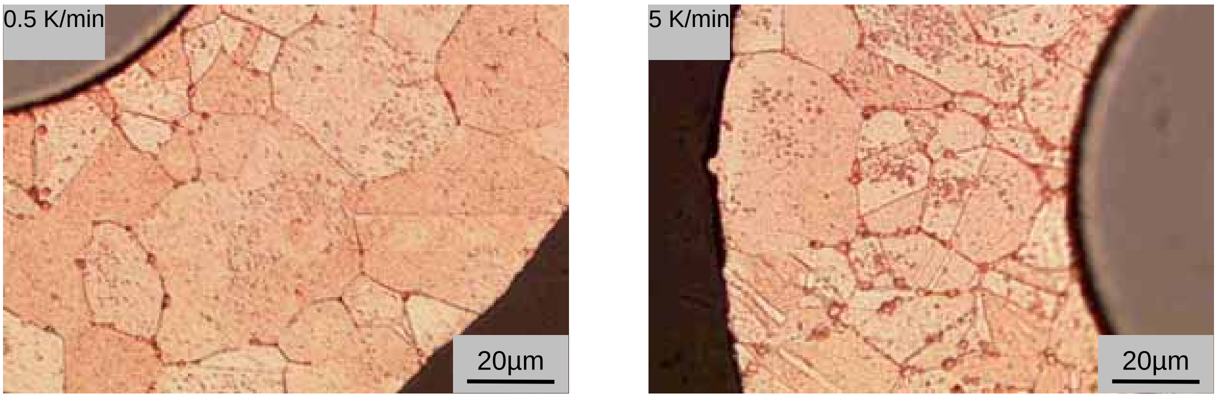

Figure 3.9. Different copper porosity at different heating rates (650°C)

3.1.4. Hot isostatic pressing

Representative overviews of the composites with different fibre volume fractions (16% and 10%) after the HIP'ing process can be seen in Fig. 3.10. Figure 3.11.a) shows the first processed test-composite TestH3 obtained without pre-heating the copper coated fibres. Many pores are observable at the edges of the copper coating (see chapter 4.1.).

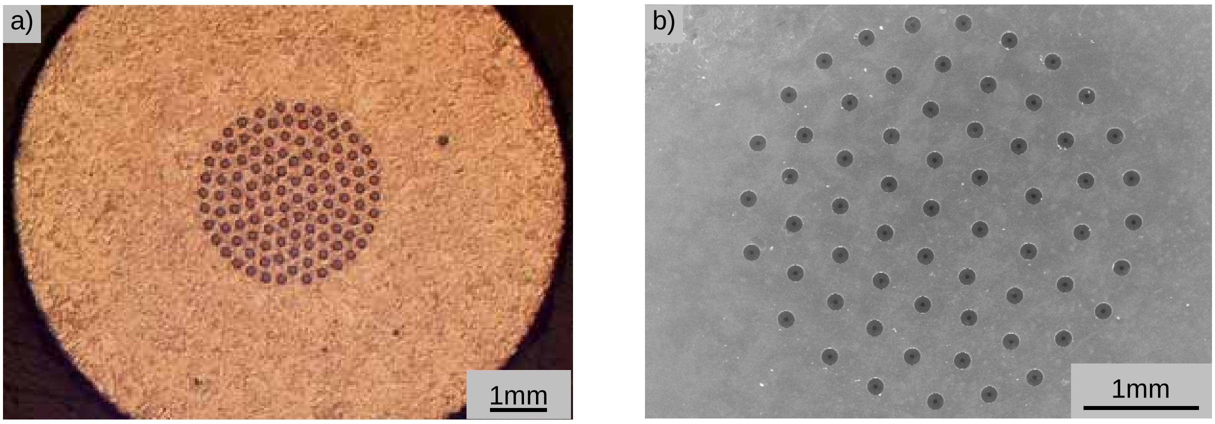

Figure 3.10. Cross-section through the composite after hot isostatic pressing process a) optical micrograph (TSSCuH07); b) SEM micrograph (TestH3)

After hot-isostatic pressing of the pre-heated single coated fibres generally very few pores occurred in the copper matrix. The initial copper coating surface appears as a hexagonal boundary around each fibre (Fig. 3.11.b)) including smaller grains. Locally twin boundaries can be observed. In total the grain size after the complete HIP process is larger than after annealing of the coated fibres.

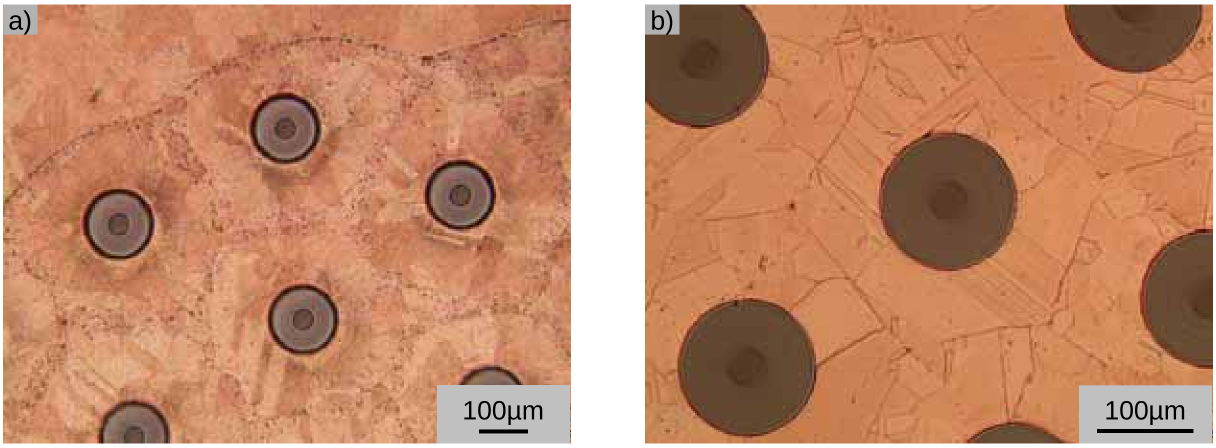

Figure 3.11. Optical micrographs of a: a) high porosity; b) reduced porosity composite

In figure 3.12. optical micrographs of CuTiH4 and CuTiH6 having a different fibre volume fraction are shown. The fibres are uniformly distributed inside the matrix and there is no contact between individual fibres.

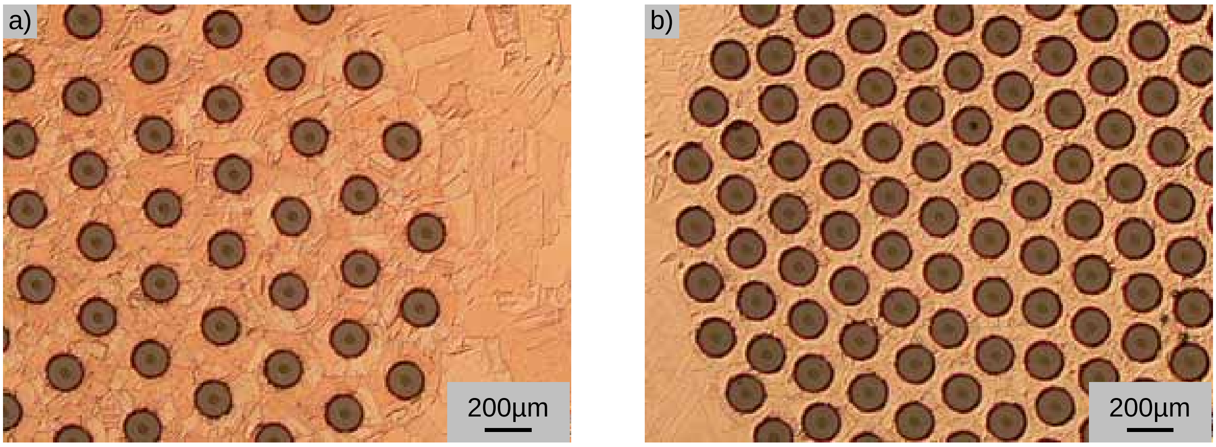

Figure 3.12. Micrographs of composites with different fibre volume fraction a) V_f=17%; b) V_f=38.8%

3.1.5. Impurities

SEM studies in the Cu-matrix of the annealed coated single fibres had shown a few white spots (Fig. 3.13.a)) locally distributed at the grain boundaries. Comparing EDX results obtained for two different regions, one on a clean area (black line) and a second on a white spot (red line) are shown in Fig. 3.10.b)). It was found that the white dots are impurities containing sulphur.

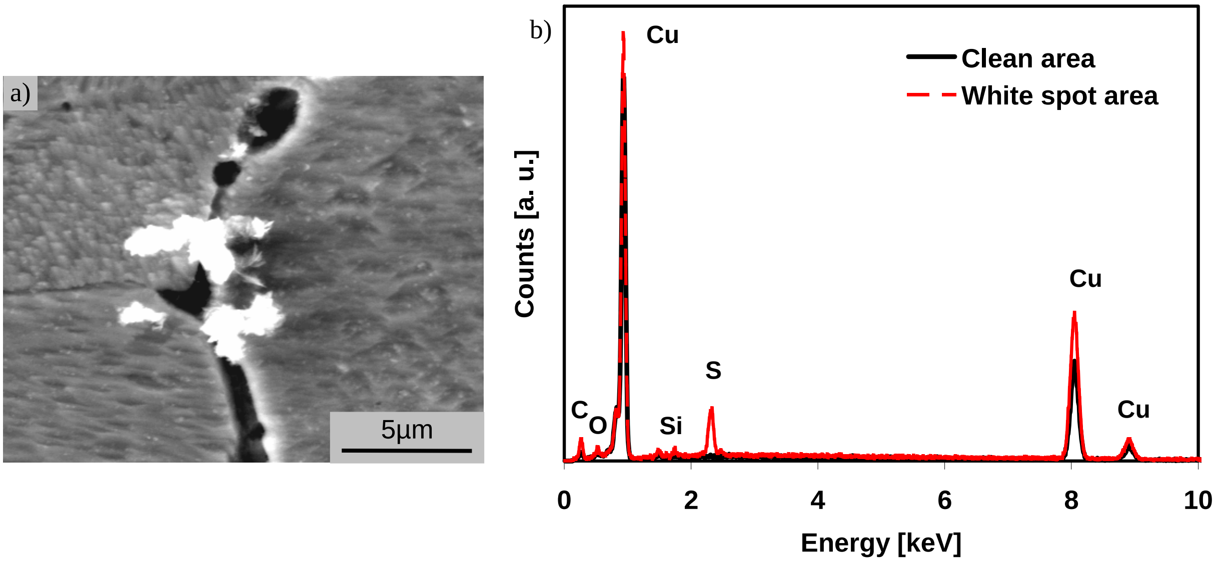

Figure 3.13. Impurities containing sulphur in the copper matrix: a) SEM micrograph showing white spots; b) EDX investigation showing comparative spectra on a clean area and on a white spots

3.1.6. Interface microstructure

The following TEM results were supplied by Prof. Dr. J. Woltersdorf and Dr. E. Pippel, Max-Planck-Institute of Microstructure Physics in Halle, Germany.

3.1.6.1. Interface without fibre surface treatment

The first batches of electrolytic copper deposition were carried out on the SCS-6 fibre without a modified interface.

The interface of an electrolytically coated single fibre was analysed in detail by TEM. Performing an EDX line-scan, an elemental profile over a distance of 100 nm across the interface was measured.

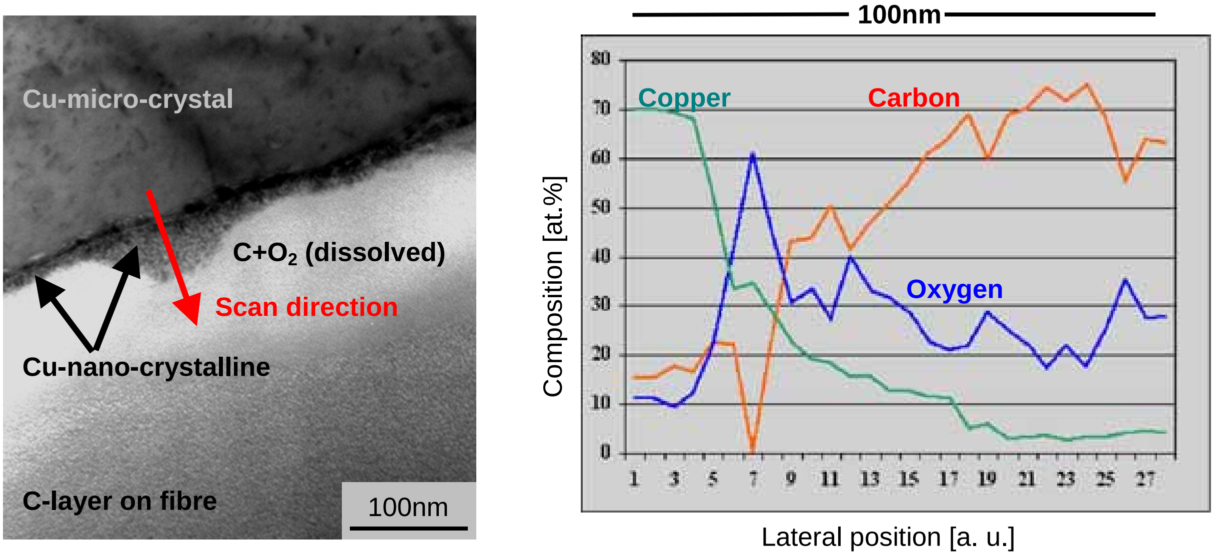

Figure 3.14. Investigation on Cu coated SCS-6 fibres a) TEM micrograph; b) TEM/EDX-line-scan

Following the direction indicated by the red arrow (Fig. 3.14.a)), a copper micro-crystal and a nano-crystalline structure at the interface region are identified. The latter yields a strong copper and oxygen signal and probably consists of copper oxide. The following decrease of the copper signal is accompanied by an increasing carbon signal, indicating the transition from coating to fibre which also contains some oxygen near its surface (blue line in Fig. 3.14.b)).

3.1.6.2. Interface with titanium interlayer

To increase the adhesion between fibre and matrix, a reactive layer was deposited on the fibre surface (CuTi samples) as described in chapter 2.1.2. (table 2.2.). A flat pyrolytic graphite sample (PyC) was also investigated.

<u>Pyrolytic graphite</u>
After annealing at 650°C for 60 min, the interface of the pyrolytic graphite sample was investigated by TEM to obtain information about the formation of TiC and possible diffusion processes.
Fig. 3.15. shows a nano-crystalline TiC layer between substrate and coating. The thickness of the interlayer is irregular and the interface to copper as well as to carbon is strongly interlocked with pronounced adhesion.

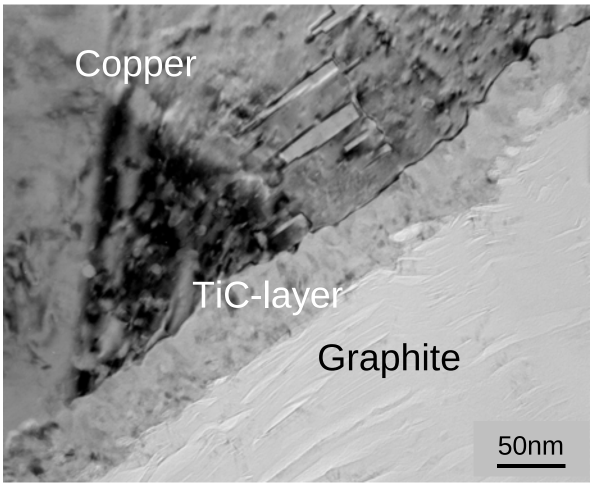

Figure 3.15. TEM micrograph of deposited PyC substrate

An image obtained by high resolution electron microscopy is displayed in figure 3.16. The atomic resolution allows to identify details of the crystal structure in the transition regions between the interlayer and copper coating. As the surfaces are rough, the transition is not sharp, but overlapping electron diffraction patterns are found (see righthand side of figure 3.16.).

These patterns also allow crystallographic statements about the selected range. The lattice constant determined form the diffraction pattern of the upper right zone marked in the image matches the value of TiC.

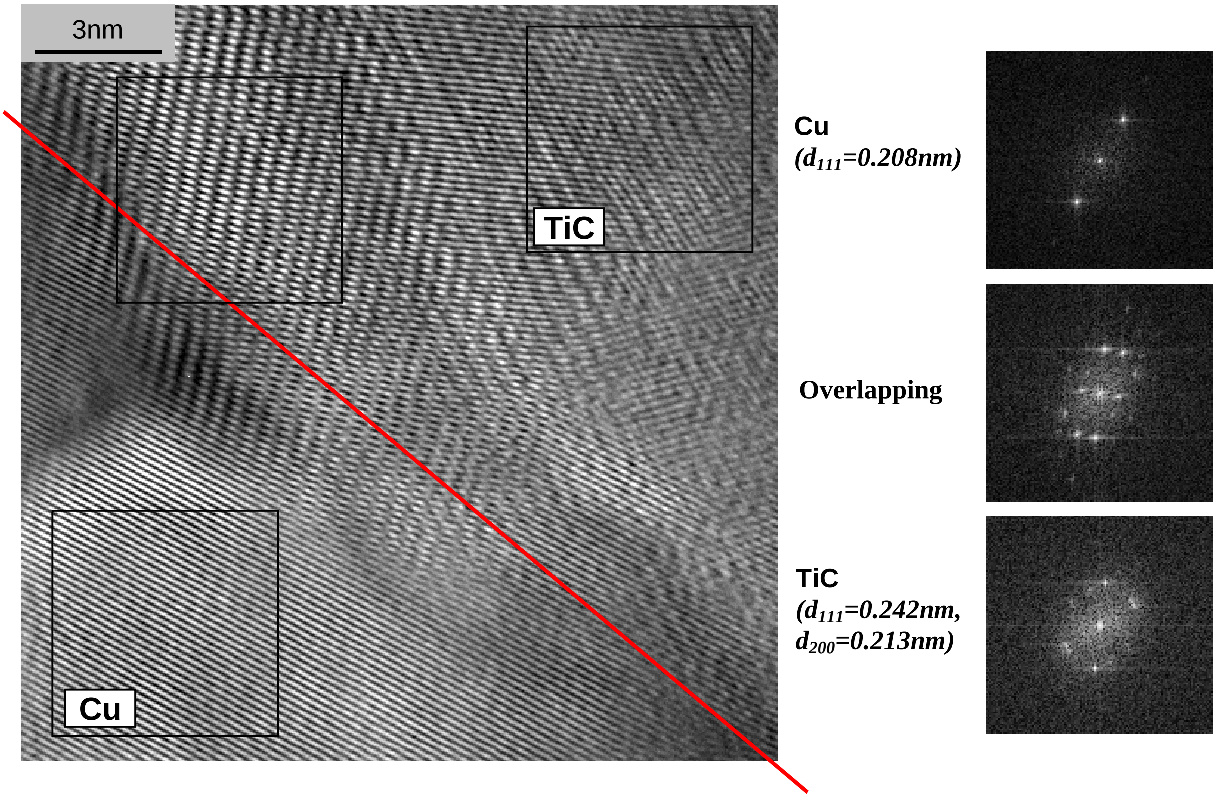

Figure 3.16. HREM image of the overlapping zone between TiC and copper on PyC substrate (on the right side electron diffraction patterns of the marked areas)

Quantitative x-ray microanalysis yields a laterally resolved measure of the chemical composition. The respective elemental distribution was measured in various points along the

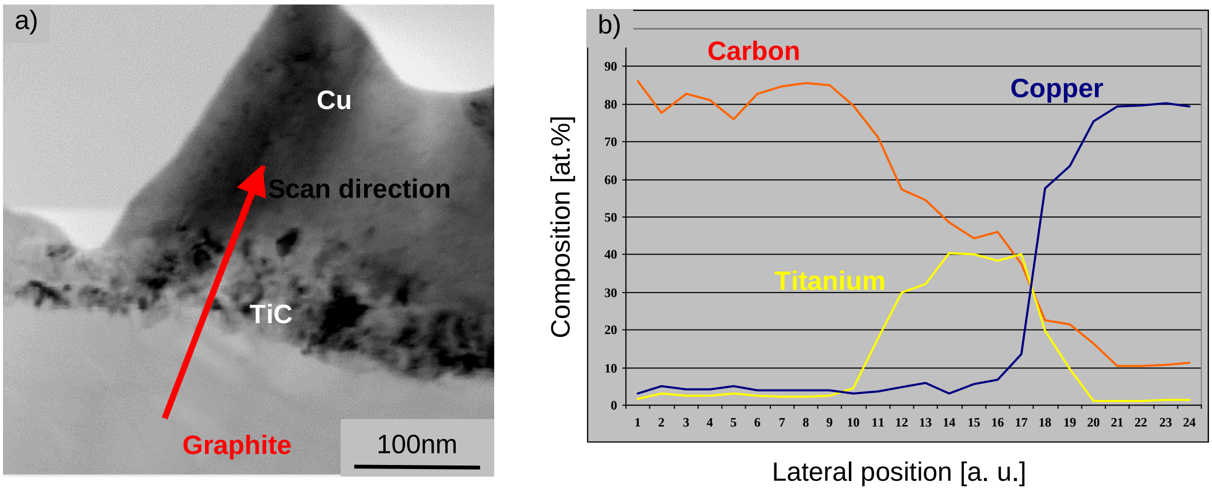

Figure 3.17. Investigation on deposited PyC substrate a) TEM micrograph; b) TEM/EDX-line-scan

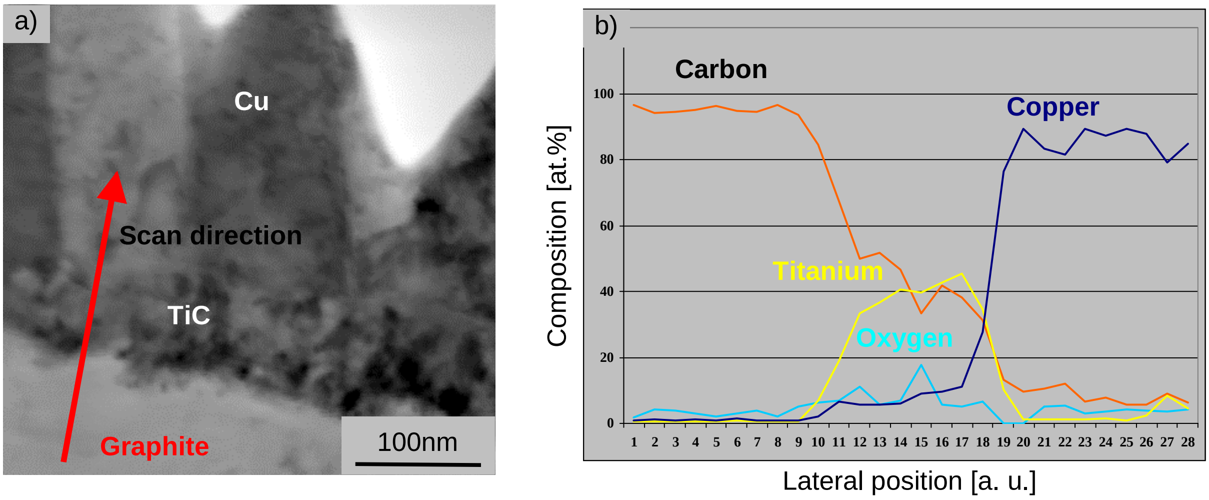

Figure 3.18. Investigation on deposited PyC substrate a) TEM micrograph; b) TEM/EDX-line-scan

red lines marked in Fig. 3.17.a) and Fig. 3.18.a). The resulting diagram (see Figs. 3.17.b) and 3.18.b)) shows roughly stoichiometric composition of the TiC layer. It is crystalline with crystal sizes in the range of some nanometers.

The EDX line-scans also show a prompt decay in the titanium signal at the copper interface. From this observation it can be concluded that no significant diffusion has occurred there. The EDX line-scan from Fig. 3.18.b) also comprises oxygen content determination, showing an amount of oxygen inside the TiC layer.

<u>Fibre</u>

The interface of PVD coated fibres (CuTi05.3 and CuTi05.4) was investigated similarly. The samples were heat treated like the PyC sample described above.

Granular crystalline copper was found with a thickness of 290 nm and a fine crystalline TiC layer having a thickness of 55 nm.

As can be clearly recognised in figure 3.19., there is a bright layer of about 200 nm between the fibre surface and the TiC coating. The EDX line-scan along the red arrow in figure 3.19. shows an oxygen enriched carbon layer, while silicon is first detected in the darker fibre area. Contrary to the PyC sample, the TiC layer does not show an increased oxygen content.

The titanium curve shows a rapid decay at point 5 (Fig. 3.19.b)), while the copper signal extends into the TiC layer. This shows clearly, that diffusion of copper into the titanium carbide layer occurs, while diffusion of Ti into copper does not take place.

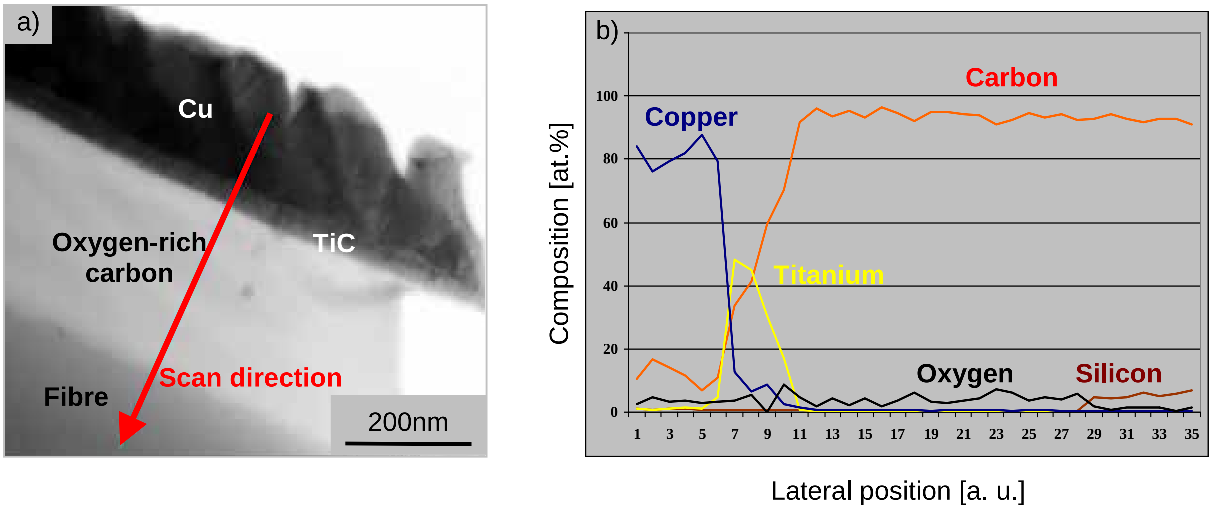

Figure 3.19. Investigation on Cu-Ti SCS-6 fibre a) TEM micrograph; b) TEM/EDX-line-scan

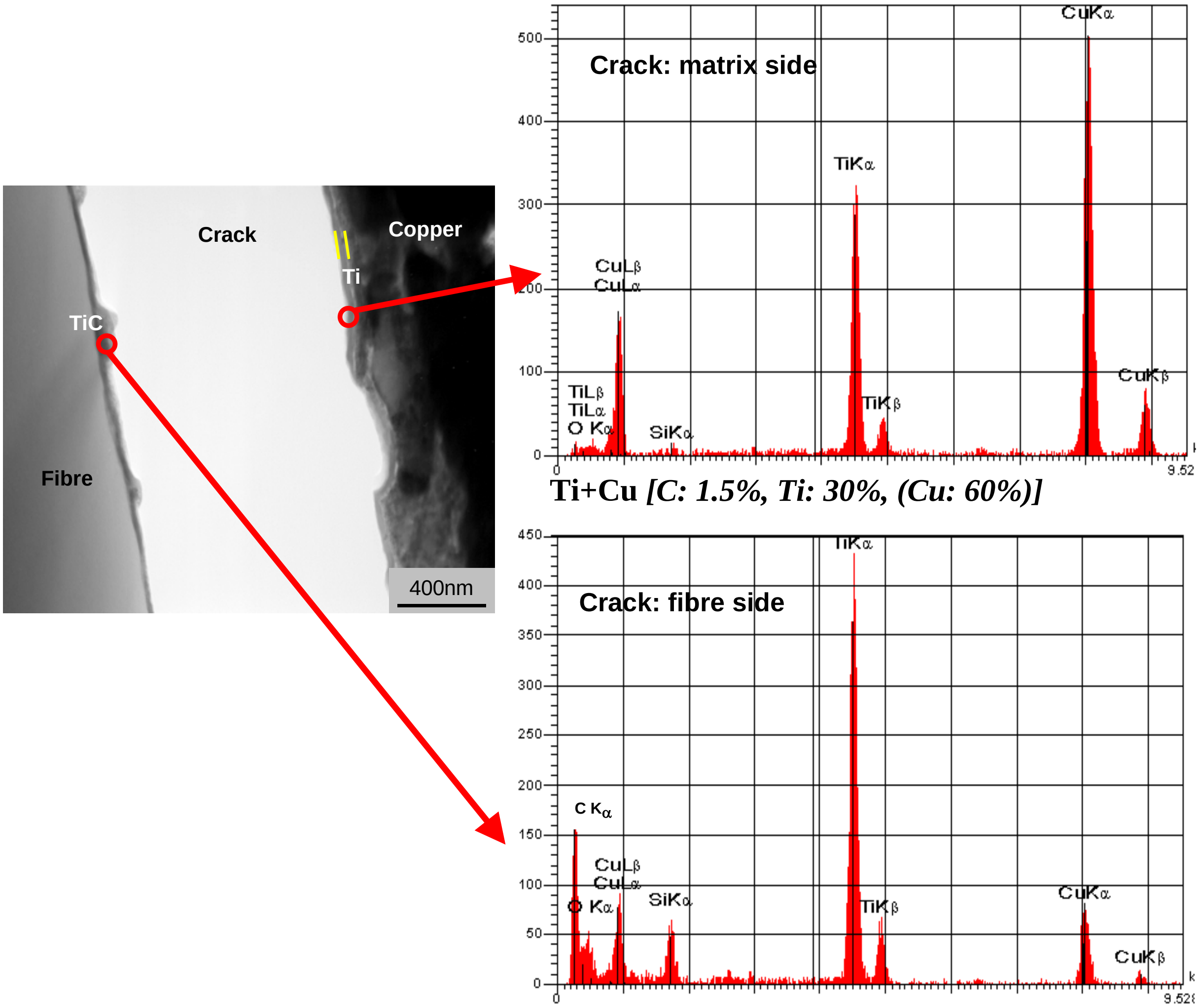

Ti+Cu ***[C: 1.5%, Ti: 30%, (Cu: 60%)]***

TiC+C ***[C: 72%, Ti: 18%, (Cu: 3%)]***

Figure 3.20. CuTi05.4 EDX point measurements

Figure 3.20. shows an undesired crack at the interface of sample CuTi05.4.
EDX measurements were performed on both the fibre and the Cu-coating side of the crack. The elemental distribution on the fibre side shows very little copper, some titanium, and a high carbon content, suggesting the presence of TiC. On the copper side titanium is present,

but the carbon content is very low. From this observation it can be concluded, that the crack formation took place within the titanium layer and before any significant diffusion of carbon throughout the whole layer thickness had occurred.

3.1.7. Thermal cycling

To study the composite behaviour under cyclic thermal loads, specimens with different interface (TSSCuH07, CuTiH2, CuTiH4) were thermally cycled 120 times between 350°C and 550°C with a rate of 4 K/min in a vacuum oven. The cycled specimens were investigated with the scanning electron microscope.

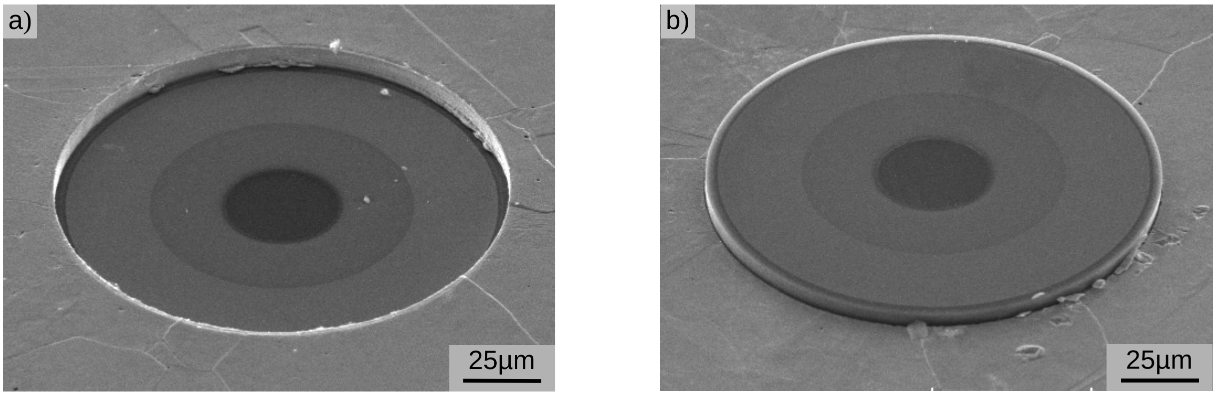

Figure 3.21. Representative SEM micrographs of TSSCuH07 composite fibres after thermal cycling

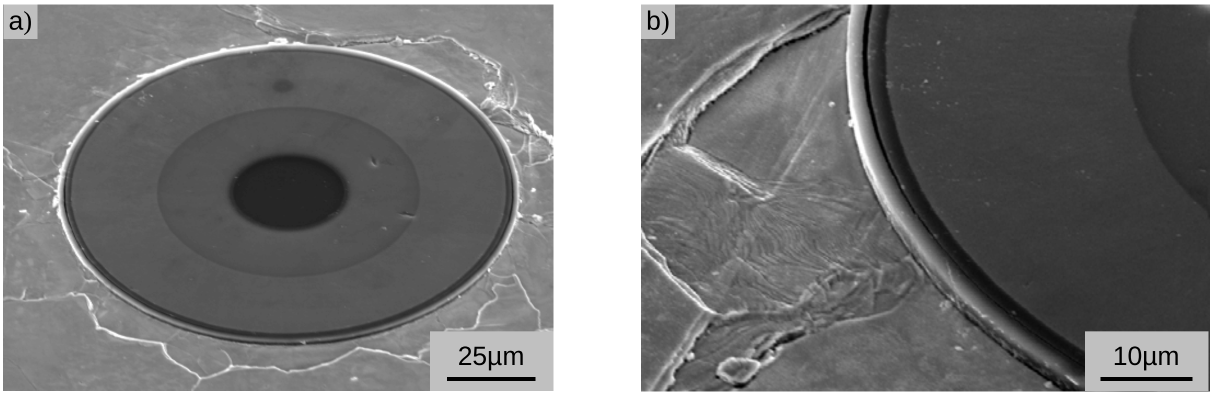

Figure 3.22. Representative SEM micrographs of CuTiH composites after thermal cycling

The micrographs presented in Fig. 3.21. show the results for TSSCuH07 specimen. Some of the fibres were found to slide into the matrix (Fig. 3.21.a)) while others moved in the opposite direction (Fig. 3.21. b)). Before the experiment all the fibres were situated about 1-2 µm outside of the matrix due to polishing, while afterwards the displacement in both directions was about 5 µm. A gap appears around the fibres between the carbon coating and the copper matrix.

The same investigations for specimens of CuTiH2 and CuTiH4 composites had shown no fibre displacement either in or out of the matrix. All fibres were found outside of the matrix at the same distance as before the experiment (1-2 µm). In comparison with TSSCuH07 a conspicuous structure was observed in the copper matrix around the fibre. It looks like a grain boundary, possibly caused by dislocation migration in the region close to the fibre (Fig. 3.22.a)).

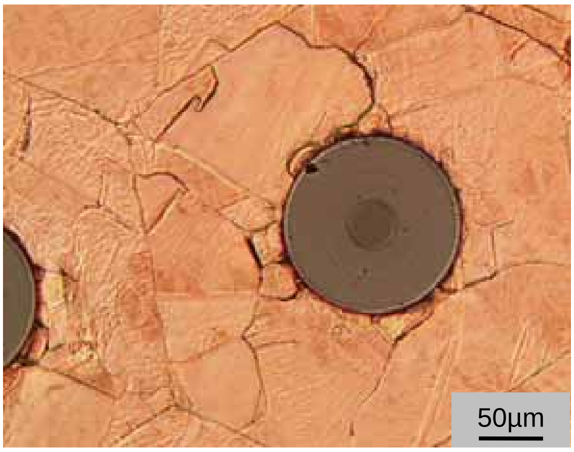

Figure 3.23. Optical micrograph of CuTiH2 after thermal cycling

A closer look at the interface shows complete debonding between the carbon coating layers of the fibre. For some fibres also a gap between the carbon coating and the copper matrix becomes visible, but not over the entire fibre circumference (Fig. 3.22.b)).
Strong grain growth is visible in Fig. 3.23. but not across the hexagonal formation around the fibre.

3.2. Mechanical properties

3.2.1. Microhardness and Young's modulus measurements

To observe the dependence of the microhardness estimation on the indentation depth, test measurements on a copper single crystal were performed.

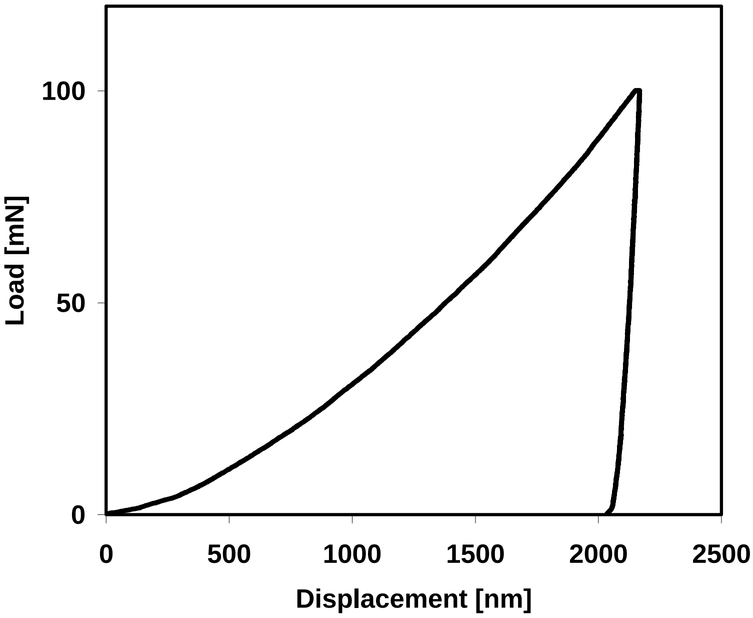

Figure 3.24. Typical load versus displacement curve obtained during a loading-unloading cycle characteristic for copper

The influence of different processing parameters was investigated by indentation measurements in the copper matrix on both untreated and heat treated individual coated fibres with and without titanium interlayer and in the corresponding composites.

To avoid an influence of the neighbour indentation, all experiments were carried out keeping a distance of 80-100 µm between the indentations. Attention was paid that the minimum distance to a fibre was about 20 µm [134].

Figure 3.24. shows a typical load-displacement curve obtained by indentation in copper at 100 mN load. The hardness and Young's modulus were calculated for the investigated samples on the basis of the Oliver and Pharr method described in chapter 2.2.3.1. An average value was derived from 10-20 experiments for each sample.

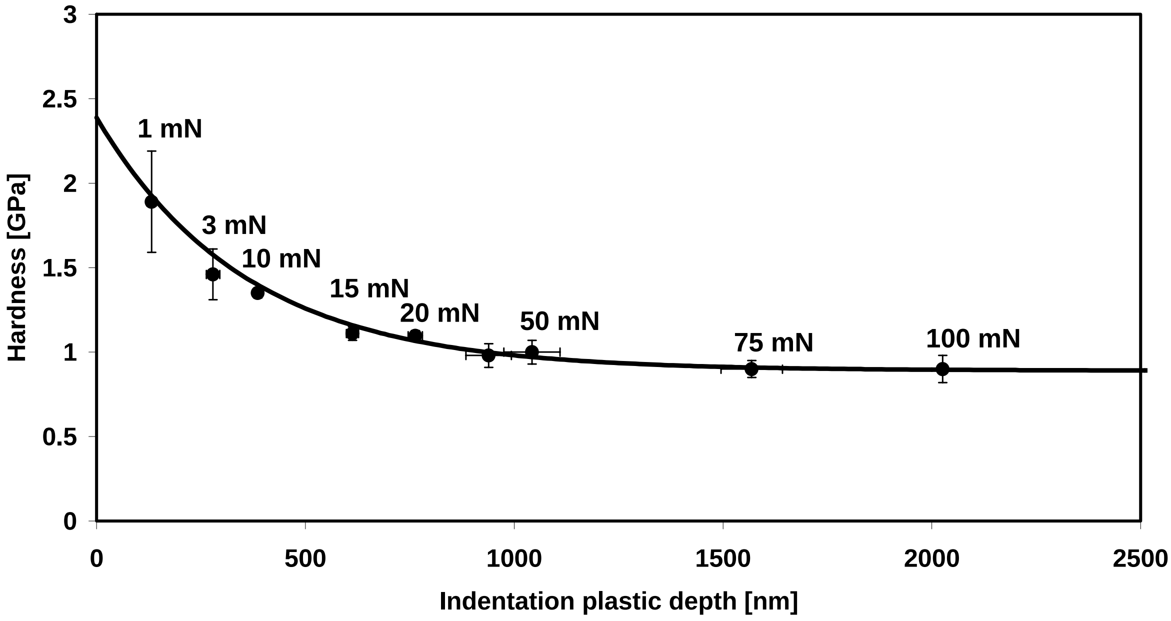

Figure 3.25. Calculated hardness versus indentation depth for copper single crystal

Copper single crystal

To check if the NanoTest device is working properly, hardness measurements were done in a copper single crystal with (111) orientation at different loads varying from 1 mN to 100 mN. At each load ten measurements were performed from which the curves which strongly deviate from the typical form (Fig. 3.24.) were deleted and the remaining were averaged. The received values are presented in Fig. 3.25. where hardness versus plastic depth is plotted.

Single coated fibres

For the determination of possible matrix hardening by the introduced fibres, microhardness measurements were performed in the annealed copper coating of the single coated fibres at different distances from the fibre. The individual hardness values obtained from 100 mN load indentations versus the distance from the fibre surface in each sample are shown in Fig. 3.26. A correlation of the hardness with the distance from the fibre was not found. The evaluated mean values are in the range between 0.8 GPa and 0.85 GPa.

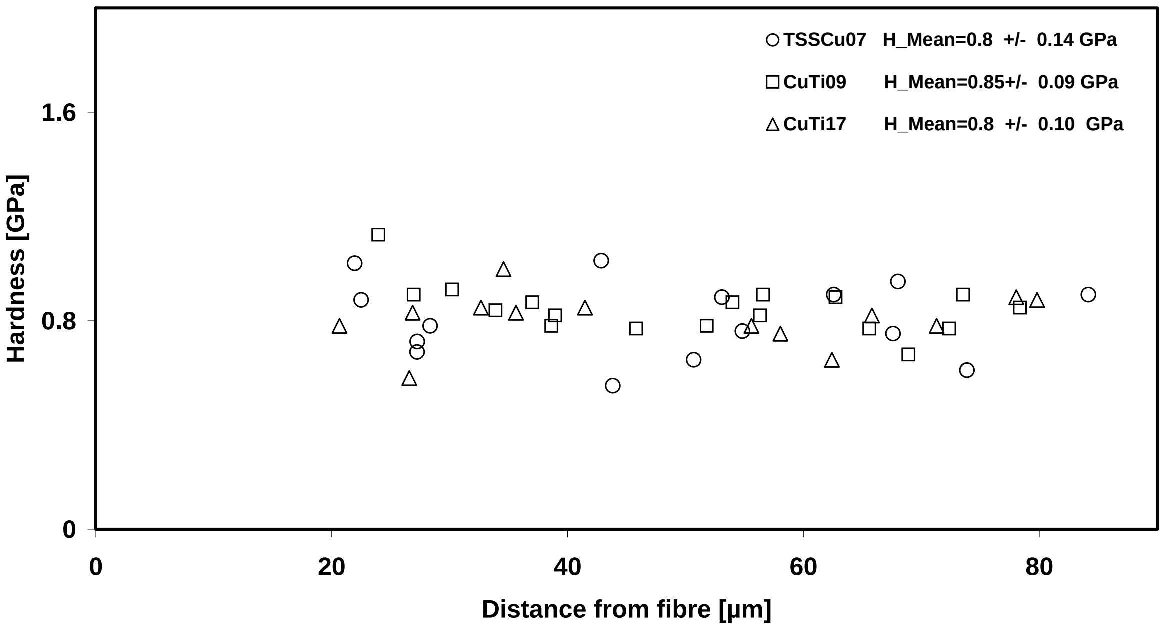

Figure 3.26. Copper hardness values for annealed single coated fibres versus the distance to fibre surface

Figure 3.27.a) shows an optical micrograph for representative indentation traces in a heat treated copper coated single fibre. Some magnified indentations and the corresponding hardness values are shown in Figure 3.27.b).

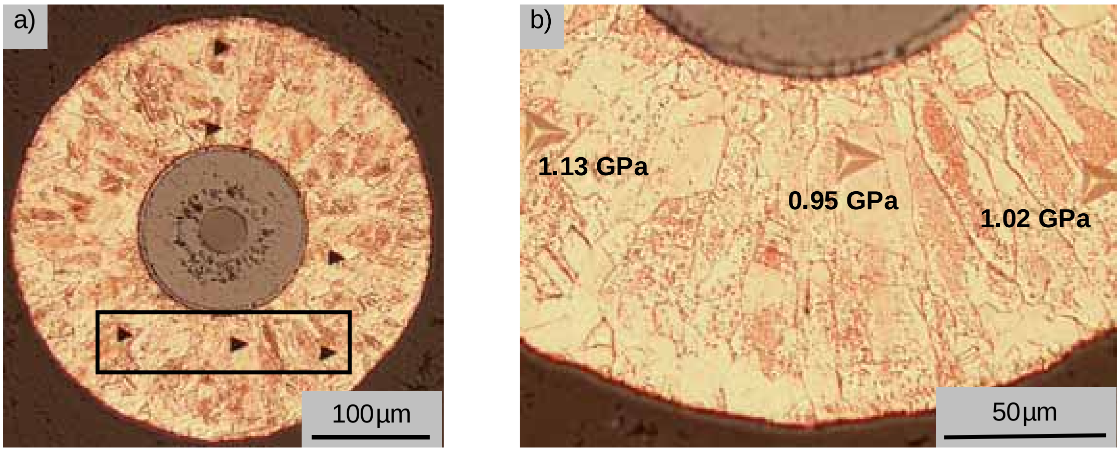

Figure 3.27. Optical micrographs showing hardness measurements in a single coated fibre a) indentation traces; b) magnified image of the indentation traces with the corresponding hardness values

Composite

For comparison with the electrolytic copper matrix within the composite, indentation experiments were performed in the copper capsule region on composite specimens obtained after HIP’ing (Fig. 3.28.). Hardness and Young’s modulus were derived. The indentation traces and the mean values are shown in the figure.

The matrix microhardness was measured in composites with different interface in the reinforced zone. The optical micrographs (Fig. 3.29.a)) show representative indentation traces in the composite. Figure 3.29.b) is an magnification of image 3.28.a) showing some indentations and the corresponding hardness values.

The averaged values are displayed in figure 3.30. in comparison with the averaged values for coated single fibres, unheated and heated to 550°C. The calculated standard deviation is attached.

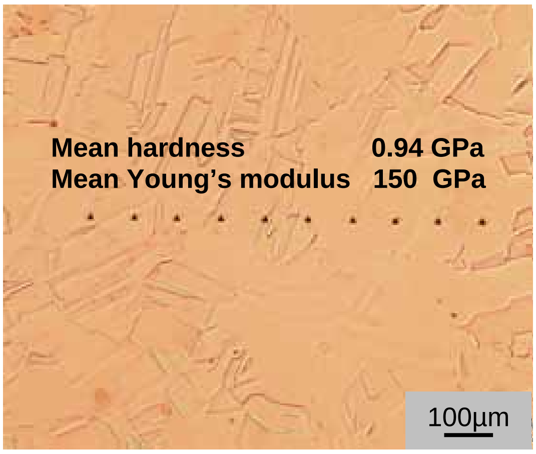

Figure 3.28. Micrograph showing indentation traces in the copper capsule region

In the composite reinforced zone, hardness values between 0.77 GPa and 0.91 GPa were determined for the Cu-matrix while the average values for the coated single fibres without heat treatment were found to be between 0.97 and 1.57 GPa. The Young's modulus was derived respectively, the average values and the standard deviations for different investigated samples are shown in Fig. 3.31.

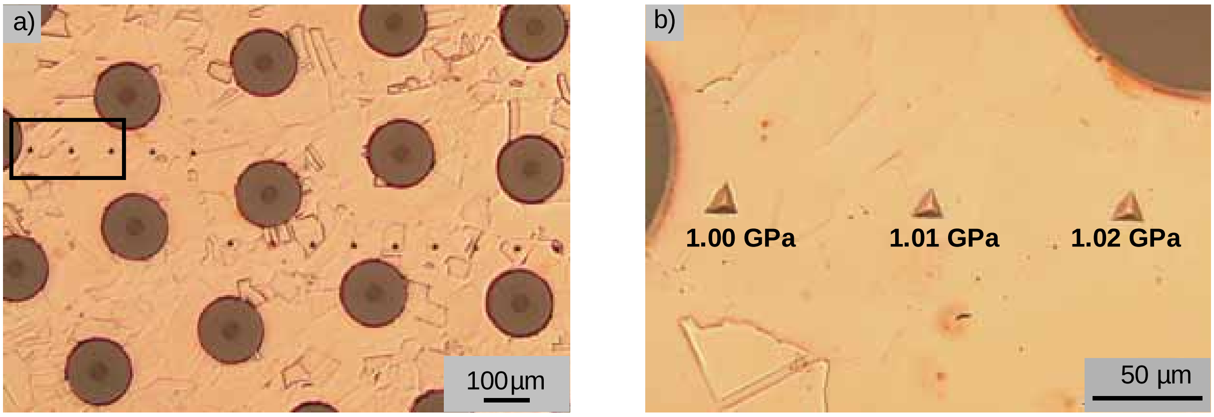

Figure 3.29. Optical micrographs showing representative hardness measurements in a composite; a) indentation traces; b) magnified image of the indentation traces with the corresponding hardness values

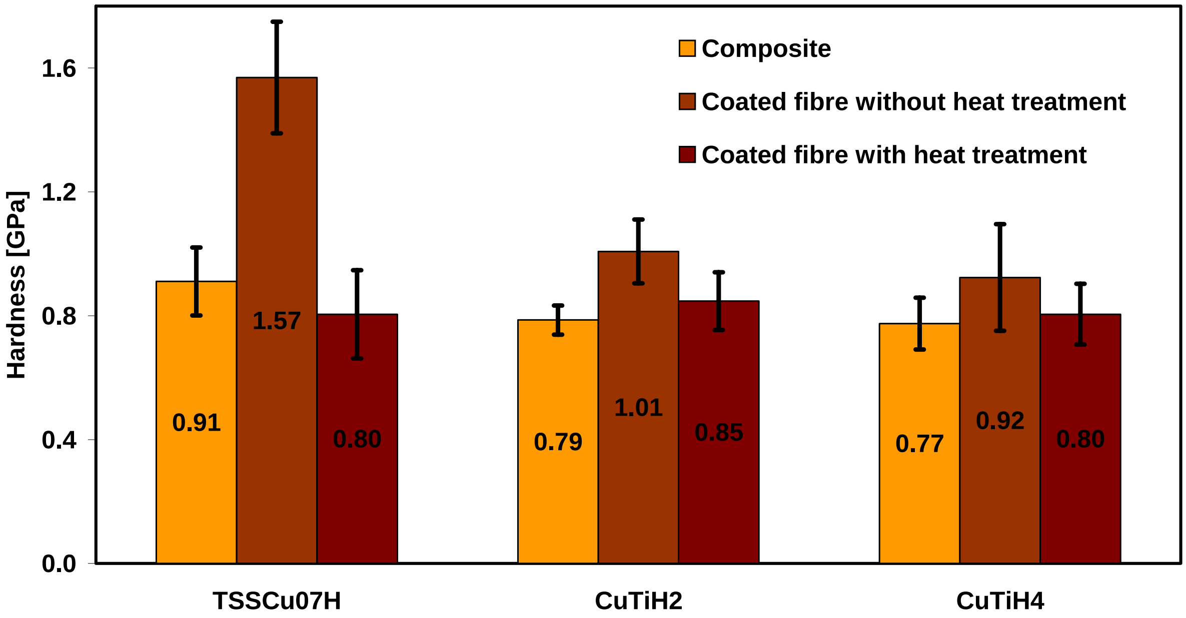

Figure 3.30. Mean hardness values of the copper phase for different investigated composites and their corresponding copper coated single fibres

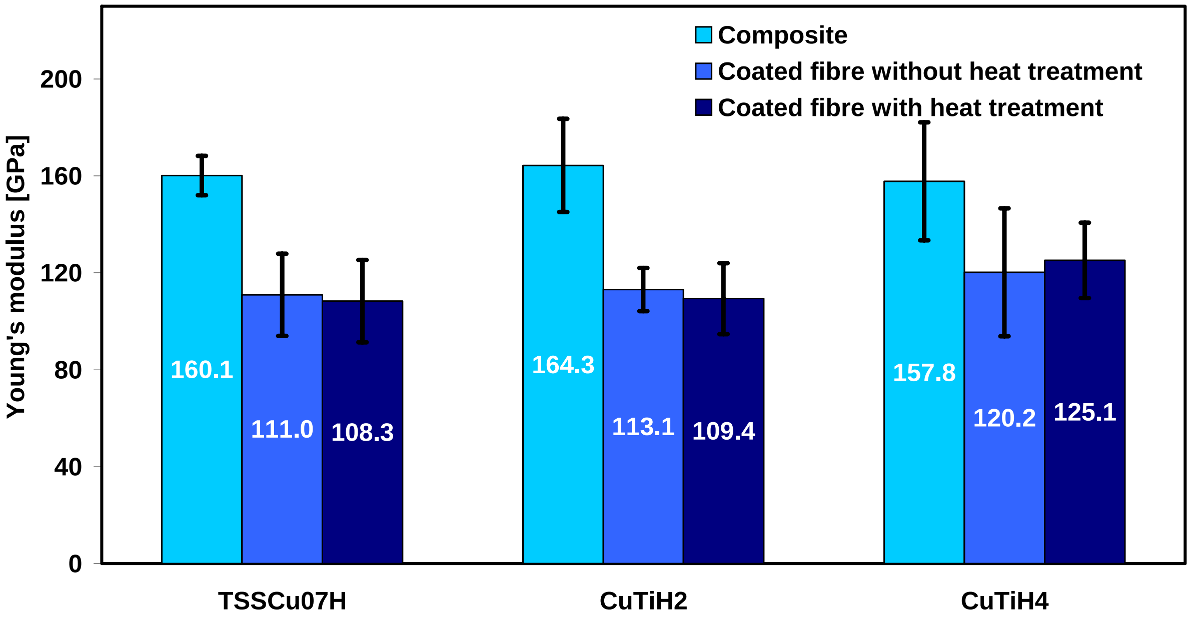

Figure 3.31. Mean Young’s modulus values of the copper phase for different investigated composites and their corresponding copper coated single fibres

3.2.2. Push-out measurements

To characterise the fibre/matrix interface, push-out tests were performed on different composite specimens.

First measurements on TestH3 composite samples (without Ti interlayer, see chapter 2.1.5.) were carried out with the micro-head of the nanoindenter-device, allowing only load-controlled experiments up to a force of 20 N. All further experiments were performed using the improved depth-controlled push-out test in the universal testing device, allowing higher forces to push-out the strong bonded fibres with titanium carbide interface and the measurement of load reduction during the experiment. The TSSCuH07 composite was tested for comparison with the nanoindenter results and two composites with improved interface (CuTiH2 and CuTiH4), distinguished by different titanium-coating thickness.

Load and indenter-displacement were recorded during the test. In the load-displacement curves the debonding load P_d, the maximum load P_{max} and the frictional load P_{fr} are taken from the characteristic points.

According to the models described in chapter 1.3.4., the interfacial parameters were computed.

<u>Composites without Ti-interface</u>

<u>TestH3-Composite</u>

Specimens with thicknesses of 2.55 mm, 2.8 mm, and 3.55 mm were sawed from the TestH3 composite and push-out specimens were prepared as described in chapter 2.2.1. The samples were placed on the holder as described in chapter 2.2.3.2. and about 15 fibres were pushed-out with the micro-head of the nanoindenter device for each thickness. Typical load-displacement curves for the fibre push-out obtained from the nanoindenter are shown in Fig. 3.32. The initial debonding load was determined from the first deviation from linearity. Sometimes the deviation was well marked by a sudden change in the displacement. The maximum load registered by the NanoTest device was interpreted as the sliding friction force.

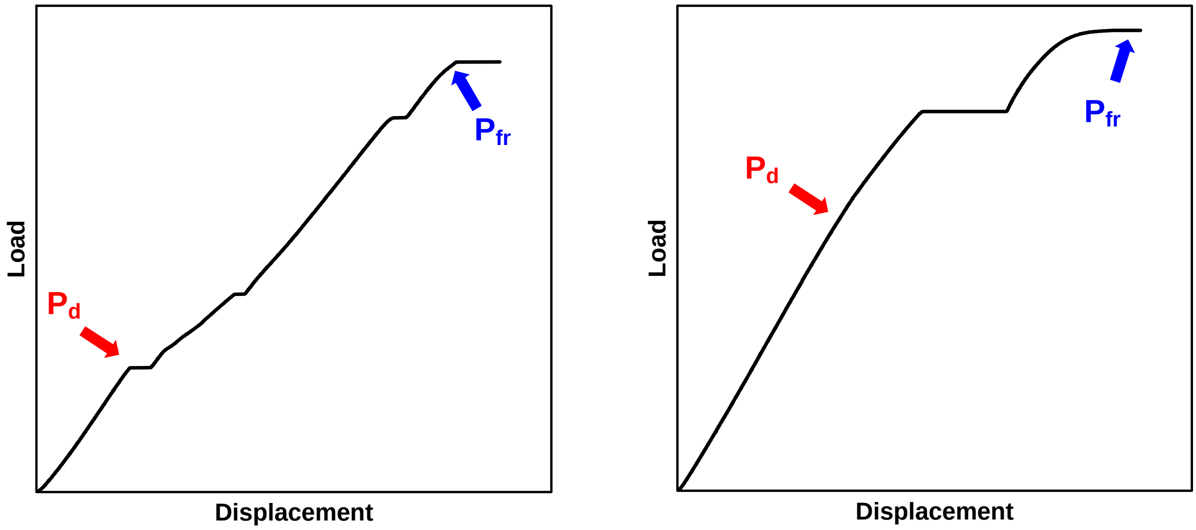

Figure 3.32. Typical load-displacement curves measured with the NanoTest device

The average load values shown in table 3.2. were plotted versus the sample thickness and the points were least square fitted using the formulas (1.26.) and (1.30) explained in chapter 1.3.5.

Sample	Thickness [mm]	Mean P_d [N]	Mean P_{fr} [N]
TestH3	2.25	3.13	6.48
	2.8	4.96	13.53
	3.55	3.85	15.54

Table 3.2. Mean push-out characteristic loads for different thicknesses

The obtained diagrams containing a standard deviation error bar are graphed in Fig. 3.33. An interfacial shear strength of 5 MPa and an interfacial frictional stress of 5.87 MPa were determined, summarised in Fig. 3.36. The interfacial frictional stress is calculated to be higher than the interfacial shear strength. This is discussed in chapter 4.2.2.1.

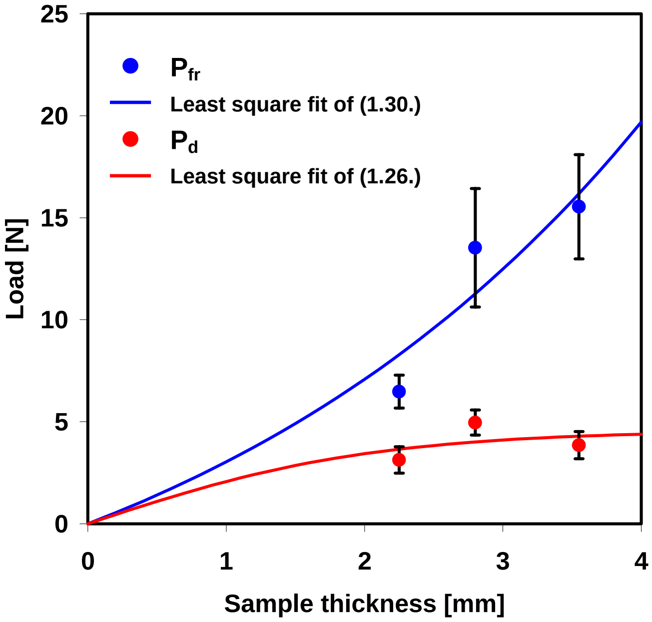

Figure 3.33. Fit of the push-out results of TestH3 composite

As SEM investigations of the tested samples show no difference to TSSCuH07-Composite, principle views can be seen in the end of TSSCuH07 push-out results summary (Fig. 3.37. and 3.38.).

TSSCuH07-Composite

Measurements on TSSCuH07 samples with a thicknesses of 1.35 mm, 1.5 mm, 2.3 mm and 3.02 mm were performed in the push-out setup of the universal testing device. The thicknesses were chosen to be comparable to the thicknesses investigated with the NanoTest device.

During the tests it was found that the load versus displacement curves can differ considerably. Three measured curves are shown in Fig. 3.34., representative examples for the observed principal types. Although showing different shapes, the characteristic loads were comparable for each measured thickness. Thus the corresponding values were averaged and used for calculation.
The initial debonding load P_d was taken at the point were the load-displacement curve deviates from linearity. The frictional sliding force was determined as shown in the example figures.

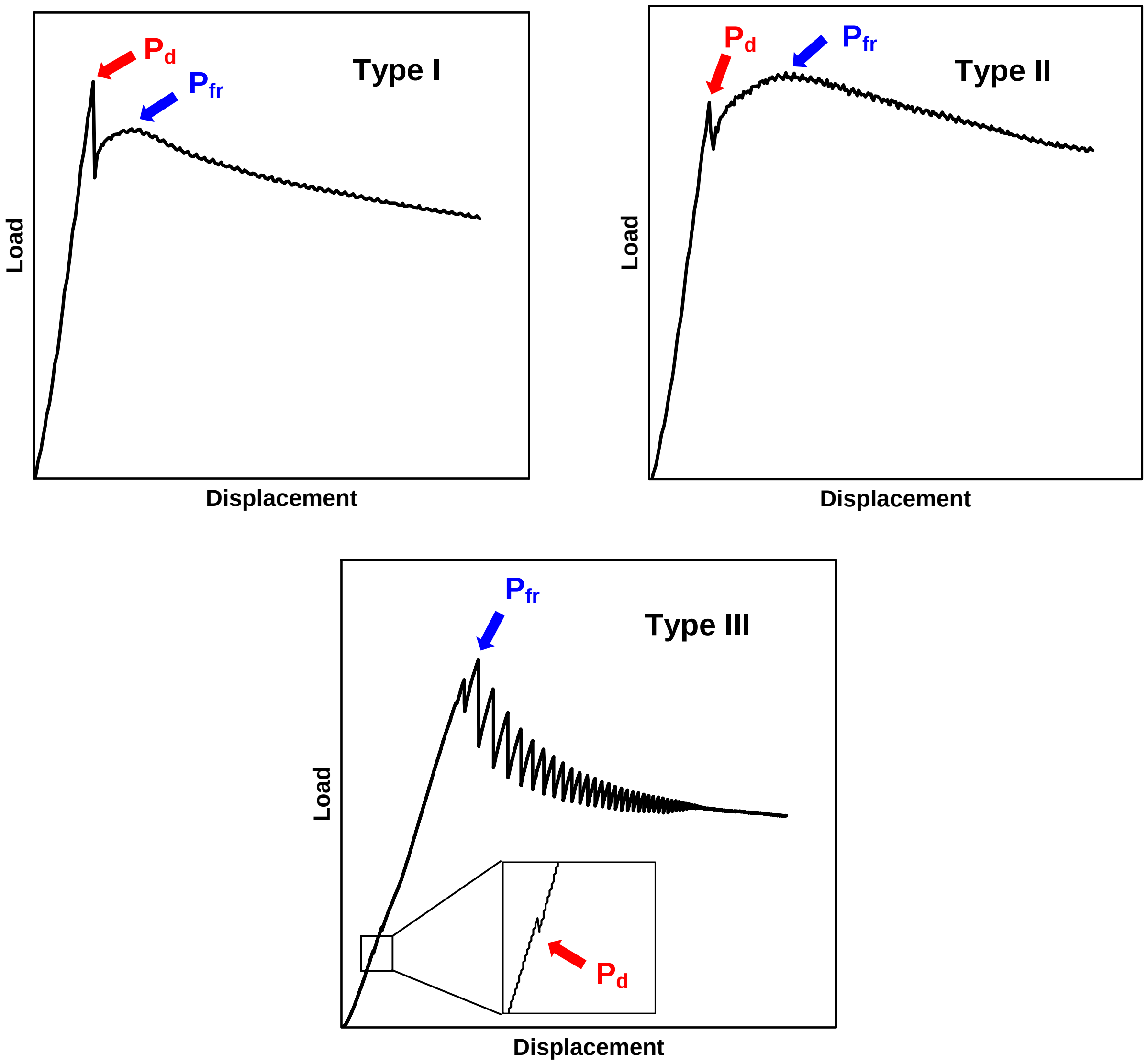

Figure 3.34. Typical load-displacement curve-types measured with the universal testing device for TSSCuH07 samples. The relation between the significant forces can be different, as to be seen in table 3.4.

For each specimen the average values for debonding and friction load were acquired from up to 20 push-out tests. Again the average load values shown in table 3.3. were plotted versus the sample thickness and the points were least square fitted using the formulas (1.26.) and (1.30.). The obtained diagrams containing a standard deviation error bar are graphed in Fig. 3.35. An interfacial shear strength of 5.38 MPa and an interfacial frictional stress of 3.4 MPa were determined and are summarised in Fig. 3.36.

Sample			**Type I**			**Type II**			**Type III**		
	Thickness [mm]	Count #	Occ. [%]	Mean P_d [N]	Mean P_{fr} [N]	Occ. [%]	Mean P_d [N]	Mean P_{fr} [N]	Occ. [%]	Mean P_d [N]	Mean P_{fr} [N]
TSSCuH07	1.35	10	10	2.6	2.3	-	-	-	90	2.1	2.3
	1.5	2	50	4.3	4.0	-	-	-	50	3.5	4.2
	2.3	13	-	-	-	29	5.1	12.5	71	5.9	12.8
	3.02	20	-	-	-	85	3.6	18.4	15	7.9	21

Table 3.3. Occurrence and mean push-out characteristics loads for each push-out curve type for TSSCuH07 sample

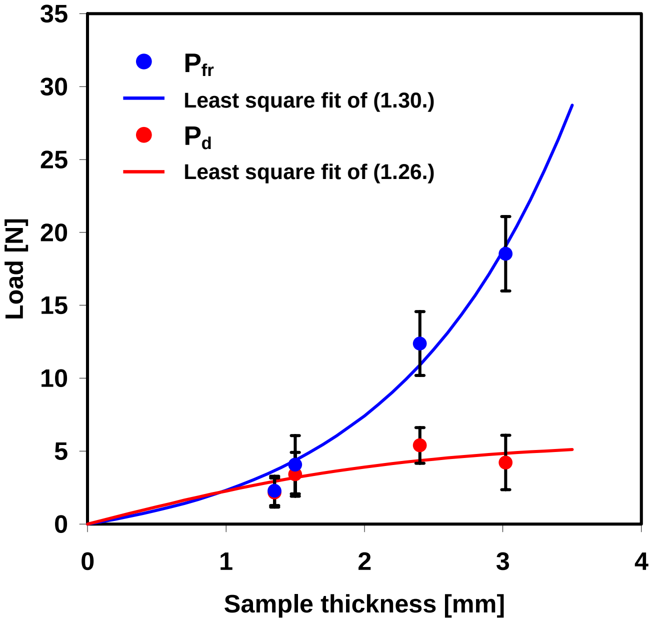

Figure 3.35. Results of the push-out tests in TSSCuH07 composite

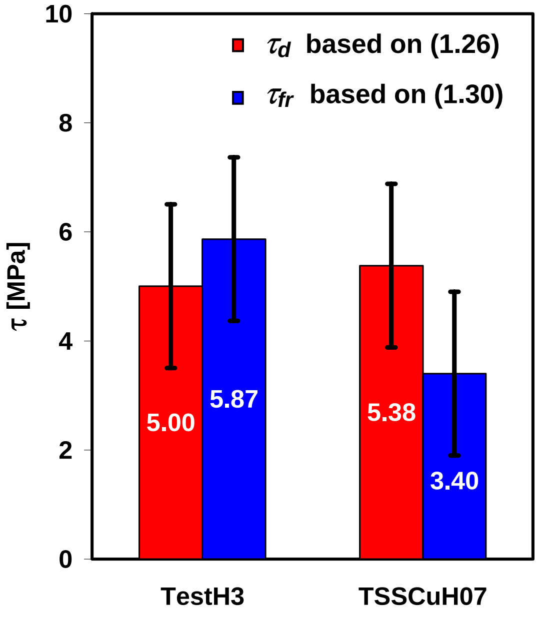

Figure 3.36. Interfacial parameters (τ_d and τ_{fr}) for composite without titanium interface

Figure 3.37 shows scanning electron micrographs of the TSSCuH07 samples after push-out. Fig. 3.37.a) shows the top surface of a push-out sample from which fibres were pushed out of the matrix and Fig. 3.37.b) shows the backside of the same sample. All specimens show qualitatively the same appearance after the test. No distortion of the Cu matrix was found on either top or bottom face of the samples.

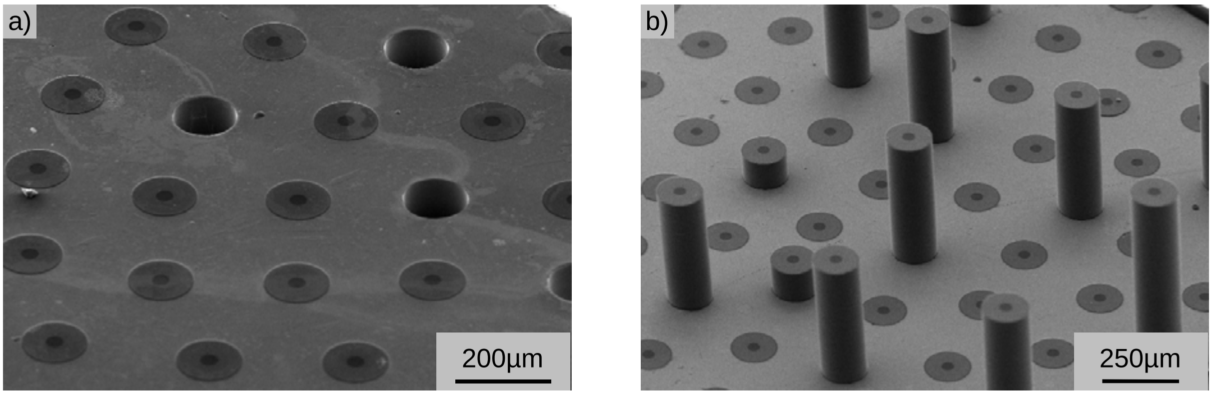

Figure 3.37. Representative SEM micrographs for TSSCuH07 sample after push-out: a) top surface; b) bottom surface

A closer look at the pushed-out fibres (EDX analyses) revealed that the interfacial debonding occurred between the outermost fibre carbon layer (see chapter 2.1.1.) and the copper matrix (Fig. 3.38.). It is also visible in Fig. 3.38. that no fibre coating debris remained on the copper matrix wall after push-out, and also no traces of copper were found on the pushed fibres. Only some brush marks are visible.

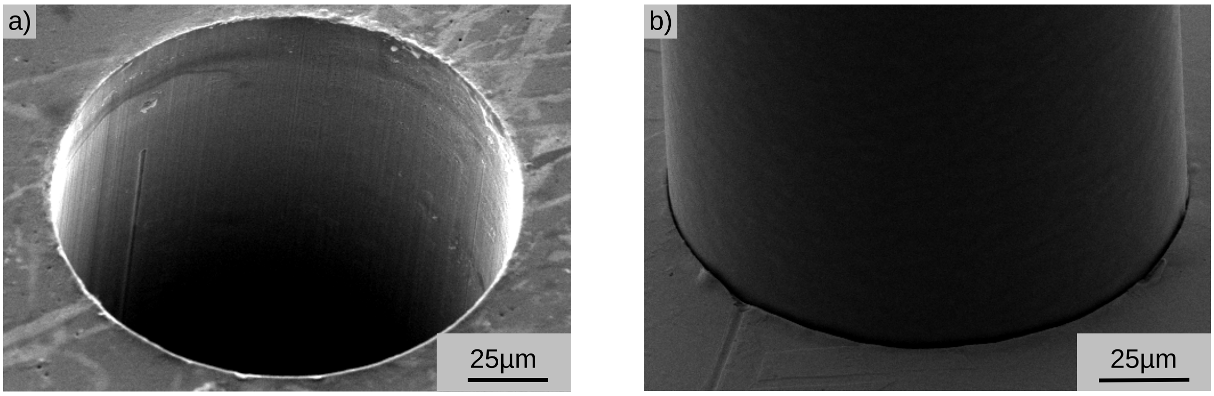

Figure 3.38. a) Push-out hole in TSSCuH07; b) Pushed-out fibre in TSSCuH07

Composite with titanium-interface

Two composites with different modified Ti-interface were investigated using the push-out setup of the universal testing device. The thicknesses of the investigated samples cut from the CuTiH2 composites are 0.8 mm and 1.25 mm and for CuTiH4 are 0.45 mm and 0.9 mm.

Typical load-displacement curves obtained for composites with a titanium carbide interface are shown in Fig. 3.39. Three types of push-out behaviour were noticed. Type Ti-I a) and b) show a linear region which transforms slowly into an non-linear region that ends in a wide peak at the maximum load. The load decreases slowly followed by a sudden load drop indicating the complete debonding and the frictional sliding. While the load decreases slowly with slide propagation (Type Ti-I a)) it is sometimes a little bit increased first (Type Ti-I b)).
The other types also consist of a linear region slowly bending with debond initiation. Type Ti-II shows a sudden load drop at the maximum load (catastrophic debonding) while for type Ti-III a slower load reduction during debonding is noticed, before the curves turn over into frictional behaviour.
The maximum load for types Ti-II and Ti-III was considerably smaller than the maximum load measured in the experiments showing type Ti-I behaviour. Types Ti-II and Ti-III can be allocated to the pushed fibres showing no matrix deformation and were only rarely noticed. Type Ti-I was predominant (see table 3.4.).

Sample			**Type Ti-I**			**Type Ti-II**			**Type Ti-III**		
	Thickness [mm]	Count #	Occ. [%]	Mean P_d [N]	Mean $P_f r$ [N]	Occ. [%]	Mean P_d [N]	Mean P_{fr} [N]	Occ. [%]	Mean P_d [N]	Mean P_{fr} [N]
CuTiH2	0.8	15	80	22	18.8	20	20.7	9.6	-	-	-
	1.25	15	53	32	28	47	26.7	10.5	-	-	-
CuTiH4	0.45	16	87	12.1	8.4	-	-	-	13	6.5	1.9
	0.9	17	70	26.5	28.2	18	24.5	8.9	12	10.41	3.2

Table 3.4. Occurrence and mean push-out characteristics loads for each push-out curve type for CuTiH samples

Calculations of the interfacial shear strength and interfacial friction stress were done considering only the type Ti-I experiments. Therefore the initial debonding load P_d was determined from the deviation of linearity of the load-displacement curve and the frictional load P_{fr} from the beginning of the sliding part of each curve as indicated by the red and blue arrows (Fig. 3.39.).

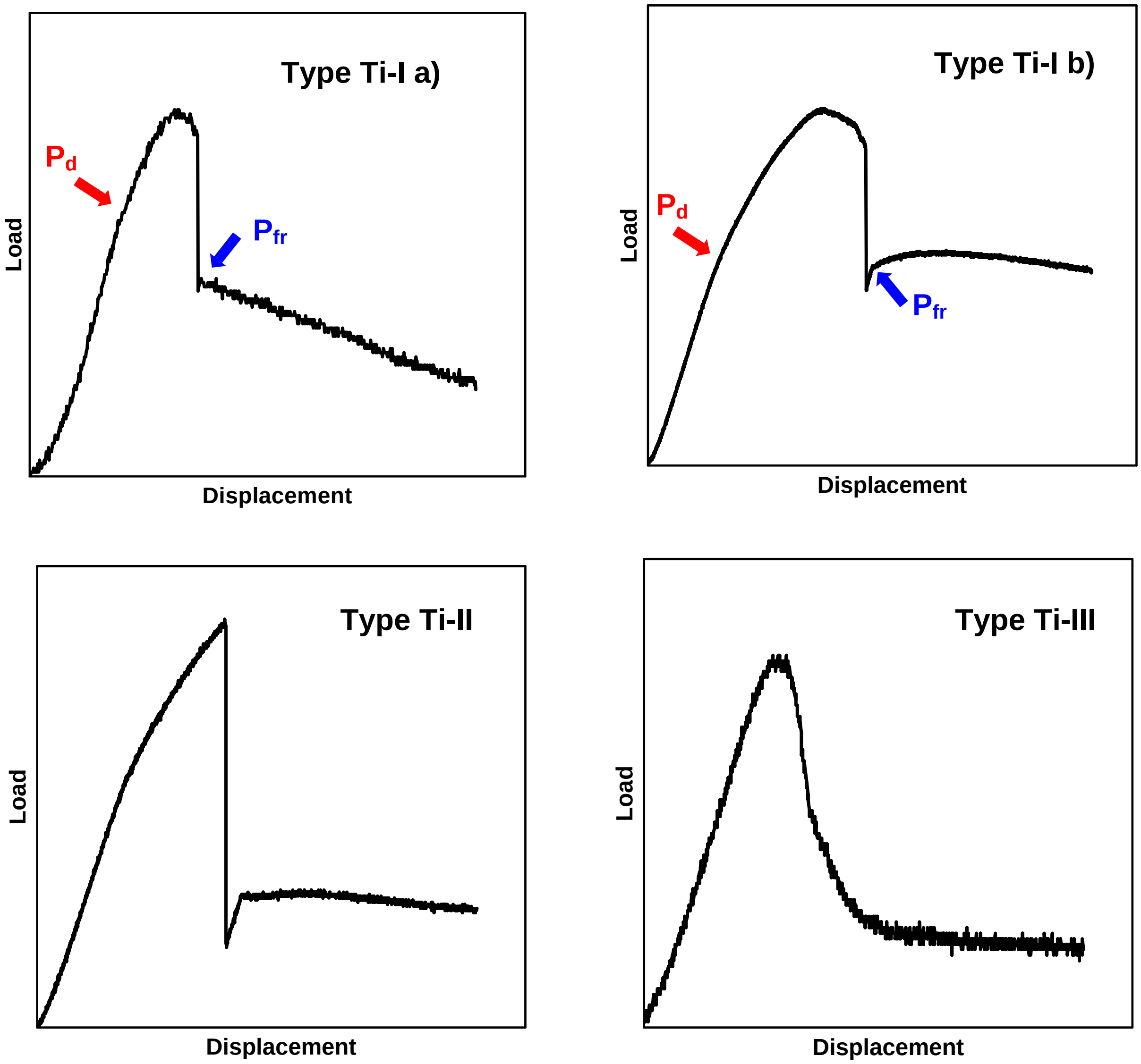

Figure 3.39. Typical load-displacement curves type for CuTiH samples

Due to the observed plastic deformation of the matrix (see below) the interfacial parameters were calculated using equations (1.23.), (1.28.).

An apparent mean value for the yielding strength τ_y of 59.38 MPa and accordingly 63.22 MPa and an interfacial frictional stress τ_{fr} of 51.66 MPa and 56.29 MPa (Fig. 3.40) were obtained for CuTiH2 and CuTiH4 composites. The average of the stress values was determined for each investigated thickness (see table 3.5.) according to formula (1.23.). An apparent mean value for the maximum strength was derived with formula (1.23.) from the average value of the maximum push-out force.

Composite	**Thickness [mm]**	τ_y **(P_d) [MPa]**	τ_a **(P_{max}) [MPa]**	τ_a **(P_{fr}) [MPa]**
CuTiH2	0.8	61.23	108.97	52.86
	1.25	57.52	105.29	50.27
CuTiH4	0.45	60.39	80.97	43.74
	0.9	66.06	121.06	68.83

Table 3.5. Averaged interfacial parameters for CuTiH composites

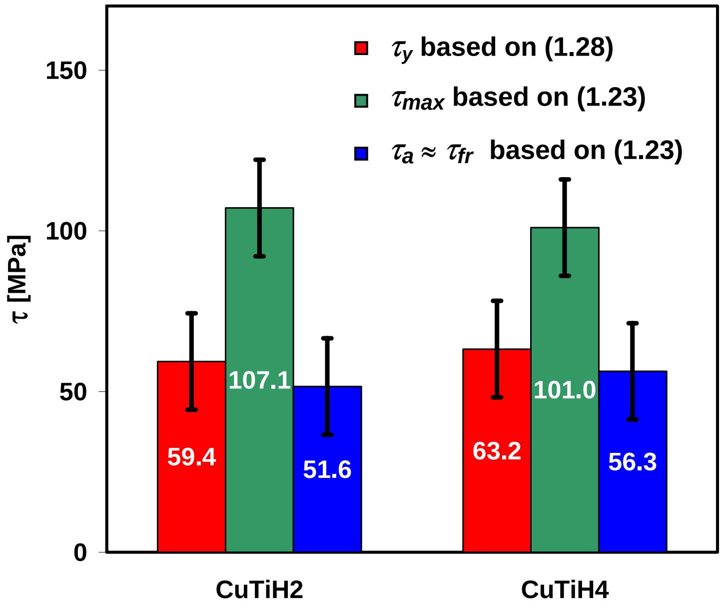

Figure 3.40. Interfacial parameters for composite with titanium interface

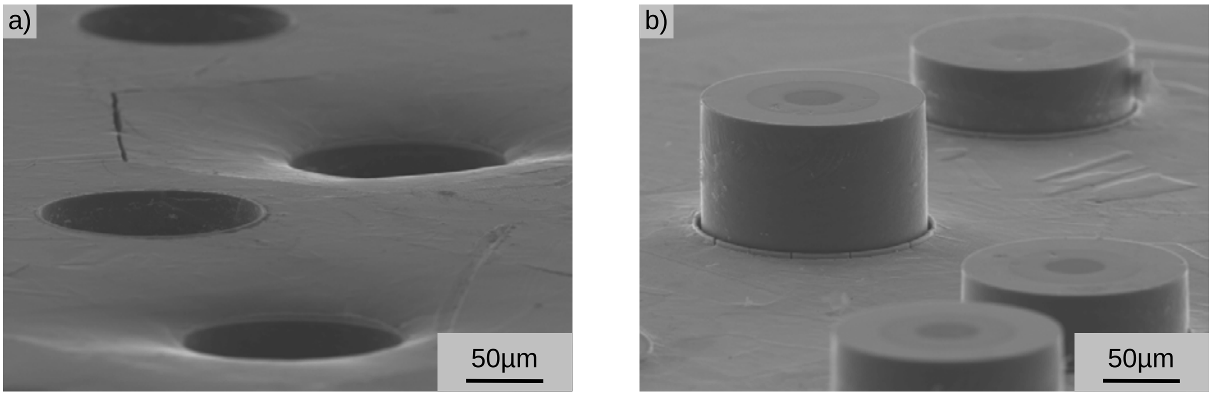

Figure 3.41. Representative SEM micrographs for CuTiH samples after push-out: a) top surface; b) bottom surface

Figures 3.41.a) and b) associate the top and the bottom surfaces of a CuTiH composite specimen after the push-out experiment. The fibre has been pressed into the matrix and pushed out of it at the bottom. Moreover, there is no trace of indenter penetration to be found on the fibre face. Plastic matrix deformation occurred clearly visible around the holes, while for some pushed fibres no deformation is observed. Matrix cracks are observed with the strong plastic deformation located at the hexagonal borderline between the copper coating of two neighboured fibres.

In figure 3.42. back-scattering electron (BSE) micrographs are presented showing the top side of the CuTiH2 composite after push-out experiments. The dark areas are characteristic for SiC and carbon, while the light zone corresponds to copper. Cracks also appear dark.

A closer look at the pushed fibres surfaces shows that the failure occurs at different fibre interfaces. For some fibres the failure occurred between the two C-rich fibre coatings (Fig. 3.43.a)). For others the crack occurred between titanium carbide and copper, with the carbide layer adhering to the matrix (Fig. 3.43.b)). Figure 3.44. put in evidence once more the different failure interface looking at the walls of the push-out holes. The fibre can be clearly seen pushed out of the matrix. In Fig. 3.44.a) the carbon coating remains on the matrix side while in Fig. 3.44.b) the failure appears between the TiC layer and the outer carbon coating. Here dislocations in the copper matrix become clearly visible as a result of the high push-out loads.

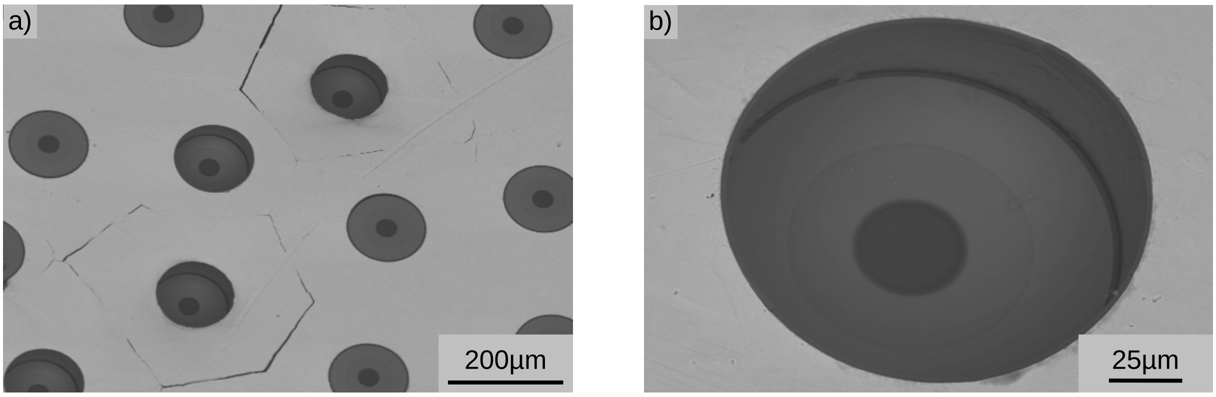

Figure 3.42. Back-scattering electron micrographs of CuTiH push-out samples a) top surface; b) magnification of a push-out hole

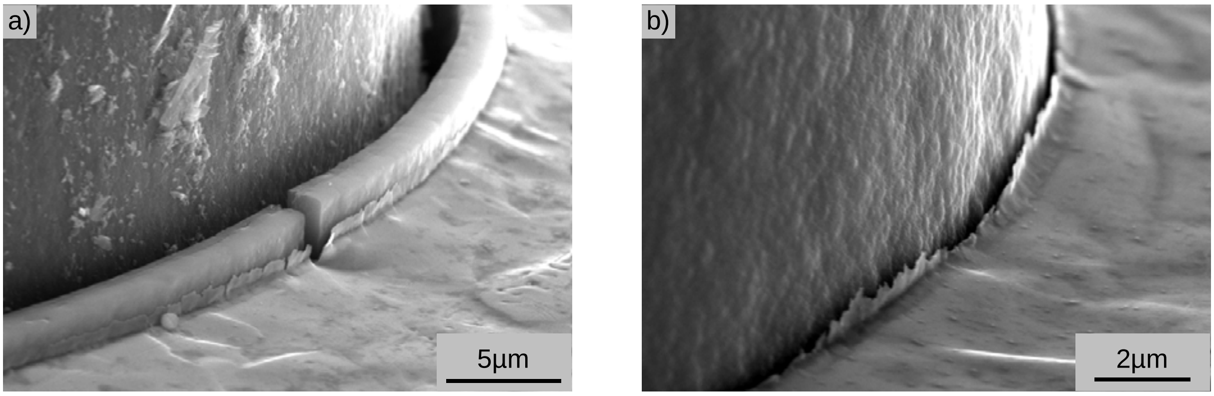

Figure 3.43. Interface failure in CuTiH samples (bottom side): a) between the two C-rich coatings of origin fibre; b) between titanium carbide and copper

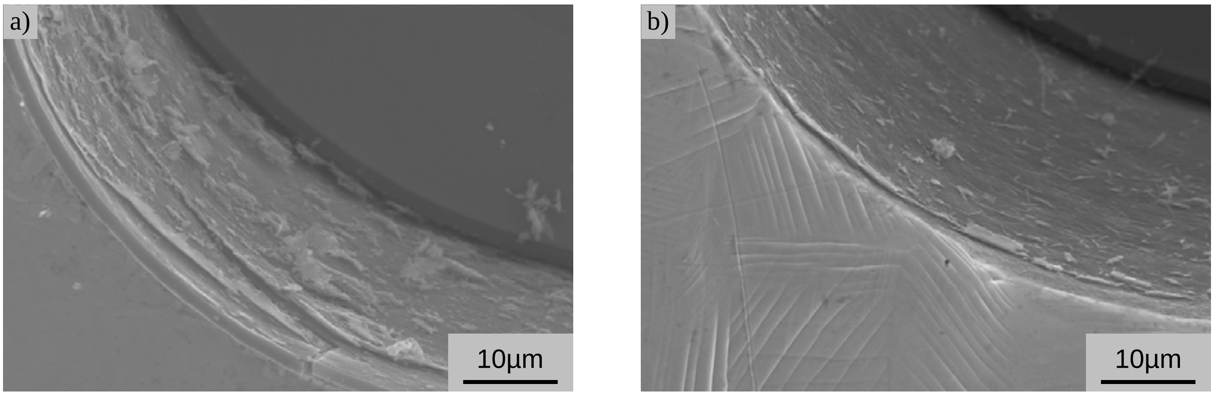

Figure 3.44. Interface failure in CuTiH samples (top side): a) between the two C-rich fibre coatings; b) between titanium carbide and carbon coating; dislocations in the copper matrix are visible

3.2.3. Tensile test

3.2.3.1. Tensile testing of the constituent materials

Electrolytic copper

Tensile specimens of electrolytic copper with rectangular cross-section of about 4 mm² and a reduced section length of 30 mm were produced. Samples with the same geometry previously heated to 550°C with a rate of 20°C/hour were also investigated. Two samples of each kind were tested. The clamping length was about 60 mm and no additional extensometer was used but the cross-head displacement. A uniform displacement of the cross-head of 1 mm/min was applied and the induced load was detected with a standard load-cell. Only elCu4 was tested with a speed of 5 mm/min.

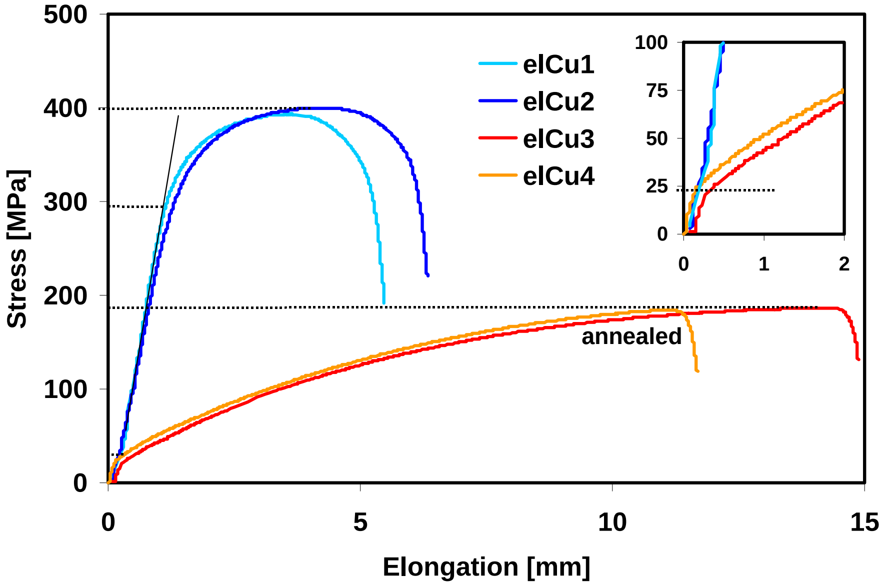

Figure 3.45. Stress-strain diagram for electrolytic copper samples

The applied stress was determined dividing the load by the original cross-sectional area of the samples. The resulting stress-displacement diagrams are shown in Fig. 3.45.

Sample	σ_y [MPa]	UTS [MPa]
elCu 1	290	394
elCu 2	275	399
elCu 3	21	186
elCu 4	25	184

Table 3.6. Tensile test results on pure electrolytic copper

While the as deposited material had shown ductile failure under a sliding angle of 45° over the whole sample width, the annealed samples showed ductile fracture behaviour necking in the width and thickness of the flat samples (Fig. 3.46.).

Values for yield strength and ultimeate tensile strength are shown in table 3.6. The Young's modulus can not be derived from this measurements due to uncertain strain determination.

The tests were kindly performed by Dipl. Ing. L. Krämer from Lehrstuhl für Leichtbau, TUM, in a standard tensile test device.

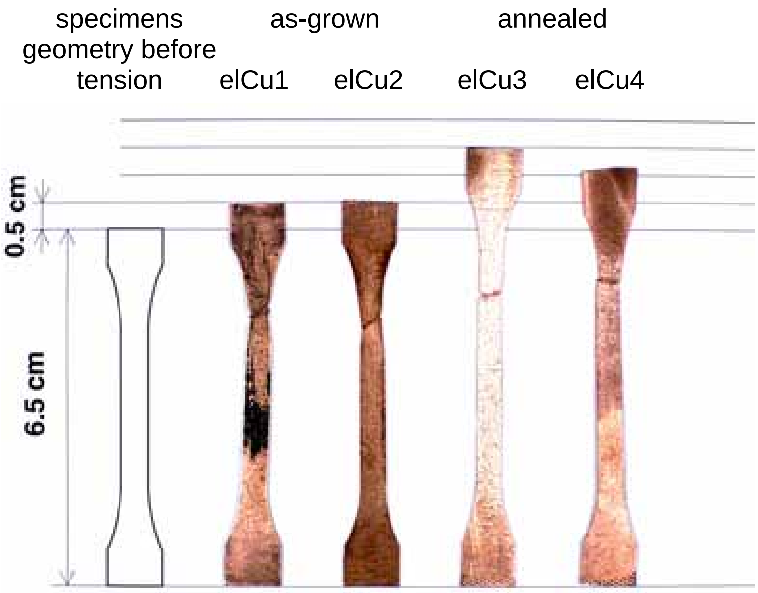

Figure 3.46. Electrolytic copper after tensile test measurements

SiC-fibre

SiC (SCS-6) fibres as provided by Textron were tensed in fibre direction in the universal test device with a nominal cross-head speed of 1 µm/s upon fracture. The fibres were clamped with plies of paper to prevent the clamping region from damage. Load and strain were measured with a standard load cell and the laser-speckle system described in chapter 2.2.4. Representative stress-strain curves are shown in Fig. 3.47.

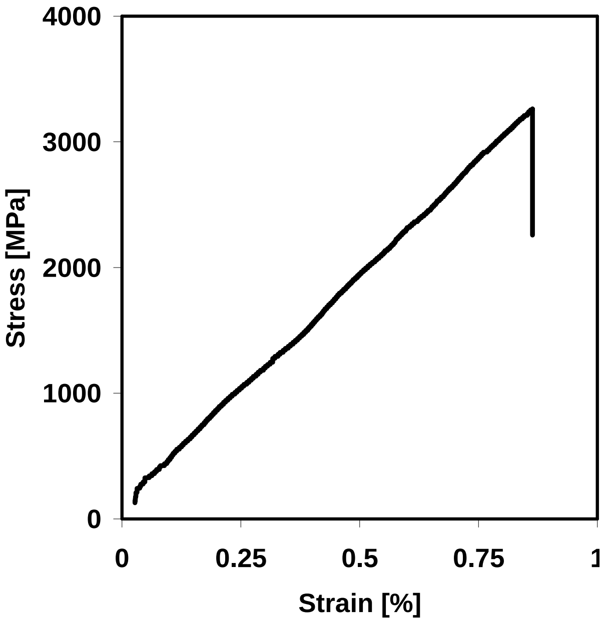

Figure 3.47. Typical stress-strain diagram for SiC fibres

The whole fibre fractured in a brittle manner and the fracture location could not be observed. Mean values of Young’s modulus, E_f, and ultimate tensile strength were calculated and are presented in table 3.7.

	E_f [GPa]	UTS [MPa]
SCS-6 fibre	351	3138

Table 3.7. Tensile test results on SiC-fibres

3.2.3.2. Tensile testing of copper coated single fibres

The copper coated single fibres with and without modified interface were especially prepared for the tensile test by additionally coating about 1.5 cm of each fibre end with a thick layer of electrolytic copper (Fig. 3.48.) to avoid damage in the gripping zone. The thickness of the protection layer was about 0.5 mm.

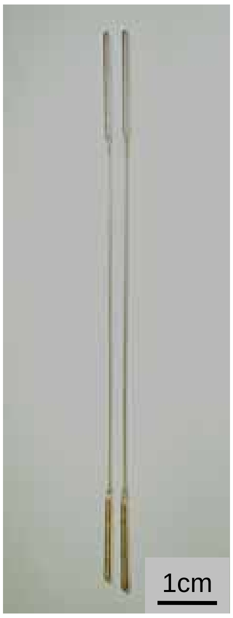

Figure 3.48. Coated fibres prepared for tensile test

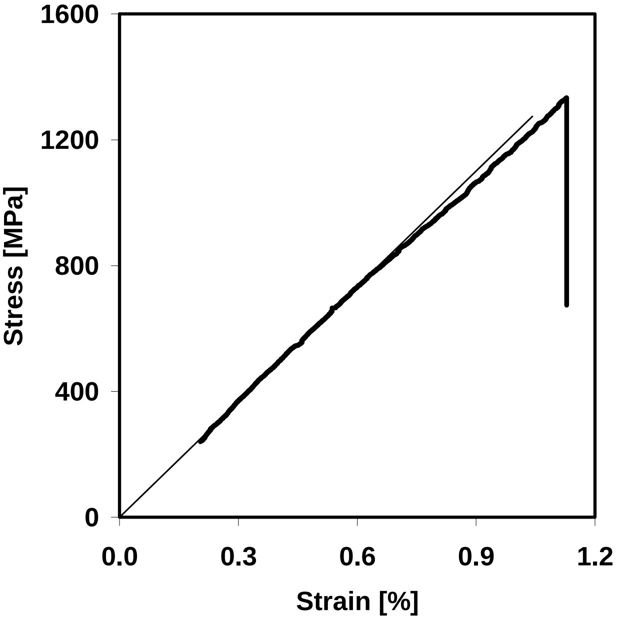

Figure 3.49. Typical stress-strain diagram for coated fibres, either with or without titanium

Coated fibres from different batches used for composite production (without, 5 min and 10 min titanium deposition time) with dfferent thickness of matrix coating were tested for comparison.
The specimens were tested in the same way as as the uncoated fibres (chapter 3.2.3.1.).

Sample	#	V_f %	Ti-coating [min]	E_{cf} [GPa]	UTS [MPa]
TSSCu08	11	37	-	126	1312
TSSCu09	8	28	-	97	920
CuTi09	10	18	5	63	621
CuTi15	6	20	10	62	713
CuTi26	10	38	10	135	1328

Table 3.8. Results on coated fibres

A mean value for the Young's modulus, E_{cf}, calculated from the slope in the lower elastic region of the measurement curve is given in table 3.8. for the different tested fibre batches, as well as the mean ultimate tensile strength.

The coated fibres often fractured next to the clamping protection**,** where the matrix coating was thinner due to a thickness gradient over the fibre length as described in chapter 3.1.1.2., while sometimes the fracture occurred randomly in other places.

3.2.3.3. Tensile testing of composites

Tensile experiments on round unidirectional composite samples were performed parallel to the reinforcement direction. For the tests the HIP-capsule described in chapter 2.1.4. was turned to approximately the radius of the reinforced zone. A thread was tapped in both sample ends for the special grips of the tensile machine. Composites without and with different titanium interface (5 min and 10 min) having diverse fibre volume fraction were tested by DLR. The strain was measured with a set-on strain sensor, the load with a standard load cell. The testing speed was 1mm/min.

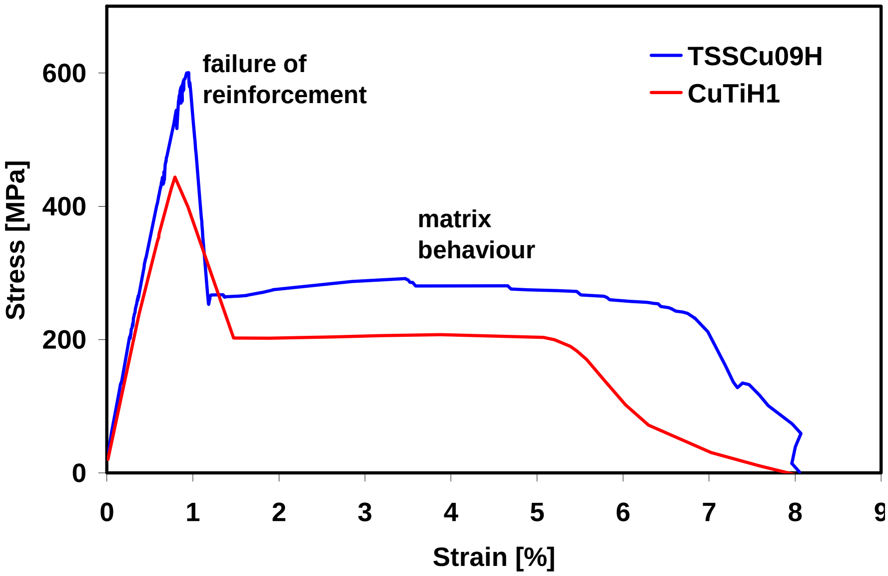

Figure 3.50. Example stress-strain curves of composite tensile test

Values of Young’s modulus and tensile strength determined from the experimental stress-strain curves (Fig. 3.50.) are shown in table 3.9. for all investigated composites. The fibre volume fractions are given, too.

Sample	**V_f [%]**	**Ti-coating [min]**	**E_c [GPa]**	**UTS [MPa]**
TSSCuH08	27	-	152	767
TSSCuH09	15	-	77	603
CuTiH1	14	5	75	446
CuTiH3	14	10	54	469
CuTiH5	32	5	133	865
CuTiH7	27	10	137	887

Table 3.9. Results from composites tensile test

Images of the composites after tensile testing are presented in Fig. 3.51. In the cases of TSSCuH08 and CuTiH7 the fibres were pulled out from the matrix.

The fracture surfaces of TSSCuH09, CuTiH1 and CuTiH5 were observed by scanning electron microscopy.

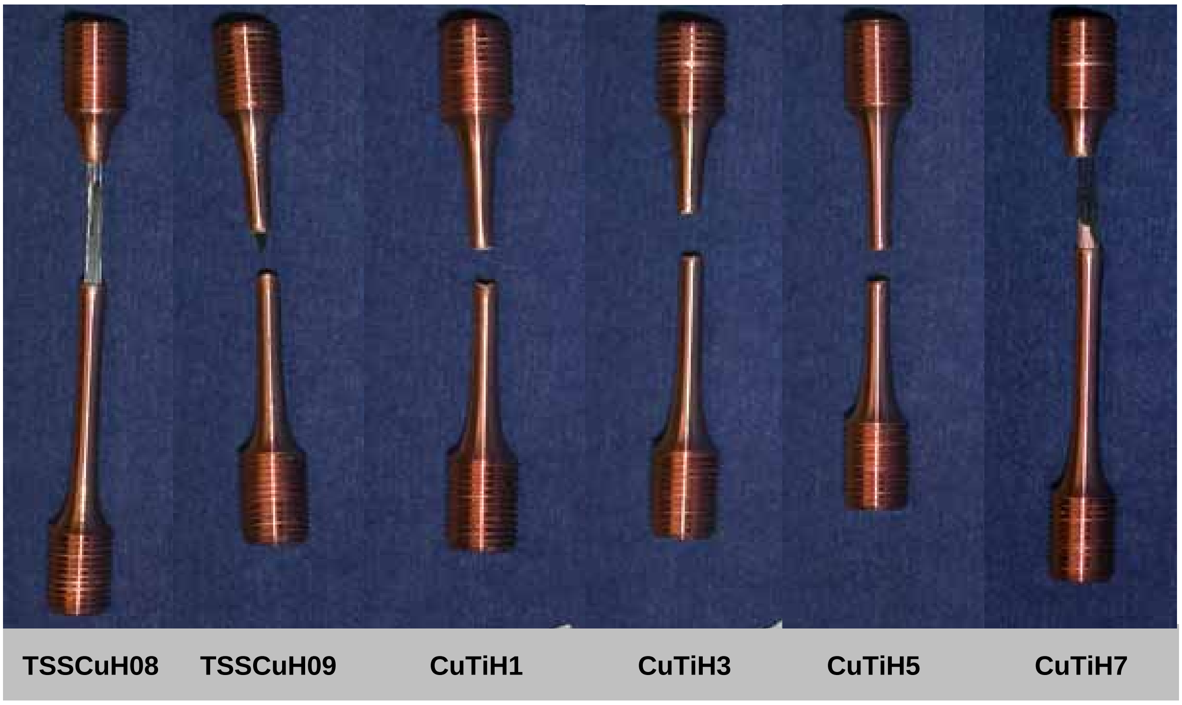

Figure 3.51. Images of composites after tensile testing

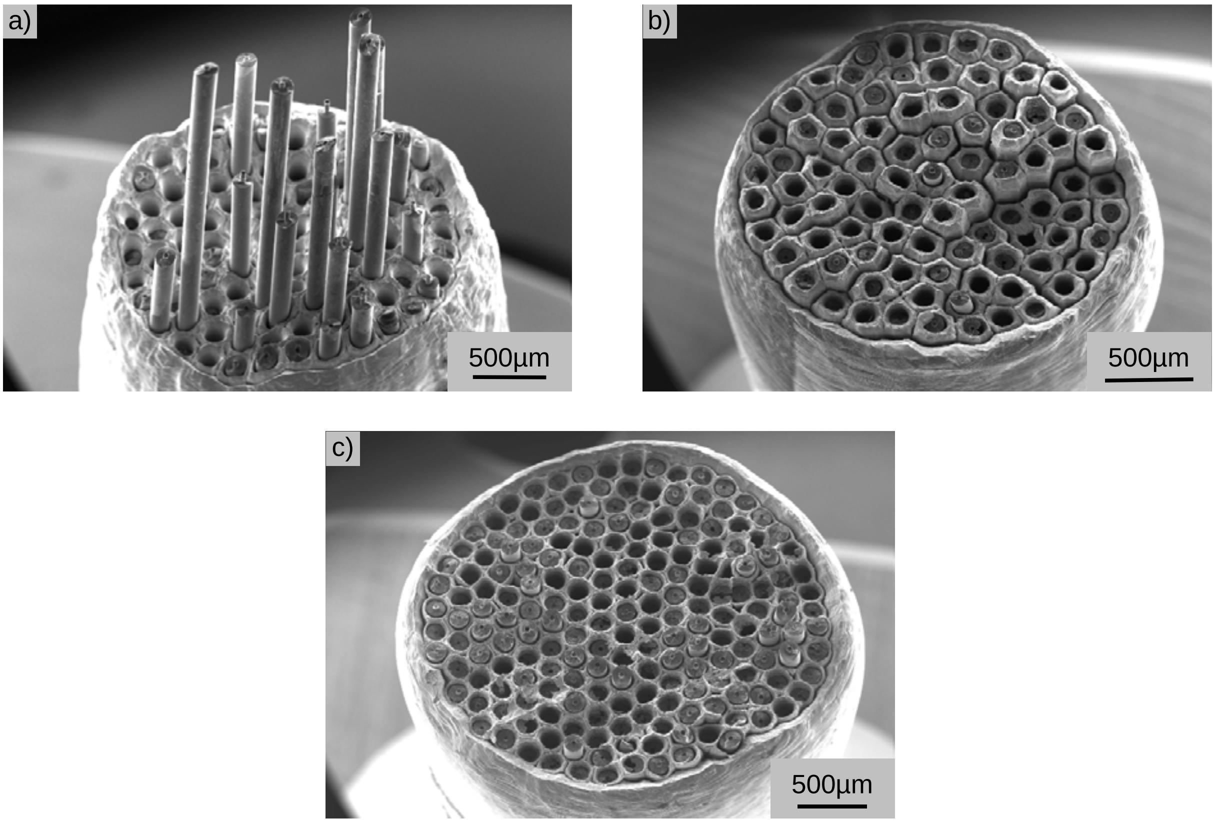

Figure 3.52. Overview fractographs of different composites a) TSSCuH09; b) CuTiH1 and c) CuTiH5

The fracture behaviour varied significantly. For composites without titanium interface, many fibres were pulled out from the matrix, while for samples with modified interface the fibres broke in the necking plane (Fig. 3.52.).

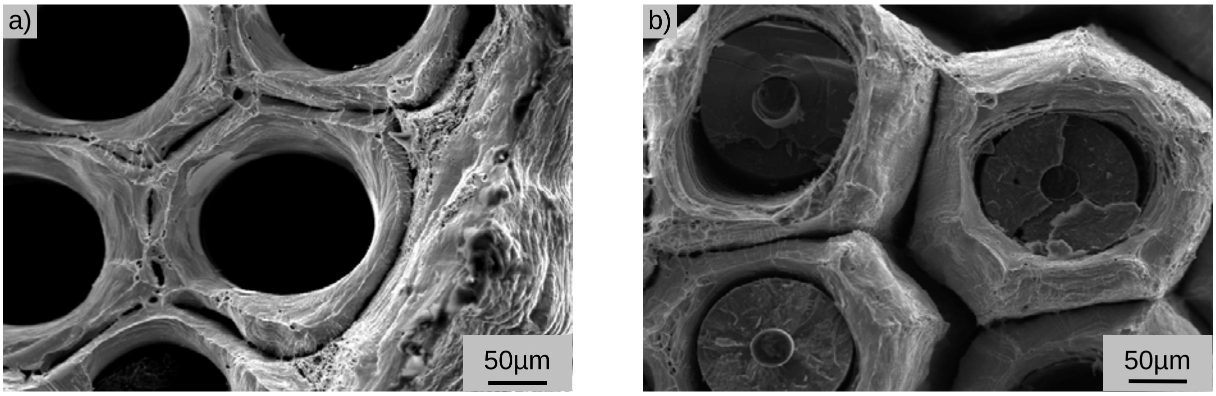

Figure 3.53. Composites fractographs showing matrix failure a) TSSCuH09 and b) CuTiH1 composites

The SEM images show that the deformation and crack damage of the ductile copper matrix for CuTiH1 with titanium interface (Fig. 3.52.b) and 3.53.b)) is stronger than that for TSSCuH09 without modified interface (Fig. 3.52.a) and 3.53.a)) or that for CuTiH5 having smaller fibre volume fraction (Fig. 3.52.c)). A necked down matrix structure was observed around the fibres with dimples where pores had formed. The boundaries of the original individual copper coated single fibres debond, leading to pore formation and sometimes big gaps appear.

For all composites the SiC fibres showed brittle failure behaviour. Fig. 3.54.a)-c) show SEM failure images of the copper matrix and the SiC fibre for different composites.

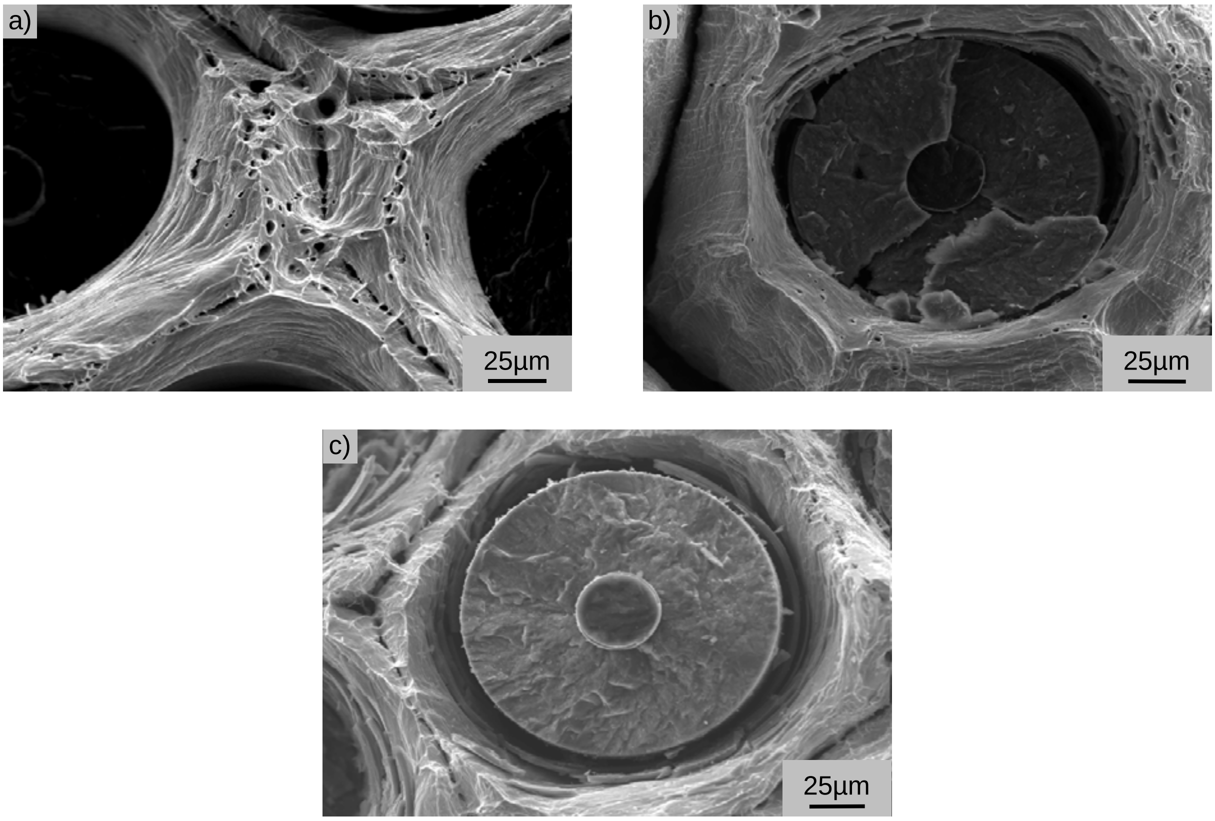

Figure 3.54. Magnified fractographs showing matrix failure of different composites a) TSSCuH09; b) CuTiH1 and c) CuTiH5

It is found that the fibre coating carbon layer has been fully peeled off in composites with titanium carbide interface (Fig. 3.55.b)) while for composites without titanium it is pulled out together with the SiC fibre (Fig. 3.55.a)).

In the materials contrast of the BSE images this is once more clearly visible. For composites with titanium interface, fragments of the fibre coating layer were found on the Cu-matrix wall (Fig. 3.56.b)) while for TSSCuH specimens the coating layer remained on the broken fibre (Fig. 3.56.a)).

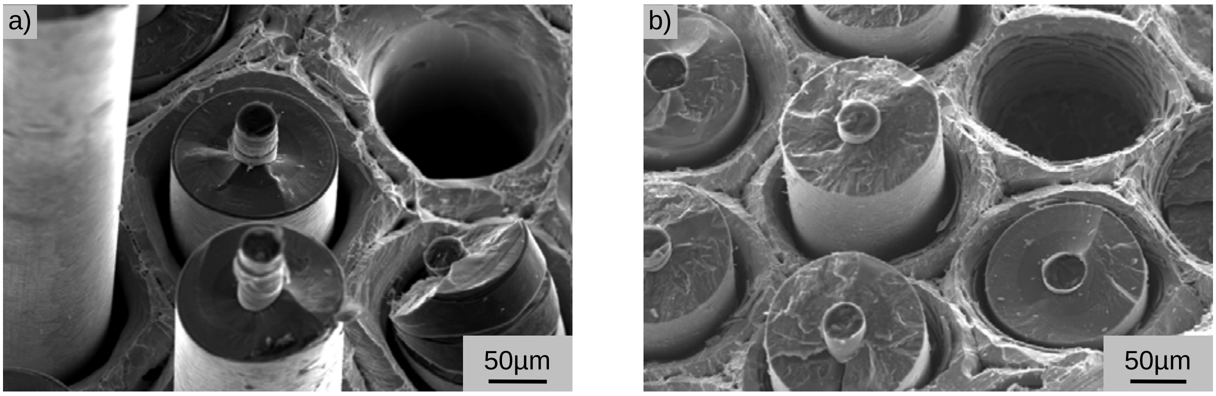

Figure 3.55. SEM fractographs showing fibre failure a) TSSCuH09 and b) CuTiH5 composite

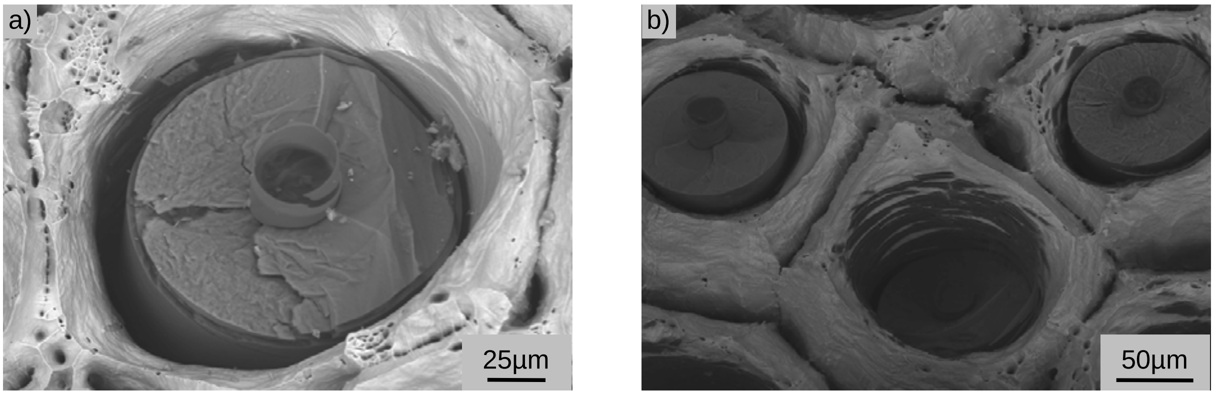

Figure 3.56. BSE fractographs showing the interface failure a) TSSCuH09 and b) CuTiH1 composite

4. Discussion

4.1. Morphology and microstructure

Magnetron sputtering

For coating flat samples by means of magnetron sputtering a laterally homogeneous deposition rate can be obtained by using a device designed for this purpose (Chapter 3.1.1.1.). The result for fibres positioned vertically in the chamber looks different (Fig. 3.4.). An explanation considering the geometry of the arrangement has been found. The sputter-cathode is located sidewise above the rotating deposition frame (Figure 2.5.). During rotation the upper edges come close to the source, resulting in a thicker coating. For the same reason, a smaller flow of deposition material reaches the lower edges. The fibres in the middle are coated more homogeneous, but receive a thicker coating at the top.

The differences in the coating thickness are very significant. They exceed a factor of two between the two locations. The measurements were carried out for a deposition time of 10 minutes. The same distribution can be expected for 5 minutes, and the coating thickness ranges overlap.

As these measurements were carried out afterwards, all fibres from one deposition procedure were processed together and bundled in one composite, resulting in a non uniformity of the interface thickness.

Electroplating

Electrolytic deposition was chosen as the processing technique for the matrix of the composites manufactured and analysed in this thesis.

Initially copper was deposited on the SiC fibres at various electric potentials between cathode and anode in order to find optimal deposition parameters. On the one hand, it is known that the deposition rate increases with applied voltage [125], while on the other hand, a too high voltage can lead to the formation of hydrogen-blisters and the deposited layer looses quality [116]. The voltage resulting in a sufficient quality and deposition rate was 0.8 V. Although, 0.6 V was found to be satisfactory and some specimens deposited at this voltage were investigated.

It is also known, that the microstructure of the electroplated layer depends on the microstructure of the substrate. Electroplating of copper shows epitaxial growth behaviour [125]. It was further found, in this study, that after a thin microcrystalline layer the copper grows in larger, radially oriented needle-crystals. It is known that the grain size is influenced by the current density [125]. Due to the layer growth on the fibres the surface growth rapidly, thus decreasing the current density.

Sometimes the radially oriented microstructure was found to be interrupted by larger grains (Fig 3.5. a) and b)). The long and thin crystals have a high surface to volume ratio. The system will attempt to adopt a configuration where the free energy is minimised, typically by forming rounder grains.

Measurements of the copper layer thickness show differences of a factor of two along the length of the fibre. The density of the electric field varies along the fibre due to resistivity, changing thickness and contacting. These lead to a non-uniform coating.

The purity of the electroplated copper is reported to be 99.9 % [115]. Other elements present in the electrolytic bath are co-deposited during the process. SEM investigation of the copper matrix and EDX-spectroscopy show impurities containing sulphur, but their amount was negligible. Oxygen and hydrogen are also co-deposited. Reacting to H_2O at temperatures

higher than 400°C it has an undesired influence on the properties of the composite [116]. The pores formed by the vapour pressure of the water disturb the thermal conductivity.
The formation of pores is especially visible in the first processed composite (TestH3) at the boundaries of the original copper coating (Fig. 3.11.). The fibres were taken out of the electrolyte during the deposition process for optical examination. Additional atmospheric oxygen explains the abundance of pores.

Reduction of porosity

The copper coating contains hydrogen and oxygen as an unavoidable consequence of the electrolytic processing. Hydrogen and oxygen are found to form H_2O at temperatures higher than 400°C [116] as mentioned above. The vapour pressure of the water produces microcavities. As a result many pores located at the grain boundaries were found by optical microscopy (Fig. 3.9.). The hydrogen has to diffuse out of the electrolytically deposited copper at a temperature below 400°C to avoid this so called ”hydrogen disease”.

The investigations with a mass spectrometer (Chapter 3.1.3.2.) show a significant increase of the hydrogen signal at a temperature of 250°C. This is in agreement with values reported in the literature [116]. At this temperature the hydrogen desorption from the surface starts. The three measurement curves show a small shift in temperature. This can be attributed to the samples contact with the subjacent heater and thermocouple. Measuring the nominal temperature at the heater, the sample might still have a lower temperature. Even for measurement #2b where the sample was not moved there can be a change in thermal contact due to sample deformation by the thermal stresses induced during heating and cooling. This assumption is confirmed by accompanying temperature measurements with a pyrometer on the sample surface. The hydrogen is not chemically bonded or trapped in defects, as defects anneal at lower temperatures.
As the temperature rises, a change of slope occurs around 370°C. At this temperature, the outgasing is limited by the maximum diffusivity and desorption from the sample surface. At temperatures near 600°C the hydrogen signal significantly decreases implying that there is no more hydrogen left to diffuse out. The shift in temperature between the outgasing behaviour at higher temperature in measurement #1 and #2b corroborates the belief that it appears due to different heater contact (especially because it is now smaller) that can be explained with higher heat radiation at elevated temperatures.

Peaks found at different temperatures can be assigned to contaminates on the sample surface, especially acetone from prior sample cleaning, which was confirmed by the same measurement procedure but not further explained in this work.

To process electrolytically coated fibres with reduced porosity fibre samples were heated with different heating rates to various high temperatures while always applying a dwell time of one hour at 300°C allowing the hydrogen to diffuse out. Two times less pores were found after the slow heat treatment (0.5 K/min) because the samples had been a longer time (about six hours) exposed to temperatures above 250°C before reaching the critical temperature of water formation at 400°C, thus the hydrogen content in the samples was much stronger reduced (Fig. 3.9.a.).
For processing of a larger number of fibres an even slower rate was applied (table 2.5. (treatment 3)). With about seven hours in the degasing temperature range no more pores are visible, although the 400°C critical temperature was exceeded.

As for the different annealing temperatures (550°C, 650°C and 750°C) no change in the porosity was observed, the fibres were only preheated to 550°C before HIPing to a composite.

4.2. Mechanical properties

4.2.1. Hardness

Microhardness investigations on copper single crystal using the NanoTest device described in chapter 2.2.3. have shown that at low testing loads the hardness measured varies dramatically. A plot of the estimated hardness as a function of the plastic indentation depth reached at a certain applied load is shown in Fig. 3.25. The graph shows the hardness values decreasing from a maximum for low forces to a uniform value calculated for measurements reaching a certain indentation depth. This phenomenon is reported in literature also for other materials [126]. In this study, it was found for the copper single crystal that the hardness decrease is amortised for loads greater 75 mN, which corresponds to a plastic indentation depth of about 1600 nm. These results are in agreement with the literature values reported in [127].

The higher hardness values registered at lower testing loads can have two causes: one is the so-called ”indentation size effect”, the second can be work hardening in the surface region. Indentation size effect implies that for the same material the hardness value depends on the size of the indentation and hence on the load used. Thus when a lower indentation load is used a higher hardness value is obtained. At lower loads a smaller volume of material is stressed. This volume might be effectively free from crystal defects. Additionally, during sample preparation the surface was work hardened due to the mechanical polishing procedure. These two effects superimpose to produce the higher hardness profile at lower loading stages.

To avoid a hardness dependence of the indentation-force, according to the results in single copper crystal, a 100 mN load was chosen for the measurements performed in this work. With this load an indentation-depth of 2000 nm was reached.

For indentations at higher loads a pile-up of the copper matrix was observed, leading to geometric uncertainties, so that a higher load was not used.

Microhardness indentations on the electrolytic copper layer of coated SiC-fibres, annealed at 550°C, did not show a systematic change in the matrix hardness with the distance from the fibre. The results are in agreement with the transmission electron microscopy investigations (see chapter 3.1.6.) which had shown no reaction zone between fibre and matrix in composites with or without titanium-precoating of the fibre.

Pickard and Miracle reported an increase in the titanium matrix microhardness for Ti/SiC composite from 1.2 GPa at 60 µm of the fibres up to 2 GPa near the fibre surface. This result was correlated to carbon diffusion from the coating into the matrix [128]. In contrast Gonzales [129] reported no change in the titanium matrix microhardness with the distance to the fibres in similar composites. This was attributed to the presence of a continuous TiC reaction layer of about 1 µm in thickness at the C/matrix interface. This TiC layer acted as an effective diffusion barrier which impeded the diffusion of C in the matrix.

The copper microhardness and Young’s modulus in composites were compared with that of as grown and annealed copper coatings.

The modification of the Cu-matrix microhardness by annealing is shown in Fig. 3.30. The microhardness dropped noticeably by annealing the copper coated fibers. This drop is caused by relieving of internal stress. As the annealing temperature is higher than the recrystallisation temperature, the microhardness decrease was caused by grain growth and reduction of dislocation density. In the case of as-processed copper, grain size, dislocation density and internal stress all contribute to the measured microhardness [130]. In comparison to thermally annealed copper where only the grain size made a major contribution to the microhardness.

The hardness values measured in the as-deposited layer of the titanium and copper precoated fibres were closer to the results of the annealed coated fibres. This can be explained by the observation of a larger as-grown grain size due to the base-orientated growth behaviour of the copper grains during electroplating.

No significant difference was found in the microhardness between the annealed fibres and the corresponding composites, indicating that the fibres were already fully annealed during the heat treatment process.

The elastic modulus values varied randomly between 75-190 GPa for as-deposited electrolytic copper, 90-150 GPa for the copper coating on the annealed fibres and 120-190 GPa for consolidated composites. The average value of elastic modulus of polycrystalline copper at room temperature is reported to be 128 GPa. This value averages the different values reported for the high-symmetry crystal directions: 66.6 GPa along <100>, 130.3 along <110> and 191.1 along <111> [131]. The random variation of the measured values can be caused by crystallographic texture in the copper layer.

The composites matrix Young's modulus is found to be higher in comparison to the copper coatings Young's modulus of the annealed fibres. During annealing and cooling the copper and the fibre having different coefficients of thermal expansion expand and contract differently, which leads to thermal stress. These induced stresses can be the cause of the higher elastic modulus of the composite compared with single coated fibres.

4.2.2. Push-out measurements

4.2.2.1. Composites without Ti-interface

The first processed composite (TestH3) showed high porosity in the copper matrix especially at every single-coated fibre boundary as discussed in chapter 4.1. Nevertheless it was used for the first push-out measurements with the micro head of the NanoTest device.

Displacement-controlled measurements with the push-out setup of the universal testing device have been carried out on a composite with enhanced matrix, TSSCuH07. These measurements showed the course of the push-out curve as described by various authors.

From both types of results values for the initial debonding load P_d were received. This allowed the evaluation with the appropriate regression function (1.26.). Both composites have very similar debonding forces. The calculated debonding strength shows that no influence of the porosity on the interfacial parameters in TestH3 can be seen. A debonding shear strength of about 5 MPa is a consequence of the poor adhesion. As there is no chemical bonding between the untreated SiC-fibres and the copper, only the thermal compressive stress due to the CTE mismatch between fibre and matrix has to be considered.

The post-experimental examinations of the push-out specimens carried out by means of scanning electron microscopy confirmed the lack of chemical interaction between the fibre and the copper. No copper traces were found on the surface of the pushed-out fibre and no fragments of the carbon layer remained on the copper side. Vertical brush marks indicate the fibre sliding process.

The calculation of the interfacial friction stress with the formulas derived from the shear lag model (Chapter 1.3.5.) indeed show a significant difference, especially as the 5.87 MPa friction stress τ_f for TestH3 appears to be higher than its debonding strength τ_d of 5.00 MPa, while for TSSCuH07 the friction stress τ_f is only 3.40 MPa. The most plausible explanation is that the considered maximum load of the load-controlled experiment is not the required frictional load. This can certainly be less than the maximum, as can be seen in the curves obtained from measurements with the universal testing device (Fig. 3.34., Type I).

Noticeable in the TSSCuH07 push-out measurements is the snatchy curve referred to as Type III (Fig. 3.34.). Such behaviour was also found by Rausch et al. [89] for thick samples of aluminosilicate glass matrix. This behaviour indicates that the stiffness of the copper matrix for the range of the measured forces is high enough to allow the application of the Greszczuk model developed for ceramic matrix composites. Type I (attributed to thin samples) was as well found by Rausch and was found in this work when considering thinner samples. Types I and II were also reported by Bright et al. [82], using the same model for evaluation.

4.2.2.2. Composites with Ti-interface

Composites with an improved titanium interface required high push-out forces. They were tested in the universal testing machine. Diverse types of push-out curves were found, they were different from the curves obtained for the composites without a titanium carbide interface layer. Because the maximum load between each type of curve (Ti-I, Ti-II, Ti-III) differs consistently for the same tested composite specimen, the types are no longer correlated with the thicknesses of the investigated samples but with the different crack-behaviour. By SEM investigations different interfaces were found to be the location of failure. At times the bonding between titanium carbide and the carbon layer failed, while sometimes the interface between the two carbon layers (Chapter 2.1.1.) broke down (Fig. 3.44.). No crack failure at the matrix/TiC boundary was detected. In addition the titanium carbide layer always remained on the copper.

The same interface debonding behaviour was reported by Guichet et al in SCS-6/Ti-alloy composite [132]. Their detailed experimental and theoretical investigations illustrated that the push-out failure propagation was sensitive to the residual stress occurring due to processing. Different residual stress appears with different fibre volume fraction. The radial stress makes either the crack initiate in the carbon coating at the bottom face of the sample, propagating over the complete fibre length, or leads to a sudden crack propagation between the coating and the reaction zone. Similar experimental observations are reported by Gundel and Wawner, also for SiC/Ti composite [133].

By TEM investigations the sputtered titanium layer was in some cases detected to be broken before full carbidisation occurred, resulting in an imperfect interface. This might be the reason for some very weak bonding associated with curve type Ti-III (Fig. 3.39.).

In the push-out experiments resulting in high forces (type Ti-I), a significant plastic flow of the matrix was observed. The plastic deformation created dislocations (Fig. 3.44.b.) until the stress conditions for sudden debonding were reached. At the hexagonal boundary (See 3.1.4.) local failure in the matrix occurred (Fig. 3.41. and 3.42.).

Only the push-out experiments associated with type Ti-I were analysed mathematically, as they were the most frequent. With the matrix showing plastic deformation, the shear-lag model is no more valid. For an estimation of the debonding strength the formula for the elastoplastic case (1.28.) was selected. The interfacial friction stress can be approximated by formula (1.23.).

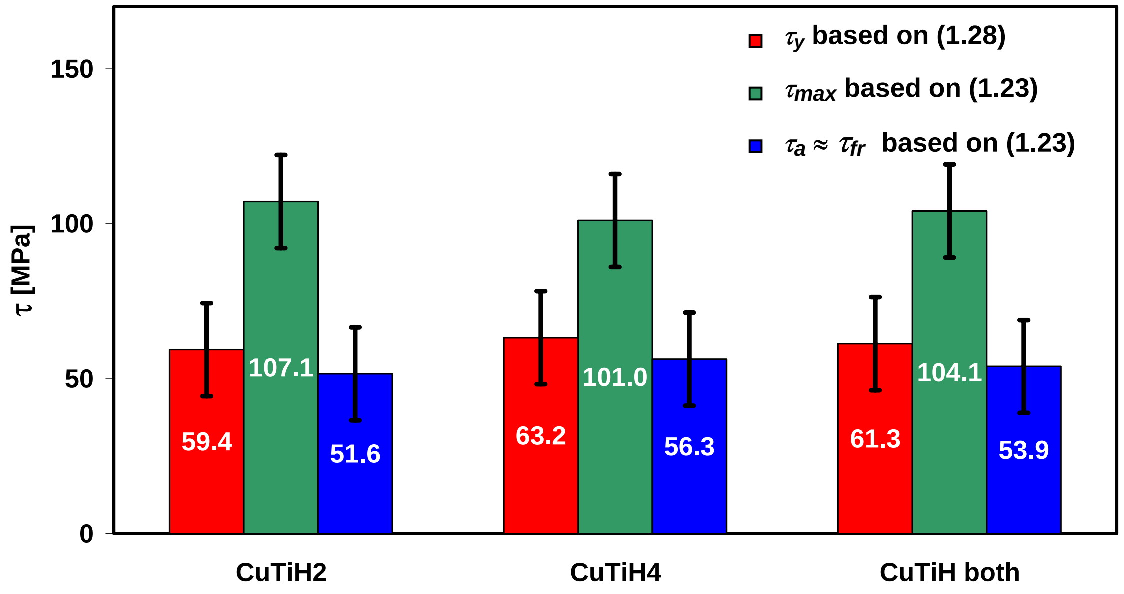

Figure 4.1. Interfacial parameters for composite with titanium interface

No significant differences between the calculated stresses in CuTiH2 and CuTiH4 composites at all thicknesses were found, although it must be assumed that strong differences in the titanium coating thickness even within the same composite sample exist (see chapter 3.1.1.2). In addition, because the two composites have about the same volume fraction (15% and 17%) the measurements can be evaluated together; this results in mean values with better statistics. 61.3 MPa averaged for the yielding strength τ_y and 53.9 MPa for the average of the apparent mean values τ_a for the frictional stress (Fig. 4.1.).

Averaging the calculated apparent mean values for each thickness a maximum shear strength of 104.1 Mpa at maximum load is obtained, which is of the same order of magnitude as Hemptenmacher et al. give from their investigations on SCS-6 fibre in titanium-alloy matrix [135, 136]. This indicates similar interface properties, as can be expected. The bonding between the titanium carbide and the copper is much stronger, confirming a small solubility of copper in the carbide, as described in chapter 1.3.4.

4.2.3. Tensile test

Electrolytic copper

Strain values are not given in Fig. 3.45., nor is the Young's modulus calculated because no extensometer was used for the tests performed on pure electrolytic copper. The determination of strain will have the largest influence on the results. The machine stiffness and the quality of clamping also influence the measurement.

The yield strength of as-grown electrolytic copper is similar to the reported values for cold worked copper [120], corresponding to the fine-grained structure and indicating crystal defects due to electrolytic growth.

For the annealed samples the yield strength is drastically reduced and in the literature yielding is reported to start instantaneously [138]. In any case yielding already starts at strain values below one percent.

The values for the ultimate tensile strength are within the expected ranges. About 400 MPa for the untreated samples which is relatively high compared to common copper values [120], while 180 MPa for the annealed copper is comparable to literature values [120].

SiC-fibre

The SCS-6 fibre properties have been verified using the laser speckle interferometer described in chapter 2.2.4.. The Young's modulus was found to vary between 330 GPa and 400 GPa with a mean value of 351 GPa, not fully reaching the specified value of 380 GPa. Some of the tested fibres have shown higher values. The strain measurement with the laser-interferometer is very accurate, with deviations from the true value smaller than 5 µm at a measurement length of 15 mm.

Also the mean ultimate strength of 3138 MPa is nearly the predicted value of 3450 MPa. In this case, clamping is responsible for the lower value, especially if the fractured surface is not investigated.

Copper coated single fibres

To be discussed is the point of fracture of the copper coated fibres. Investigations of the uniformity of the copper coating thickness in chapter 3.1.2. have shown that generally a gradient of thickness over the fibre length is found. This is the reason why most of the fibres broke next to the gripping region, but some of the fibres broke elsewhere. This might be due to previous surface damage by handling.

The deviation from linearity indicated in the example stress-strain graph (Fig. 3.49.) was not always recognisable, therefore; no value is given for this yielding. When observable, the associated strain was below one percent, corresponding to the yielding found for annealed electrolytic copper.

For the examined batches a strong correlation of the measured values with the fibre volume fraction was observed, but there was no influence of the titanium carbide interface (see below).

Composites

The tensile tests on HIP'ed composite samples showed various results.

Mainly for composites with weak interface broken fibres were pulled out of the matrix. The behaviour is similar to a loose fibre bundle where the fracture will occur independently for each fibre at its weakest point. In the case of the improved interface composites, failure in one plane was observed demonstrating the function of the improved fibre-matrix bonding. There a crack in one fibre becomes the weak point for the whole composite.

Another behaviour that was found after push-out investigations (chapter 3.2.2.) is the breakage of the fibre matrix interface. For the unmodified interface, the carbon layer remained on the fibre surface while for the reactive interlayer the weaker interface was between SiC and carbon coating. The transverse contraction of the matrix material resulted in perpendicular tensile stress on the fibre-matrix bonding, showing the sensitivity of the SCS-6 fibre to radial tensile forces. These forces were increasing with the copper-matrix volume fraction, because the thicker the material the greater is the absolute transversal contraction. As a result, the hexagonal interface around the former copper coatings was split, stronger for the samples with lower fibre volume fraction. This was observed after push-out tests (Figure 3.42.). In figure 3.52.b) the copper coating of some fibres seems to be pulled out of the composite, giving rise to the description of a loose coated-fibre bundle.

The two samples that failed in the gripping zone (TSSCuH08 and CuTiH7) are conspicuous. Their fibre-matrix interface must have been affected by some forces, as bad clamping alone cannot explain these results. It is possible that resulting from the different coefficients of thermal expansion there is a lower stress in the middle of the sample length and high stress at both ends. The stress is dependant on the sample length (Described for relatively short push-out samples in [118]). This stress might have pre-damaged the samples.

Comparison

Figure 4.2. shows in comparison the tensile behaviour of the different investigated samples in a representation analogue to figure 1.13. Matrix yielding can not clearly be seen, but it is known to be less than one percent. The results for annealed electrolytic copper have high uncertainties in strain.

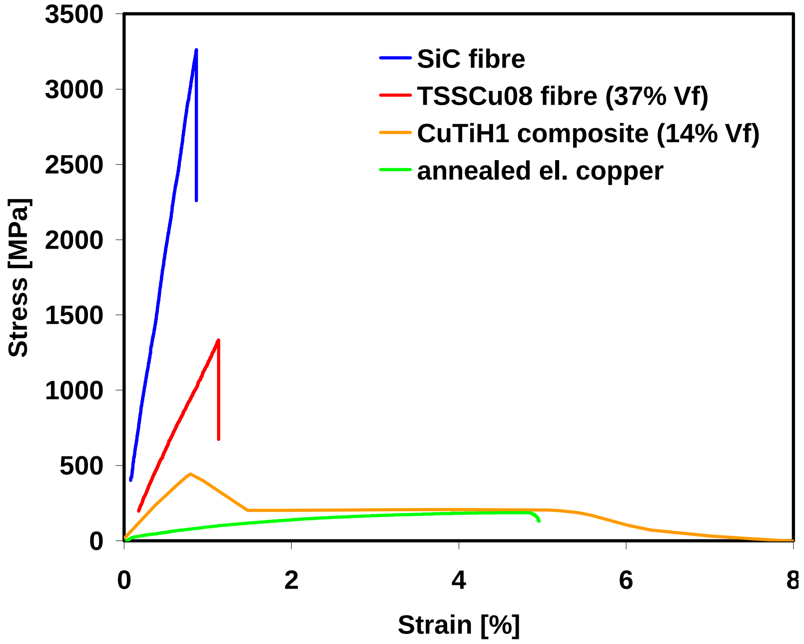

Figure 4.2. Comparison of stress strain behaviour

Figure 4.3. displays the measured composites properties (Young's modulus and ultimate tensile strength) next to the properties of the respective fibre. Although no fibre volume fraction is cancelled out, good parallelism between consolidated composite and raw material is found. The ultimate tensile strength for the composite is always lower due to a smaller effective fibre volume fraction. The Young's modulus is once higher, once lower, but always of the same order.

A better comparison of the results is produced by displaying the values dependant of the fibre volume fraction as done in figure 4.4. a) and b). The black line in both figures is a linear fit of values for composites and coated fibres, but the pure SCS-6 fibre fits these curves too. This linear correlation is described by the *”rule of mixture”*.
Assuming the validity of the *”rule of mixture”* for the Young’s modulus, the value of the electrolytic copper must be very low. Most probably there is an insufficient fibre/matrix coupling. The elastic modulus of the coated fibres is always a bit below the curve, while for the composites it is a bit higher. The difference is that the composites are surrounded by an additional copper layer from the HIP-capsule, lowering their volume fraction but increasing their strength. The capsule material is different than the annealed electrolytic copper.
For the ultimate tensile strength the interrelation is quite similar. In the *”rule of mixture”* of the ultimate tensile strength the matrix stress at fibre failure has to be considered (about one percent of strain) very low, fitting to the near zero value indicated by the regression line (figure 4.4.b)).

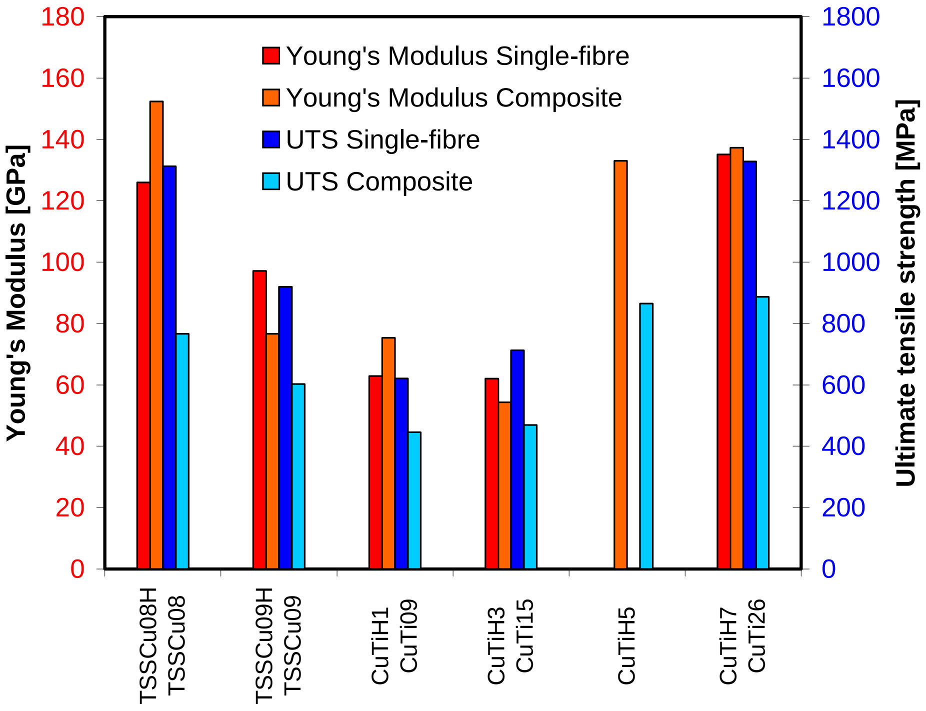

Figure 4.3. Comparison of composite and corresponding fibre

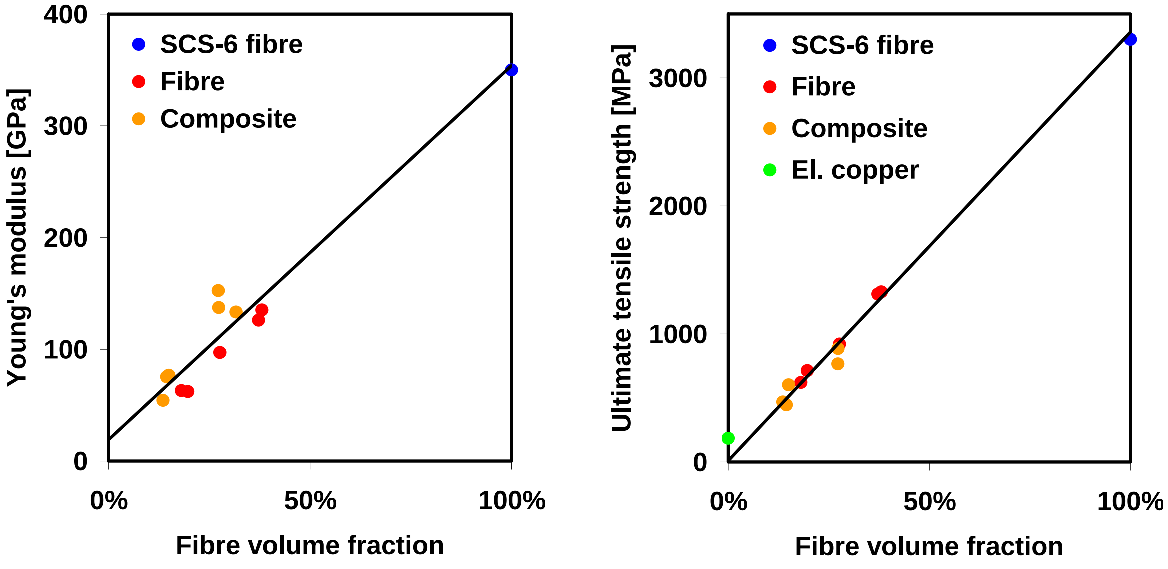

Figure 4.4. Material property versus fibre volume fraction a) Young's modulus; b) Ultimate tensile strength

The weak electrolytic copper might be an explanation for why no strengthening effect by the titanium carbide interface is observed. The immediate yielding of the highly annealed copper impedes a supporting influence to the composite strength.

The determination of Young’s modulus by tensile tests should be interpreted with caution. The results seem to match, but future measurements of higher accuracy need to be performed to confirm the observations.

4.2.4. Comparison between different measurement techniques

Yield stress

Big differences were found for the yield stress of the matrix material. The tensile test on annealed electrolytic copper resulted in 20-25 MPa yield stress, while from the push-out results 60 MPa were calculated with formula (1.28).

An explanation seems quite obvious. The formula considers uniform stress in the matrix along the fibre surface length. J. Dinter et al. [118] performed FEM simulations of the stress distributions on Ti/SiC-MMCs during push-out tests. The results showed that the shear stress varies significantly along the fibre's length. While the compressed fibre causes high stress near the loaded surface, the stress is lower and more even along the main fibre length. This principle stress distribution is comparable for other SiC-MMCs.

In a push-out test a deviation from the linear force-displacement curve can only be found when the whole fibre starts to move. Therefore the matrix material all along the fibres circumferencial area has to start yielding. This requires the yield stress to be reached in every point along the length. The shear stress in the upper region will already be higher.

Thus, averaging the indenter load over the whole fibre surface area is not acceptable to determine yield stress. The values for yield stress obtained with formula (1.28.) from push-out measurements have to be rejected.

Young's modulus

The tensile tests suggested low values for the Young's modulus, estimated from the results of the composite tensile tests. With the microindentation method values more consistent with copper literature values (Fig. 3.31.) [120] were found in the coating of the single fibres (~110 GPa).

For the composite matrix which is under thermomechanical stress due to different CTE-values, the Young's modulus was determined too high by microindentation (~160 GPa). It seems that the stress state influences the measurement.

Finally the modulus of elasticity of the annealed copper matrix in the investigated composite cannot be given.

4.3. Influence of the microstructure on material properties

The carbon layer on the fibres surface is a protection of the fibre during processing and it maintains the tensile properties of the Textron fibres by reducing stress concentrations at the SiC-surface [137]. Originally this carbon layer was developed to optimise the properties of a titanium matrix composite.

For the copper matrix composite problems arise from the bad wetting properties of copper on carbon. The fact that no chemical reaction occurs between copper and carbon impedes a stronger bonding between the fibres' outer layer and the copper matrix. Rather the carbon layer itself acts as a lubricating film that aids the sliding of the fibre inside the matrix.

After thermal cycling of a simple Cu/SiC-composite sample without special interface treatment a fibre displacement occurred (Fig. 3.21.). The continuous strong expansion and contraction of the copper in fibre direction ”worked” the fibres out of the matrix. The direction of this process depends on microstructural roughness. The matrix material remains undamaged. This indicates a poor bonding between fibre and matrix.

These results were confirmed by push-out tests. As a consequence of the poor adhesion, a low interfacial shear strength of about 5 MPa was found (chapter 3.2.2.). As there is no chemical bonding between the SiC-fibres and the copper, only the thermal compressive stress due to the CTE mismatch between fibre and matrix has to be considered.
The post-experimental examinations of the push-out specimens by means of scanning electron microscopy confirmed the lack of chemical interaction between the fibre and the copper. No copper traces were found on the surface of the pushed-out fibre and no fragments of the carbon layer remained on the copper side (Fig. 3.38.). Vertical brush marks indicate the fibre sliding process.
The poor bonding was similarly confirmed by tensile tests, where broken fibres were pulled out of the matrix (Fig. 3.52.a)).
Transmission electron microscopy investigations in a cross section of the interface (chapter 3.1.2.) using EDX-analysis had also shown no reaction between the C-coating of the fibre and the Cu-matrix in non-annealed single Cu-coated fibres.
Microhardness measurements on the electrolytic copper layer of coated SiC-fibres, annealed at 550°C, did not show any hardening of the matrix close to the fibre (Fig. 3.26.). This verifies that not much carbon diffuses into copper and it does not lead to diffusion hardening.

For the improvement of the fibre matrix adhesion, a titanium interlayer was deposited (chapter 3.1.1.), which should lead to binding between the carbon-layer and the copper by forming a carbide that on the one hand is chemically bonded to the carbon and on the other hand disolves an amount of copper providing a bonding between carbide and copper.

Thermal cycling already showed first success on the improvement of the adhesion between matrix and titanium coated fibre surface, which affects the results in different ways. At first fibre displacement did not occur anymore, showing the stronger coupling. But this bonding also leads to strong longitudinal shear forces on the interface between SiC-core and carbon layer as a consequence of the high thermal expansion of the copper, resulting in a failure of this interface (Fig. 3.22.).
Another influence of continuous cycling of the strongly bonded constituents with great CTE mismatch is the formation of dislocations in the matrix around the fibre, where the copper is exposed to the highest stresses. The convergence of dislocations leads to grain boundary formation in the near fibre range, while in a distance larger grains are found.

Push-out results confirm the observation of a better bonding. The interfacial strength was raised by about one order of magnitude.
An influence of the titanium layer thickness on the push-out results could not be determined. SEM investigations showed that a failure of the boundary between titanium and copper did not occur, but between the two C-rich coatings of the original fibre or between the carbon-coating and the TiC-layer (Fig. 3.43. and 3.44.). Therefore a thin Ti-layer of about a few ten nanometers is sufficient to achieve both a chemical and a mechanical bonding between fibre and matrix. TEM-studies had shown the mechanical bonding by the interlocking between fibre surface and copper matrix and also the chemical formation of carbide was proven (chapter 3.1.6.2.).

From the tensile tests the strengthening of the interface became apparent. As analyses of the fracture surface had shown in SEM-investigations, the fibres were not pulled out of the matrix anymore, but the fracture of all fibres occurred in one plane (Fig. 3.52.b) and c)).

Tensile tests have not been carried out on thermally cycled composite samples, which will be the usual loading condition for the PFCs in a fusion reactor. The carbon coating that should avoid stress concentrations at the SiC-surface will no longer be bonded to the fibre due to the failure mechanisms described above. Its protective effect is lost and the failure will tend to initiate at lower loads. This shows the negative influence of the better coupling between the fibre and the copper matrix with a much greater coefficient of thermal expansion.

Although the thermal conductivity of the copper matrix composites was not yet determined, some statements can be given on its performance, which is very important for the PFC.

The influence of a thin titanium carbide layer around each fibre should be negligible on the heat conductivity of the composite. Hardness measurements did not show hardening of the Cu matrix in the proximity of the titanium layer. An alloy of copper with titanium was excluded by TEM/EDX investigations. The conductivity of the pure copper should be maintained in the matrix volume.

The copper matrix was found to be separated by boundaries with a hexagonal shape, visible in all images of the matrix structure, in metallographic specimens (Fig. 3.11.) as well as in SEM images of push-out (Fig. 3.42.a)) and tensile test samples (Fig. 3.53.). Their geometry results from the original coated fibres surface being pressed together in the HIP process. The origin could be a surface oxide layer on every copper coated fibre. This interface was found to be a weak point in the matrix. The interface failed in the tensile tests and in the push-out tests, where the matrix was plastically deformed.
This lack of a joining will have an influence on the thermal conductivity of the matrix. The matrix consolidation will need further optimisation.

A few hundred ppm of oxygen are also chemically bonded as Cu_2O (see chapter 2.1.3.) during electrolytic deposition. This leads to pores by combination with hydrogen to water vapour (chapter 4.1.) at high temperatures. The pores had no influence on the push-out behaviour, but will have on the thermal conductivity by disturbing the matrix homogeneity.
After carefully removing the hydrogen from the matrix by optimised heat treatment, the pores were reduced successfully (chapter 3.1.3.2.).

4.4. Conclusion and outlook

A way of producing a SiC/Cu-MMC has been shown. Electrolytic deposition on SiC-fibres with and without pre-sputtered coating is a gentle procedure for copper matrix processing. It avoids the high temperatures of infiltration with liquid copper.
Carefully annealing of the electrolytic copper is a successful method to avoid pores in the matrix.
Pre-sputtering a titanium interlayer is an effective technique to increase the adhesion between fibre and copper matrix by a reactive chemical bonding.

The composite system needs further improvement. A homogeneous matrix must not show non bonded boundaries around the original constituents. At the very least after annealing they should be dissolved. These oxide boundaries may decrease the macroscopic thermal conductivity. The mechanical behaviour is also influenced due to missing coupling.
The influence of hydrogen on oxygen-containing copper is known as the ”hydrogen disease”. In the case of application to a fusion device the recurrence of hydrogen by diffusion and neutron-electron recombination is inescapable. Water vapour destroying the matrix will again be formed from the remaining traces of oxygen.

Problems arise from the large CTE mismatch between copper and silicon carbide. The long term behaviour during thermal cycling at high temperature is insufficient, as the fibre/matrix bonding is destroyed. A usage at moderate temperature might be possible.

For the application as heat conductor in a fusion device the prevention of matrix destruction is required. In the presence of hydrogen no oxygen can be tolerated at temperatures above 400°C. A possibility for reducing the oxygen content without melting the copper is annealing in a carbon monoxide atmosphere. The oxygen atoms diffusing to the material surface need not recombine into an oxygen molecule but can directly react with the carbon monoxide to form carbon dioxide. Copper is non-soluable for both gases and the process is described as relatively fast [115]. This would also remove the surface oxide layer from the coated fibres if it is possible to avoid further contact with air.

To avoid damage to the interfacial layer before full carbidisation, heat treatment could be applied in advance of the electrolytical deposition. Thermally expanding the thin titanium and copper layers will not be as strong as the thick electrolytic coating, thus the layers will stay bonded to the fibre and carbidisation can be completed.

For the composite integrity it is also required to avoid damage resulting from the CTE mismatch between matrix and fibre. A solution might be a graded interface between fibre surface and copper to smooth the transition. A stress reducing mantle around every fibre can protect the carbon surface and thus help to maintain the fibre’s strength.

5. Summary

The task of this work was the development of a new SiC-long fibre reinforced copper matrix composite. It shall be used in fusion reactors as a constituent of the plasma facing components. Its task is to absorb high stresses in critical interfaces between the plasma facing material and the heat sink. Due to this it must also have maximum thermal conductivity. It shall allow a higher operational temperature than the current components and thereby increase the efficiency of the fusion power plant.

The processing procedure was developed and then optimised. Commercially available SiC-fibres (Textron SCS-6) consist of a SiC core, coated with a carbon rich layer to avoid stress concentrations at the SiC surface. These fibres were electrolytically coated with copper as a matrix material. Suitable parameters for the electrolytic deposition were determined.
For a better fibre/matrix adhesion the fibre surface was pre-coated with titanium to reactively form titanium carbide at the interface. Magnetron sputtering was used for this process with the fibres standing upright on a rotating table in the sputtering chamber. The titanium layer was protected against oxidation with a subsequently sputtered copper layer. Titanium carbide was formed from the reaction of titanium with the subjacent carbon layer during later annealing procedures.
After electrolytic deposition of the copper matrix a heat treatment was applied to avoid the porosity caused by the “hydrogen disease” of copper. The desorption of hydrogen from electrolytic copper was investigated with a mass-spectrometer in ultra high vacuum to optimise the heat treatment.
The fibres were bundled in a copper capsule. The capsule was welded under vacuum and hot isostatically pressed for composite consolidation.

For the purpose of characterisation and optimisation the processing was accompanied by microstructure investigations and mechanical tests.
The microstructure of single coated fibres and composites was studied using both optical and scanning electron microscopy. The titanium interface was characterised by transmission electron microscopy. EDX measurements were performed as well for elemental characterisation and impurity detection. Composite samples were thermally cycled to observe the long term behaviour.
The mechanical properties were determined by means of microhardness measurements, tensile tests and fibre push-out tests. Microhardness measurements were performed on as-deposited electrolytic copper, annealed copper coated fibres and the copper matrix of a consolidated composite. Composites and correspondingly treated coated single fibres were tensile tested for comparison. Push-out tests were used to acquire interfacial parameters.

The following conclusions can be drawn. The behaviour of the composite depends on the interface characteristics, as was shown by the results of push-out tests, tensile tests and thermal cycling.
The creation of a titanium carbide interlayer results in a strong chemical bonding between fibre and matrix, while the strength of the SCS-6 fibre is not directly affected by the additional layer. As no diffusion was found in the composites without interfacial coating, neither of carbon into the copper nor of copper into the fibres outermost carbon layer, the function of the titanium layer as a diffusion barrier is not relevant.
The microstructural investigations of the matrix material have shown a strong grain growth of the copper crystallites, which was expected after treating the material at temperatures higher

than the recrystallisation temperature. After long term thermal cycling the grains were found to be even larger. Only around the fibres with a titanium carbide interface smaller grains were detected due to the cyclic stress.

Electrolytically deposited copper is a material of high purity. Only a small amount of sulphur was found. Oxygen, chemically bonded as Cu_2O, and hydrogen are also known impurities in this material.

Around every originally coated fibre in the consolidated composite a non-bonded border can be observed. This border is due to surface oxidation of the coated single fibres. It does not vanish even after long term annealing.

In the first processed composites pores were found in the matrix material. These pores are due to the formation of water vapour from hydrogen and oxygen at about 400°C. To prevent the pore formation during heat treatment the material has to be carefully degased. Hydrogen desorption was found to start at 250°C. In the composites pre-heated in this way the pores were absent.

The microstructure of the fibre/matrix interface investigated by TEM showed no diffusion between copper matrix and the outermost carbon layer. With an additional titanium coating, titanium carbide was formed. The carbide layer was strongly interlocked with the copper matrix. The interface was in some places found to be broken before complete carbidisation. This is attributed to the high coefficient of thermal expansion of copper.

The thermal cycling experiments revealed the long term behaviour of the interfacial microstructure. Composites without strengthened interface show fibre displacement, indicating poor bonding. With titanium carbide interface the fibres did not move but the interface between carbon layer and SiC fibre-core failed.

The mechanical properties of the composite material were evaluated. The hardness of the matrix material was determined and no local hardening was found. This correlates with TEM-investigations where no element diffusion from the fibres into the matrix was found.

From the measurement curves of the microindentation tests the elastic modulus was derived. It was in agreement with the values in the literature. A higher modulus was observed in the consolidated composite. The thermal stress after cooling from fabrication temperature is thought to influence the results.

From push-out experiments interfacial shear strength and interfacial friction stress were determined. For composites without carbidic interface these values were relatively low. This corresponds to a lack of chemical bonding between fibre and matrix. For composites with titanium carbide interface the values were higher by one order of magnitude.

Tensile tests showed the stress-strain behaviour of the composites. From these tests the Young’s modulus, the ultimate tensile strength and the matrix yield strength were derived. The tensile tests revealed that the matrix does not contribute to the strength of the composite. It acts more like a filler material to adjust the fibre volume fraction. The titanium carbide interface while it has no influence on the strength does affect the fracture behaviour. Without bonding the failure behaviour is comparable to a loose fibre bundle, while the strongly coupled interface enforces a crack in one plane.

For the first time it could be demonstrated, that a reinforcement of copper by SiC long fibres is possible. Some points are to be improved in future works.

6. References

[1] G. Nebbia: *Twenty twenty-five*. Futures 33 1 (2001), pp. 43-54.

[2] D. J. Wuebbles, A. K. Jain: *Concerns about climate change and the role of fossil fuel use*. Fuel Processing Technology, 71 (2001), pp. 99–119.

[3] J. A. Schmidt and J. M. Ogden: *Fusion power deployment*. Fusion Engineering and Design 63-64 (2002), pp. 19-23.

[4] A.Ciampichetti et al.: *Accidental and long-term safety assessment of fission and fusion power reactors*. Fusion Engineering and Design 63-64 (2002), pp. 229-234.

[5] PCAST Panel on the U.S. Program of Fusion Energy Research and Development, 1995.

[6] X. Sillen et al.: *Analysis of human intrusion scenarios for the deep disposal of fusion wastes*. Fusion Engineering and Design 54 (2001), pp. 575–581.

[7] P. Rocco, M. Zucchetti: *Long-term safety of fission and fusion waste disposal*. Fusion Engineering and Design 51–52 (2000), pp. 593–597.

[8] K. Brode´n: *Waste from fusion reactor: A comparison with other energy producing systems*. Fusion Engineering and Design 42 (1998), pp. 1–6.

[9] T. Hamacher et al.: *A comprehensive evaluation of the environmental external costs of a fusion power plant*. Fusion Engineering and Design 56-57 (2001), pp. 95-103.

[10] R. Toschi: N*uclear fusion, an energy source*. Fusion Engineering and Design 36 (1997), pp. 1-8.

[11] J. Ongena and G. Van Oost: *Energy for future centuries*. Transactions of fusion science and technology 41 (2002), pp. 3-14.

[12] E. Rebhan: *Thermonuclear burn criteria*. Transactions of fusion science and technology 41 (2002), pp. 15-23.

[13] Internal Report, Max-Planck Institut für Plasmaphysik (IPP): *Einführung in die Fusionsforschung "Kernfusion - Berichte aus der Forschung",* Garching 1995.

[14] N. R. Marshal: *Opportunities in the Fusion Energy Sciences Program*. Fusion Energy Sciences Advisory Committee (FESAC) Report, June 1999.

[15] M. Lindinger: *Die Kernfusion in der Wasserstoffkapsel*. Frankfurter Allgemeine Zeitung 94, 23.04.2003, pp. N1.

[16] G. Federici et al.: *Plasma-material interactions in current tokamaks and their implications for next step fusion reactors*. Nuclear Fusion 41 (2001), pp. 1967-2137.

[17] K. Lackner et al.: *Long-term fusion strategy in Europe*. Journal of Nuclear Materials 307-311 (2002), pp. 10-20.

[18] A. Cardella et al.: *Design of the ITER EDA plasma facing components.* Fusion Engineering and Design 39-40 (1998), pp. 377-384.

[19] D. Reiter et al.: *Time dependent neutral gas transport in tokamak edge plasmas,* Journal of Nuclear Materials 220-222 (1995), pp. 987-992.

[20] ITER Physics Basis Editors, ITER Physics Expert Group Chairs and Co-Chairs and ITER Joint Central Team and Physics Integration Unit: *Chapter 1: Overview and summary*. Nuclear Fusion 39 (1999), pp. 2137-2174.

[21] K. J. Dietz et al.: *Engineering and design aspects related to the development of the ITER divertor*. Fusion Engineering and Design 27 (1995), pp. 96-108.

[22] G. Janeschitz et al.: *The ITER divertor concept*. Journal of Nuclear Materials 220-222 (1995), pp. 73-88.

[23] U. Schumacher: *Status and problems of fusion reactor development*. Naturwissenschaften 88 (2001), pp. 102-112.

[24] J. N. Brooks et al.: *Erosion/redeposition analysis: status of modeling and code validation for semi-detached tokamak edge plasmas*. Journal of Nuclear Materials 266-269 (1999), pp. 58-66.

[25] G. Federici et al.: *Critical plasma-wall interactions issue for plasma-facing materials and components in near-term fusion devices*. Journal of Nuclear Materials 283-287 (2000), pp. 110-119.

[26] G. Federici et al.: *In-vessel tritium retention and removal in ITER*. Journal of Nuclear Materials 266-269 (1999), pp. 14-29.

[27] V. Barabash et al.: *Carbon fiber composites application in ITER plasma facing components*. Journal of Nuclear Materials 258-263 (1998), pp. 149-159.

[28] K. Ioki, V. Barabash et al.: *Design and material selection for ITER first wall/blanket, divertor and vacuum vessel*. Journal of Nuclear Materials 258-263 (1998), pp. 74-84.

[29] G. Janeschitz et al.: *The requirements of a next step large steady state tokamak*. Nuclear Fusion 40 6 (2000), pp. 1197-1221.

[30] R. Parker et al.: *Plasma-wall interactions in ITER*. Journal of Nuclear Materials 241-243 (1997), pp. 1-26.

[31] G. Janeschitz: *Plasma-wall interactions issues in ITER*. Journal of Nuclear Materials 290-293 (2001), pp. 1-11.

[32] V. Barabash et al.: *Selection, development and characterisation of plasma facing materials for ITER*. Journal of Nuclear Materials 233-237 (1996), pp. 718-723.

[33] H. Bolt et al.: *Plasma facing and high heat flux materials – needs for ITER and beyond*. Journal of Nuclear Materials 307-311 (2002), pp. 43-52.

[34] B. N. Singh et al.: *Temperature and dose dependencies of microstructure and hardness of neutron irradiated OHFC copper*. Journal of Nuclear Materials 224 (1995), pp. 131-140.

[35] G. Kalinin et al.: *Structural materials for ITER in-vessel component design*. Journal of Nuclear Materials 233-237 (1996), pp. 9-16.

[36] S. A. Fabritsiev et al.: *Evaluation of copper alloys for fusion reactor divertor and first wall components*. Journal of Nuclear Materials 233-237 (1996), pp. 127-137.

[37] G. Kalinin and R. Matera: *Comparative analysis of copper alloys for the heat sink of plasma facing components in ITER*. Journal of Nuclear Materials 258-263 (1998), pp. 345-350.

[38] J. W. Davis and G. M. Kalinin: *Material properties and design requirements for copper alloys used in ITER*. Journal of Nuclear Materials 258-263 (1998), pp. 323-328.

[39] G.M. Kalinin et al.: *Specification of properties and design allowables for copper alloys used in HHF components of ITER*. Journal of Nuclear Materials 307-311 (2002), pp. 668-672.

[40] A. A. F. Tavassoli: *Materials design data for fusion reactor*. Journal of Nuclear Materials 258-263 (1998), pp. 85-96.

[41] J. H. You: *Loading characteristics of material interfaces in divertor joint components for thermonuclear reactors under fusion relevant conditions*. Master of Science thesis, Seoul, Korea, (1996).

[42] S. Suzuki et al.: *Thermal fatigue damage of the divertor plate*. Fusion Engineering and Design 49–50 (2000), pp. 343–348.

[43] E. Visca et al.: *Thermal fatigue equipment to test joints of materials for high heat flux components*. Fusion Engineering and Design 49–50 (2000), pp. 377–382.

[44] J. H. You and H. Bolt: *Overall mechanical properties of fiber-reinforced metal matrix composites for fusion applications*. Journal of Nuclear Materials 305 (2002), pp. 14–20.

[45] R.H. Jones et al.: *Promise and challenges of SiC/SiC composites for fusion energy applications*. Journal of Nuclear Materials 307-311 (2002), pp. 1057-1072

[46] G. J. Butterworth and C. B. A. Forty: *A survey of copper alloys for use as fusion reactor materials*. Journal of Nuclear Materials 189 (1992), pp. 237-276.

[47] V. Barabash et al.: *Armor and heat sink materials joining technologies development for ITER plasma facing components*. Journal of Nuclear Materials 283-287 (2000), pp. 1248-1252.

[48] A. Kurumada et al.: *Evaluation of the integrity of divertor models of tungsten or SiC/SiC composites joined with copper*. Journal of Nuclear Materials 313-316 (2003) pp. 247-251.

[49] U. Holzwarth et al.: *On the recovery of the physical and mechanical properties of a CuCrZr alloy subjected to heat treatments simulating the thermal cycle of hot isostatic pressing*. Journal of Nuclear Materials 279 (2000), pp. 19-30.

[50] D. B. Miracle and S. L. Donaldson: *Composites*. Section 1, Introduction to Composites, ASM Handbook, Volume 21, 2001.

[51] K. Kaw: *Mechanics of Composite Materials*. CRC Press, New York, 1997, Chapter 3.3.

[52] B. Terry and G. Jones: *Metal matrix composites*. Elsevier Advanced Technology, Mayfield House, Oxford UK, 1990, pp. 3-11.

[53] R. M. Jones: *Mechanics of composite materials*. Scripta book company, Washington, D. C., 1975, pp. 10-13.

[54] T. W. Clyne and P. J. Withers: *An introduction to metal matrix composites*. Cambridge University Press, (1993), pp. 7-10.

[55] K. K. Chawla: *Composite materials Science and Engineering*. 2nd ed. Springer, 1998, Chapter 10, pp. 109-114, 170-206.

[56] W. D. Jr. Callister: *Fundamentals of Materials Science and Engineering Am interactive e-text*. 5th ed. John Wiley & Sons, Inc., 2001, pp. 172-177.

[57] F. L. Mattheus and R. D. Rawlings: *Composite materials: Engineering and Science*. Chapman & Hall, London, 1994, pp. 91-94.

[58] K. W. Weber et al.: *Titanmatrix Faserverbund-werkstoffe für Verdichterkomponenten* in Cluster Werkstoffe und Strukturen. Annual report DLR, Cologne, 1998, pp. 99-107.

[59] W. Buchgraber et al.: *Carbon fibre reinforced copper matrix composites: Production routes and functional properties*. Submitted to the EUROMAT, 1999, München.

[60] J. Hemptenmacher et al.: *Microstructural Characterization of the Titanium alloy Ti-6Al-4V Used as a Metal Matrix in SiC-Fibre Composites*. Practical Metallography 30 [12] (1993), pp. 609-621.

[61] H. J. Dudek et al.: *Entwicklung von warmfesten faserverstärkten Titanlegierungen,* in: *Titan und Titanlegierungen*. Hrg.: M. Peters, C. Leyens, J. Kumpfert, DGM Verlag, Oberursel, 1996, pp. 107-122.

[62] J. Korab et al.: *Thermal expansion of cross-ply and woven carbon fibre-copper matrix composites*. Composites, Part A 33 (2002), pp. 133-136.

[63] A. F. Whitehouse et al.: *Electrical resistivity of copper reinforced with short carbon fibers*. Journal of Materials Science 26 (1991), pp. 6176-6182.

[64] G. Lefranc et al.: *Al-SiC improves reliability of IGBT power modules*. Proceedings of ICCM-12, Paris, 1999, pp. 1335-1344.

[65] G. Korb et al.: *Thermophysical properties and microstructure of short carbon fibre reinforced Cu-matrix composites made by electroless copper coating or powder metallurgical route*. Proceedings of the Electronic Manufacturing Technology Symposium IEMT Europe, Potsdam, 1998, pp. 98-103.

[66] P. Stefanik and P. Sebo: *Thermal expansion of copper-carbon fiber composites*. Theoretical and Applied Fracture Mechanism 20 (1994), pp. 41-45.

[67] P. Stefanik et al.: *Thermal expansion of copper matrix composite with spiral arrangement of carbon fibres*. Journal of Materials Science Letters 16 (1997), pp. 392-394.

[68] J. Korab et al.: *Thermal conductivity of unidirectional copper matrix carbon fiber composites*. Composites: Part A 33 (2002), pp. 577-581.

[69] G. Korb et al.: *Properties and microstructure of short carbon fibre reinforced copper matrix composite*. Proceedings of the 21st Int. Spring Seminar on Electronics Technology, 1998, Neusiedl, pp.116-120.

[70] P. Stefanik and P. Sebo: *Thermal stability of copper coating on carbon fibres*. Journal of Materials Science Letters 12 (1993), pp. 1083-1085.

[71] T. Weissgaerber et al.: *Cu-SiC Composites for Thermal Management Application prepared by Powder Metallurgy*. Proceedings of Materials week 2000, Frankfurt, 2000.

[72] D. A. Mortimer and M. Nicholas: *The wetting of Carbon by Copper and Copper Alloys*. Journal of Materials Science 5 (1970), pp. 149-155.

[73] O. Dezellus and N. Eustathopoulos: *The role of van der Waals interactions on wetting and adhesion in metal/carbon systems*. Scripta Materialia, 40 [11] (1999), pp. 1283-1288.

[74] D. A. Mortimer and M. Nicholas: *The wetting of carbon and carbides by copper alloys*. Journal of Materials Science 8 (1973), pp. 640-648.

[75] A. Preidel et al.: *Verbesserung des Benetzungsverhaltens von Kohlefaserfilzen für die Herstellung von MMCs*. Verbundwerkstoffe und Werkstoffverbunde, Wiley-VCH Verlag GmbH, Weinheim, 2001, pp. 235-240.

[76] E. Neubauer et al.: *Einsatz von PVD Beschichtungsverfahren zur Steigerung der Haftung von Cu Schichten auf Kohlenstoff für die Herstellung von Cu-C-MMC*s. Verbundwerkstoffe. 14. Symposium Verbundwerkstoffe und Werkstoffverbunde, Wiley-VCH Verlag GmbH, Weinheim, 2003, pp. 79-84.

[77] P. B. Abel et al.: *Study of copper on graphite with titanium or chromium bond layer*. Journal of Materials Research, 9 [3] (1994), pp. 617-624.

[78] T. Massalski: *Binary Alloy Phase Diagams*. American Society for Metals, Vol. 1, 1986, pp. 593-596.

[79] A. E. W. Jarfors: *The influence of carbon on the phases in the copper-titanium system and their precipitation*. Journal of Materials Science 34 (1999), pp. 4533-4544.

[80] S. Miller: *Untersuchung der chemischen Wechselwirkung von Titan und Kohlenstoff mittels Röntgen-Photoelektronen-Spektroskopie*. PhD thesis submitted at Bayreuth University, 1997.

[81] D. H. Grande et al.: *Fibre-matrix bond strength studies of glass, ceramic, and metal matrix composites*. Journal of Materials Science 23 (1988), pp. 311-328.

[82] J. D. Bright and D. K. Shetty: *Interfacial Bonding and Friction in Silicon Carbide (Filament)-Reinforced Ceramic- and Glass-Matrix Composites*. Journal of American Ceramic Society 72 [10] (1989), pp. 1891-1898.

[83] R. J. Kerans: *Theoretical analysis of the Fiber Pullout and Pushout Tests*. Journal of American Ceramic Society 74 [7] (1991), pp. 1585-1596.

[84] G. P. Tandon and N. J. Pagano: *Micromechanical analysis of the fiber push-out and re-push test*. Composite Science and Technology 56 (1998), pp. 1709-1725.

[85] Yongjian Sun and R. N. Singh: *A technique for the determination of interfacial properties from debond length measurement*. Journal of Materials Science 35 (2000), pp. 5681-5690.

[86] S. W. Wang et al.: *A novel nanoindentor technique for measuring fiber-matrix interfacial strengths in composites*. Journal of Materials Science Letters 11 (1992), pp. 739-741.

[87] D. A. Koss et al.: *Mechanics of interfacial failure during thin-slice fiber push-out tests*. Materials Research Society Symposium Proceedings, 273 (1992), pp. 303.

[88] I. Roman and P. D. Jero: *Interfacial shear behavior of two titanium-based SCS-6 model composites*. Materials Research Society Symposium Proceedings Vol. 273 (1992), pp. 337.

[89] G. Rausch et al.: *A push-out technique for the evaluation of interfacial properties of fiber-reinforced materials*. Journal of the European Ceramic Society 10 (1992), pp. 229-235.

[90] K. Honda and Y. Kagawa: *Debonding criterion in the push-out process of fiber-reinforced ceramics*. Acta Materialia, 44 [8] (1996), pp. 3267-3277.

[91] B. Guichet et al.: *A study of the micromechanical push-out test: response of an SCS-6/Ti-6242 composite*. Composites Science and Technology 58 (1998), pp. 665-670.

[92] D. Osborne et al.: *Interphase behavior of titanium matrix composites at elevated temperature*. Composites, Part A 32 (2001), pp. 545-553.

[93] N. Chandra and H. Ghonem: *Interfacial mechanics of push-out tests: theory and experiments*. Composites, Part A 32 (2001), pp. 575-584.

[94] X.. F. Zhou, H. D. Wagner and S. R. Nutt: *Interfacial properties of polymer composites measured by push-out and fragmentation tests*. Composites, Part A 32 (2001), pp. 1543-1551.

[95] W. D. Zeng et al.: *Interfacial bond strength and fracture energy at room and elevated temperature in titanium matrix composites (SCS-6/Timetal 834)*. Composites, Part A 33 (2002), pp. 1159-1170.

[96] N. Chandra and C. R. Ananth: *Analysis of interfacial behavior in MMCs and IMC by the use of thin-slice push-out tests*. Composites Science and Technology 54 (1995), pp. 87-100.

[97] L. B. Greszczuk: *Theoretical studies of the mechanics of the fibre-matrix interface in composites*. Interfaces in Composites, ASTM STP 452. American Society for Testing and Materials, 1969, Section 11-C.

[98] P. Lawrence: *Some theoretical considerations of fiber pull-out from an elastic matrix*. Journal of Materials Science 7 (1970), pp. 1-6.

[99] R. J. Gray: *Analysis of the effect of embedded fibre length on fibre debonding and pull-out from an elastic matrix*. Journal of Materials Science 19 (1984), pp. 861-870.

[100] R. J. Kerans et al.: *The Role of the Fiber-Matrix Interface in Ceramic Composites*. Ceramic Bulletin 68 [2] (1989), pp.429-441.

[101] M. R. Piggott: *Interfaces in Composites*. Reprinted from the Journal of Composites Science and Technology Vol. 42 Nos 1-3., Elsevier Applied Science, 1991.

[102] D. K. Shetty: *Shear-Lag Analysis of Fiber Push-Out (Indentation) Tests for Estimating Interfacial Friction Stress in Ceramic-Matrix Composites*. Communications of the American Ceramic Society 71 [2] (1989), pp. C-107-C-109.

[103] S. R. Nutt and F. E. Wawner: *Silicon carbide filaments: microstructure*. Journal of Materials Science 20 (1985), pp. 1953-1960.

[104] F. E. Wawner, JR.: *Boron and Silicon Carbide/Carbon Fibers* in *Fibre reinforcements for composite materials*. edited by A. R. Bunsell, Elsevier Science Publishers, 1998, pp. 397-425.

[105] X. J. Ning and P. Pirouz: *The microstructure of SCS-6 SiC fiber*. Journal of Materials Research Vol. 6, No 10 (1991), pp. 2232-2248.

[106] X. J. Ning et al.: *The structure of carbon in chemically vapor deposited SiC monofilaments*. Journal of Materials Research Vol. 5, No 12, (1990), pp. 2865-2876.

[107] P. R. Smith et al.: *Heat treatment effects on SiC fiber*. Journal of Materials Science 33 (1998), pp. 5855-5872.

[108] Silicon Carbide (SCS) Filament Data, Textron Specialty Materials, Lowell, MA (1994).

[109] D. D. Edie: *The effect of processing on the structure and properties of carbon fibers*. Carbon Vol.36, No. 4, 1998, pp. 345-362.

[110] R. H. Jones et al.: *Promise and challenges of SiC/SiC composites for fusion energy applications*. Journal of Nuclear Materials 307–311 (2002), pp. 1057–1072.

[111] J. E. Mahan: *Physical Vapor Deposition of Thin Films*. John Wiley an Sons, INC., A Wiley-Interscience Publication, New York, 2000, p. 153.

[112] Y. Z. Wan et al.: *Effect of metal diffusion barrier on thermal stability of metal-coated carbon fibers*. Journal of Materials Science 36 (2001), pp. 2809-2814.

[113] S. J. Sun and M. D. Zhang: *Interface characteristics and mechanical properties of carbon fibre reinforced copper composites*. Journal of Materials Science 26 (1991), pp. 5762-5766.

[114] Pay Yih and D. D. L. Chung: *Silicon carbide whisker copper-matrix composites fabricated by hot pressing copper coated whiskers*. Journal of Materials Science 31 (1996), pp. 399-406.

[115] W. Espe: *Werkstoffkunde der Hochvakuumtechnik*. Veb Deutscher Verlag der Wissenschaften, 1959, pp. 267-305.

[116] S. C. Dexter: *Corrosion of Copper and Copper Alloys*. Metals Handbook, 9th ed., 13, Corrosion, ASM International, 1987, pp.610

[117] K. Dies: *Kupfer und Kupferlegierungen in der Technik*. Springer Verlag, 1967, p. 679-687.

[118] J. Dinter et al.: *Finite element modeling of the push-out test for SiC fibre-reinforced titanium alloys*. Composites, Part A 27A (1996), pp. 749-753.

[119] Goodfellow corporation catalog, 800 Lancaster Avenue, Berwyn, PA 19312-1780, USA, (2001).

[120] W. D. Jr. Callister: *Materials science and engineering an introduction*. 6th ed. John Wiley & Sons, Inc., 2003, p. 755.

[121] Micro Materials NanoTest User Manual, Micro Materials Ltd. Wrexham, United Kingdom, last update June 2002.

[122] W. C. Oliver and G. M. Pharr. *An improved technique for determining hardness and elastic modulus using load and displacement sensing indentation experiments*. Journal of Materials Research 7 [6] (1992), pp. 1564-1583.

[123] M. F. Doerner and W. D. Nix: *A method for interpreting the data from depth-sensing indentation instruments*. Journal of Materials Research 1 [4] (1986), pp. 601-609.

[124] W. D. Nix: *Mechanical properties of thin films*. Metallurgical Transactions 20A (1989), pp. 2217-2245.

[125] H. Fischer: *Elektrolytische Abscheidung und Elektrokristallisation von Metallen*. Springer Verlag, 1954.

[126] M. Shah et al.: *Mechanical Characterization of the Heat Affected Zone of Gold Wirebonds Using Nanoindentation*. Proceedings of Advanced Materials for Micro- and Nano-Systems, Symposium, Singapore 2002.

[127] K. W. McElhaney et al.: *Determination of indenter tip geometry and indentation contact area for depth-sensing indentation experiments*. Journal of Materials Research 13, 5, (1998), pp. 1300-1306.

[128] S. M. Pickard and D. B. Miracle: *An experimental study of residual stresses in SiC-fiber-reinforced Ti-based composites*. Materials Science and Engineering. A203 (1995), pp. 59-68.

[129] C. Gonzales and J. Llorca: *Micromechanical modelling of deformation and failure in Ti-6Al-4V/SiC composites*. Acta mater. 49 (2001), pp. 3505-3519.

[130] H. Jiang et al.: *Microstructural evolution, microhardness and thermal stability of HPT-processed Cu*. Materials Science and Engineering A290 (2000), pp. 128-138.

[131] D. V. Read: *Young's modulus of thin films by speckle interferometr*. Meas. Sci. Technol. 9 (1998), pp. 676-685.

[132] B. Guichet et al.: *Study of Push-Out Micromechanical Test: Response of SCS-Ti-6242 Composite*. Key Engineering Materials Vols. 127-131 (1997) pp. 651-658.

[133] D. B. Gundel and F. E. Wawner: *Experimental and theoretical assessment of the longitudinal SiC-fiber/titanium-matrix composites*. Composites Science and Technology 57 (1997), pp. 471-481.

[134] Composite Materials Handbook: *Metal Matrix Composites*. Vol. 4. MIL-HDBK-17-4, 1999.

[135] J. Hemptenmacher et al.: *Scherfestigkeituntersuchungen on Faserverbundwerkstoffen mit der warmfesten Titanlegierung IMI834 als Matrix*. Progresss in Metallography, M. Kurz, M. Pohl, DGM Informationgesellschaft mbH, 1995.

[136] J. Hemptenmacher et al.: *Characterization of SiC-Fibre/Ti 6Al 4V-Matrix Composites by Macro-Indentation Tests*. Practical Metallography 31 [3] (1994), pp. 110-119.

[137] S. Q. Guo et al.: *Microstructure and role of outermost coating for tensile strength of SiC fiber*. Acta mater. Vol 46, No. 14 (1998), pp. 4941-4954.

[138] T. Matthams et al.: *Introduction to mechanical testing*. Library of Teaching and Learning Packages for Materials Science, Department of Materials Science and Metallurgy, University of Cambridge, 2003.
(http://www.msm.cam.ac.uk/doitpoms/tlplib/BD3/credits.php)